Department of Physics and Astronomy

University of Heidelberg

Master's thesis in Physics

submitted by

Christian Warnecke

born in Rendsburg

2019

Imaging of Coulomb crystals in a cryogenic Paul trap experiment

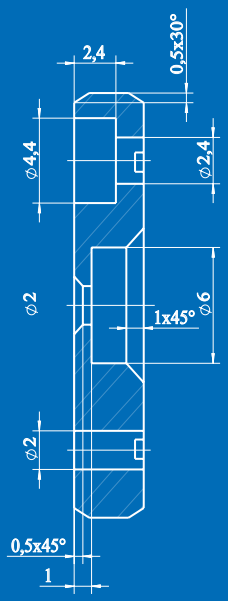

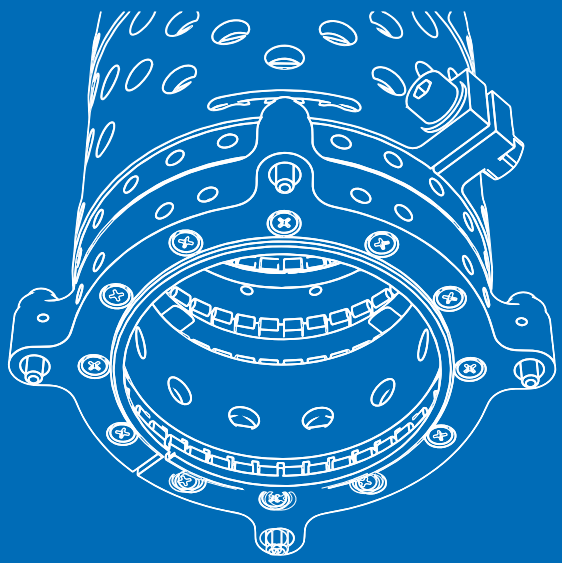

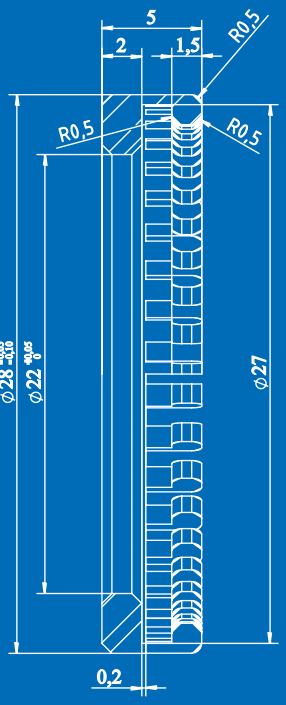

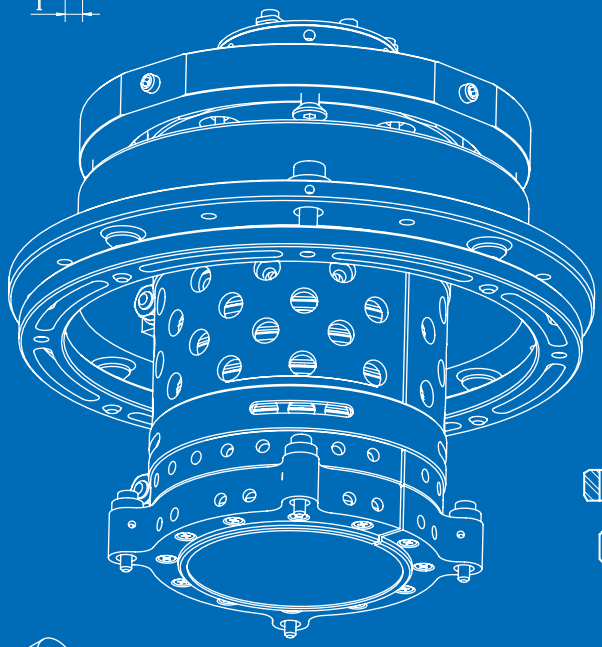

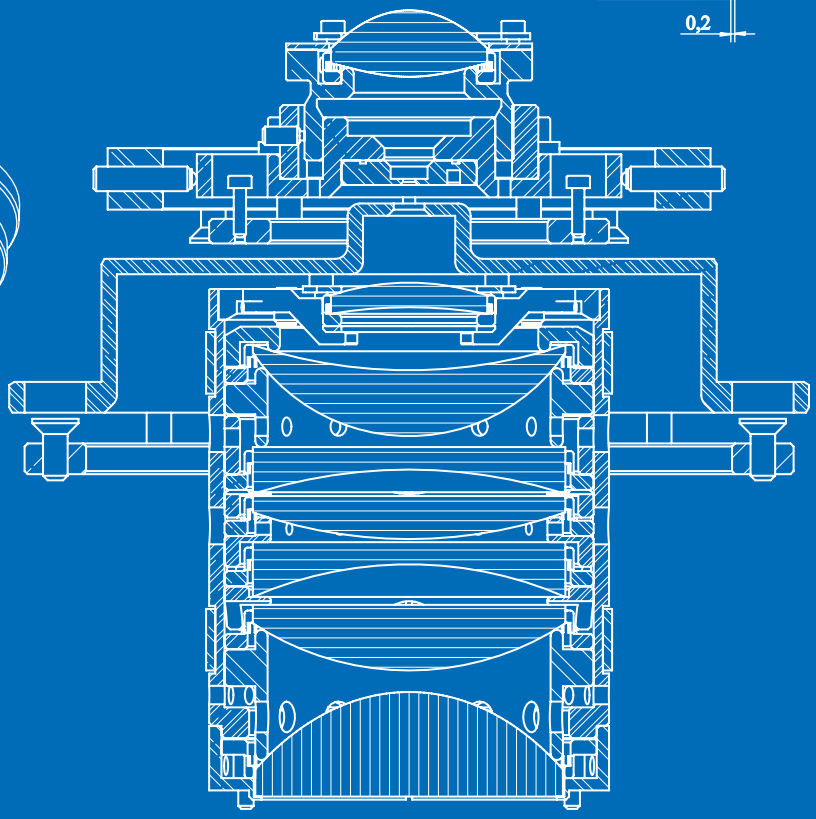

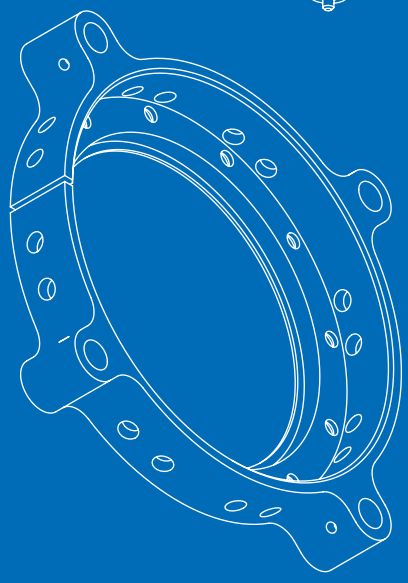

This thesis has been carried out by
Christian Warnecke
at the
Max-Planck-Institut für Kernphysik
under the supervision of
Priv.-Doz. Dr. José Ramón Crespo López-Urrutia

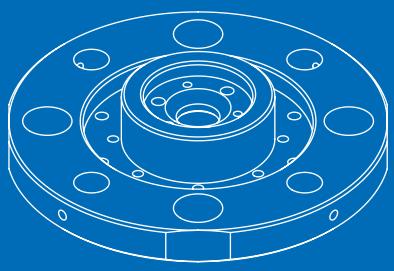

ABSTRACT

Visual observation always has been an important tool for scientific experiments. While in the early 16*th* century structures of cells already have been resolved with simple optical systems, the subject of this work is the observation of atoms and ions controlled and manipulated by coherent light. To detect and localize laser-cooled beryllium ions confined in a cryogenic Paul trap with superconducting radio-frequency quadrupole resonator a microscope objective with 57 mm working distance, numerical aperture $NA = 0.365$ and variable magnification from 7.8× to 20× has been designed and tested. As design wavelength, the $^2S_{1/2} \leftrightarrow {}^2P_{3/2}$ cooling transition of Be^+ at 313 nm was chosen. Also, the eight-lens system has the capability to efficiently collect fluorescence of the resonance-enhanced two-photon ionization transition of atomic beryllium at 235 nm. Beryllium ions are of importance for sympathetic cooling of highly charged ions, which are excellent candidates for extreme ultraviolet frequency standards since some of them possess highly forbidden transitions in that spectral range. In the commissioning phase of the cryogenic paul trap experiment (CryPTEx) II which was designed and built at the Max-Planck Institut für Kernphysik, the M1 hyperfine-transition from a single Ar^{13+} retrapped from an electron beam ion trap (EBIT) and cooled by one Be^+ ion, shall be resolved. This transition has a wavelength of 441 nm and can be also detected through the microscope objective.

ZUSAMMENFASSUNG

Die visuelle Observation ist schon seit jeher von Bedeutung in wissenschaftlichen Experimenten. Während im frühen sechzehnten Jahrhundert bereits Strukturen von Zellen mit einfachen optischen Systemen beobachtet werden konnten, ist das Thema in dieser Arbeit die Observation von Atomen und Ionen, welche mit kohärenten Licht kontrolliert und manipuliert werden. Um lasergekühlte Beryllium Ionen, welche in einer kryogenen Paul Falle ausgestattet mit einem supraleitenden Radiofrequenz Resonator eingeschlossen wurden, zu detektieren und lokalisieren, wurde ein Mikroskop Objektiv mit einer Arbeitsdistanz von 57 mm, einer numerischen Apertur von $NA = 0.365$ sowie einer variablen Vergrößerung von 7.8× bis 20× entwickelt und getestet. Als Design Wellenlänge wurde der $^2S_{1/2} \leftrightarrow {}^2P_{3/2}$ Kühlübergang der Beryllium Ionen ausgewählt. Zusätzlich ist mit dem acht-Linsen-System eine effiziente Fluoressenzsammlung der resonanzverstärkten Zweiphotonionisation des atomaren Beryllium bei 235 nm möglich. Die Beryllium Ionen sind von Wichtigkeit für das sympathetische Kühlen von hochgeladenen Ionen, welche exzellente Kandidaten für extrem Ultraviolett Frequenzstandards sind, weil manche stark verbotenen Übergänge in diesem Spektralbereich besitzen. In der Inbetriebnahme Phase von CryPTEx II, welches am Max-Planck-Institut für Kernphysik entwickelt und gefertigt wurde, soll der M1 Hyperfeinstruktur Übergang von Ar^{13+}, welches aus einer EBIT wieder eingefangen und mit einem Be^+ Ion gekühlt wird, aufgelöst werden. Dieser Übergang besitzt eine Wellenlänge von 441 nm und kann ebenfalls durch das Mikroskop Objektiv detektiert werden.

CONTENTS

1 INTRODUCTION 11

2 THE CRYOGENIC PAUL TRAP EXPERIMENT 17
- 2.1 The linear Paul trap 17
  - 2.1.1 Equations of motion in an ideal linear Paul trap 18
- 2.2 Transition rates of Ions in a Paul trap 20
  - 2.2.1 Spectroscopic properties of Be^+-Ions 21
- 2.3 Experimental Apparatus 22

3 IMAGING OF COULOMB CRYSTALS 25
- 3.1 Optics: Waves and Rays 25
  - 3.1.1 Maxwell's equations 26
  - 3.1.2 Wavefront aberrations 27
  - 3.1.3 Zernike Polynomials 28
  - 3.1.4 Point spread function 30
  - 3.1.5 Optical transfer function 30
  - 3.1.6 Modulation transfer function 31
  - 3.1.7 Resolution 31
  - 3.1.8 Paraxial ray tracing 31
  - 3.1.9 Matrix optics 32
  - 3.1.10 Design of aspheric surfaces 33
- 3.2 Detection of the fluorescence 34
  - 3.2.1 The EMCCD 34
  - 3.2.2 The PMT 36
- 3.3 Inter-ionic distance of trapped Be^+ Ions 36
- 3.4 Optical Design 37
- 3.5 Cryogenic Design 40
- 3.6 Optomechanical stress Tests 43
- 3.7 First Characterizations of the imaging system 43
  - 3.7.1 First images with the lens stack 44
  - 3.7.2 Characterization of the magnification 45
  - 3.7.3 Determination of the resolution 46
- 3.8 Lens alignment on the superconducting resonator 47

4 UPGRADES 51
- 4.1 Modification of the first Asphere 51
- 4.2 Replacement of the lens stack with a bi-aspheric lens 52
- 4.3 Design of a reflective Schwarzschild Objective 53

5 CONCLUSION AND OUTLOOK 59

A APPENDIX 63

B OPTOMECHANICAL DRAWINGS 67

ACRONYMS

BSM beyond the standard model

CaF2 calcium fluoride

CCD charged coupled device

CMOS complementary metal-oxide-semiconductor

CryPTEx cryogenic paul trap experiment

EBIT electron beam ion trap

EMCCD electron multiplying charged coupled device

HCI highly-charged ion

MPIK Max-Planck-Institut für Kernphysik Heidelberg

MTF modular transfer function

OSLO Optics Software for Layout and Optimization

OTF optical transfer function

PMT photo multiplier tube

PSF point spread function

PTB Physikalisch Technische Bundesanstalt Braunschweig

QED quantum electrodynamics

RF radio frequency

RFQ radio-frequency quadrupole

SM standard model of particle physics

UVFS UV fused silica

1 INTRODUCTION

Our current knowledge on the nature of matter and energy concludes within four fundamental interactions: The gravitation, the weak, strong and the electromagnetic. While the first one is implemented in Einstein's general relativity [1], the remaining three are covered by the Standard Model of particle physics (SM). Both frameworks have been very successfully tested and explain most of the known phenomena in a simple, elegant way [2]. However, due to the mathematical structure of these field theories, they seem to be highly incompatible with each other. To overcome their boundaries, extensions of the SM, a forest of so-called physics beyond the standard model (BSM) theories are proposed to explain e.g. matter/anti-matter asymmetries, neutrino masses, dark matter, and dark energy. Accompanied by some of these extensions is the variation of fundamental constants such as the proton to electron mass ratio $\bar{\mu} = m_p/m_e$ and the fine structure constant $\alpha = e^2/\hbar c$ [3, 4] or the presence of a stronger electric dipole moment in neutrons and electrons [5], which could also lead the way to the violation of Lorentz- and CPT-invariance [6]. Important evidence of a variation of α became an observation of the Very Large Telescope and the Keck Observatory: Within quasar absorption spectra in astrophysical hydrogen-clouds, a spatial variation of α on cosmological scales has been identified [7]. This "Australian-Dipole" has not yet been verified by other experiments due to its proposed drift of $\dot{\alpha}/\alpha \mid_{\text{lab}} \approx 10^{-19}$/yr on earth [8].

SM tests and searches for physics beyond the Standard Model are traditionally carried out in the high energy regime at TeV scales with collision experiments that lead to the discovery of new particles or the verification of predicted ones such as the Higgs boson. On the other end of the energy scale, high precision measurements at low energies resulted in stringent tests of physical theories like Quantum-electrodynamics (QED) [9–11]. Atomic electron transitions are known for their oscillatory behavior and their unique properties in a given environment. Thus, if experimental parameters like temperature, electrical, magnetic or gravitational fields do not change, the frequency of the natural line width does not change. Therefore they are auspicious candidates for reaching precisions down to 10^{-19} and moreover their transition frequency ν depends directly on the fine structure constant [12]:

$$\nu \simeq cR_\infty A(Z) F(\alpha) \tag{1}$$

Here, c is the speed of light, R_∞ the Rydberg constant, $A(Z)$ a dimensionless factor scaling with nuclear charge Z and $F(\alpha)$ a function depending upon the particular transition. While the coupling constant α characterizes the strength between electromagnetic interaction and matter, spectroscopy (the measurement of atomic transition lines) originates from a time where the nature of the light emitted from atoms was not fully understood.

The first observation of discrete lines in the continuous spectrum of the sun was published by Joseph von Fraunhofer at the beginning of the 19$^{\text{th}}$ century [13]. A few years later, Kirchhoff and Bunsen connected these lines to elements found on earth by burning sodium in a flame and comparing its emission lines with Fraunhofer's absorption spectra [14,15]. In 1913, Nils Bohr presented his famous model which describes electronic shells in an atom with quantized energy levels. In his theory, absorption or emission of a photon results in a shell transition of an electron. Finally, in 1940 and 50 years after the observation by Michelson and Morley [16], Sommerfeld explained the fine structure splitting in hydrogen by quantizing the angular momentum of atomic systems [17]. Such a system is described by

$$\nu_{hfs} \simeq c\, R_\infty\, A\,(Z)\, \frac{g_i}{\bar{\mu}}\, \alpha^2\, F\,(\alpha)\ . \tag{2}$$

and considers the gyromagnetic ratio $g_i = \mu_i/\mu_\mathrm{N}$ consisting of the nuclear magneton $\mu_\mathrm{N} = \hbar e/2m_\mathrm{p}$ and the nuclear magnetic moment μ_i. Today, the driving force of most spectroscopy experiments are photons carrying the energy needed to excite an electronic transition. Einstein proposed in his work "On the quantum theory of Radiation" different natures of absorption and emission of radiation and described for the first time stimulated, coherent and monochromatic emission of multiple photons. This insight was the fundamental step for the development of the first Laser in 1960 [18] and boosted an understanding of quantum mechanics by utilizing this new technology for spectroscopy experiments. With the development of the frequency comb by the group of Theodor Hänsch in 1998 [19] a direct measurement of optical resonances at highest precision became possible, such that at the present time, laser-spectroscopy of the $^2S_{1/2}(F=0) \rightarrow {}^2F_{7/2}(F=3)$ transition of single $^{171}\mathrm{Yb}^+$ ions confined in a linear RF quadrupole trap lately overcame already fractional systematic uncertainties of 3×10^{-18} [20].

In 1953, Wolfgang Paul proposed, that charged particles with specific charge-to-mass ratio q/m could be focused in two dimensions by exposing them to radio-frequency (RF) driven electric and magnetic multipole fields and developed the linear quadrupole mass spectrometer [21,22]. The realization of additional confinement in the third dimension [23,24] and therefore a trapping in a locally controllable environment with arbitrary long interaction times resulted in the awarding of the Nobel Price to Paul in 1989 together with Hans Dehmelt, who confined charged particles in a strong, homogeneous magnetic field by overlapping it with an electric quadrupole-field [25].

A challenging disadvantage of the most frequency standards based on atoms or singly charged ions is the lack of sensitivity to a variation of fundamental constants like α and their comparable high susceptibility to external disturbances. Thus it takes measurement times in the range of a year to reach relative accuracies down to 10^{-18}. If ions with different atomic numbers obtain the same valence electron and the same shell structure they are isoelectronic.

By moving along the isoelectronic sequence of hydrogen, the electronic wavefunction overlaps more and more with the nucleus due to a Z^{-1} scaling of the Bohr radius. As a result, e.g. the first order QED correction for the 1s-transition of hydrogen-like Uranium U^{91+} rises to 425 eV since it scales with $(\alpha Z)^4$ [26]. Also, perturbations such as the first (Z^{-1}) and second-order (Z^{-4}) Stark shift are heavily suppressed while parity violations scale with Z^5 due to the weak polarizability of an electron in the region around the nucleus. Such a multiply

Bohr radius	Z^{-1}
Polarizability	Z^{-1}
Electronic gross structure	Z^2
Fine structure	Z^4
Hyperfine splitting	Z^3
QED effects	Z^4
2nd order Stark effects	Z^{-4}

Table 1: Scaling laws for atomic properties of hydrogen-like ions [12].

ionized system is called highly-charged ion (HCI) and due to the enhanced relativistic contributions to its electronic binding energies of some transitions it is an excellent candidate to test a possible variation in α. In the observable, baryonic universe most of the atoms heavier than helium occur in highly ionized states and on earth, there are various methods to produce and store HCI to investigate their fundamental properties and gain knowledge of laboratory plasmas, which are found for example in fusion reactors. Cryogenic setups with temperatures down to 4 K increase the vacuum by orders of magnitude and allow for longer storage times due to reduced collision rates with the background gas. Most times this interaction is not only responsible for a transfer of kinetic energy, but also recombination and therefore can result in a loss of the HCI.

Due to the lack of an easily accessible level structure with fast cycling transition in the optical or UV regime cooling to the lowest possible state of a HCI in a Paul trap can only be achieved by interacting with a singly charged, laser-cooled ion. The possibility of cooling Ar^{13+} sympathetically with a single Doppler cooled Be^+ ion has been successfully proven within a cryogenic Paul trap environment [27,28]. Further investigations into the sideband cooling of such a mixed two-ion crystal via the Beryllium ion resulted in a reduction of the motional energies in the sympathetically cooled HCI to the ground state of the harmonic trapping potential [29]. Hence, spectroscopy of highly-charged ions with a fractional accuracy beyond 10^{-16} (and therefore an improvement of at least 9 orders of magnitude [30]) became a reachable goal in state of the art spectroscopy experiments.

Spectroscopy in Paul traps presupposes that even fractions of the photons emitted by the resonantly excited ions are detected. Visual observation has always been an important tool in science. While in early times the documentation of an experiment was only possible verbally or with manual drawings,

Figure 1: The first compound microscope made by Zacharias Janssen around 1606-1607. Taken from [31].

today nearly all scientific data is generated and archived electronically. Photography is not only a crucial method in astronomy or particle physics, but also in state of the art Paul trap experiments. While astronomers can measure and extract positions and magnitudes of stars, atomic physicists use photons emitted by ions and ion crystals for diagnostics, elaboration of dynamics within the crystal or state detection of the trapped ions [32, 33]. Underlying these measurement methods, an optical device is needed to project the geometry of an object onto a detector. Manufacturing techniques of quartz and theories on light have been developed since the time of ancient Egyptians and Mesopotamians [34]. While the first evidence on knowledge about magnification can be traced back to a written record of Seneca, who wrote "Literae quamvis minutae et obscurae per vitream pilam aqua plenam maiores clarioresque cernuntur" ("Letters, however small and indistinct, are seen enlarged and more clearly through a globe of glass filled with water"), the first magnifying lens was found in the 10th century in Arabia [35, 36]. By aligning two lenses within a sliding tube, the Janssen family invented the first primitive microscope in 1590 [36]. Within a short time, many types of microscopes were used for scientific research reaching magnifications up to 270 and even today they are crucial instruments in many fields of science and criminology [36]. In contrary to the at that time well-known law of reflection, the first experimental description of refraction was given in 1621 by Willebrord Snell. Fermat then published in *The Principle of Least Time* a mathematical description of refraction in different media by postulating that light always follows the shortest path in time. After the discovery of Newton in 1666 that white light can be decomposed into different colors by utilizing a prism, Christian Huygens not

only developed the foundations of a wave theory of light but also he could reproduce the known laws of reflection and refraction. Based on Huygens' ideas on an envelope wave and already well-known interference phenomena, Fresnel was able to describe diffraction phenomena caused by straight edges, small apertures, and screens. His laws on the propagation of polarized light through a crystal and formulation of a few simple assumptions on the nature of elementary waves together with Arago lead to the awarding of the Royal Society's "crown", the Rumford Medal in 1826 and are still of great significance today. James Clerk Maxwell could finally describe an electromagnetic wave in its completeness, without the use of any mechanical models. Important contributions to the descriptions of imaging defects were made in 1857 when Philipp Ludwig von Seidel mathematically decomposed first order monochromatic aberrations into spherical, coma, astigmatism, curvature and distortion. Zernike succeeded by publishing a more efficient description of aberrations by expanding wavefronts into a power series. This allowed not only to separate aberrations but also to increase the design performances of the optical apparatus by weighting them. Today, most, if not all, optics simulation programs use the polynomials of Seidel and Zernike to estimate and optimize wavefront aberrations of optical systems.

In this thesis, a microscope for imaging of up to 500 µm × 500 µm wide Be^+ Coulomb crystals trapped in a cryogenic Paul trap is presented. The trap together with the experimental apparatus is briefly introduced in Chapter 2. Optical design and simulations of the lens system were achieved in Optics Software for Layout and Optimization (OSLO). In addition to the 313 nm cooling transition of Be^+ the objective was designed to collect fluorescence of the Ar^{13+} M1 (441 nm) transition and the 235 nm resonance-enhanced two-photon ionization process of the Beryllium atoms. Seven of the eight lenses are located directly on top of the Paul trap at a 4 K stage and are commercially available. The supplementing, special fabricated, eighth, bi-aspheric lens is mounted on the 40 K heat shield [29]. For the cryogenic environment, a mounting system was developed together with the construction workshop of the Max-Planck-Institut für Kernphysik Heidelberg (MPIK) which is described in Chapter 3 together with the optical design. Besides keeping the lenses centered without breaking them while cooling down from room temperature to 4 K it is also possible to change the magnification in a range from 7.8× to 20× which is shown in Section 3.7.2, together with characterization measurements of the lens stack and resolution tests. Since financial limitations resulted in a system that is capable of fulfilling the requirements for imaging the trapped ions but by far not reaching physical limitations, further investigations and simulations of a diffraction-limited system are presented in Chapter 4.

2 THE CRYOGENIC PAUL TRAP EXPERIMENT

In this chapter, the experimental setup is briefly introduced. Theoretical foundations of the Paul trap are presented in a theory section 2.1. The transition properties of a stored ion are shown in Section 2.2. A short overview of the setup is given in 2.3.

2.1 THE LINEAR PAUL TRAP

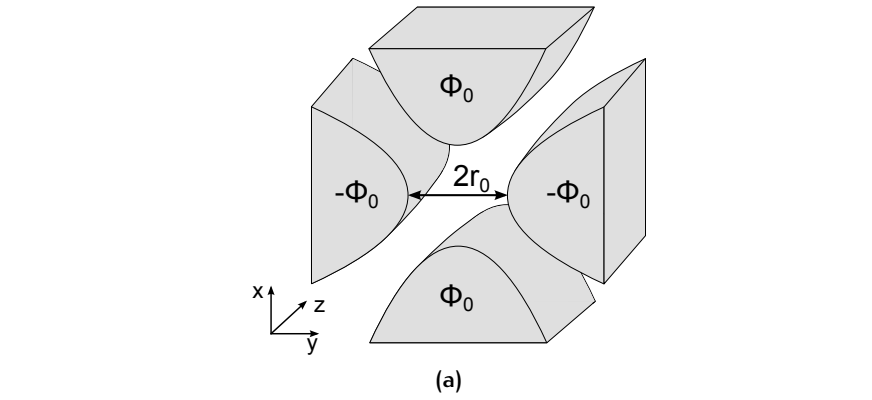

(a)

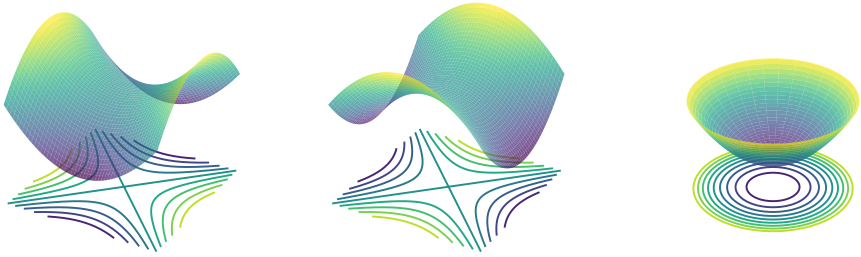

(b) $\Phi(t = 0)$ (c) $\Phi(t = \pi/\Omega_{RF})$ (d) Time average

Figure 2: a) Hyperbolic electrode configuration. Φ_0 is the applied electric potential, r_0 describes the distance between trap center and electrodes. Taken from [37] b)-d) Qualitative plot of the radial, RF-driven potential described in Equation 6. b) saddle potential at a given time $t = 0$; c) saddle potential at $t = \pi/\Omega_{RF}$; d) time averaged effective pseudo-potential. In addition the equipotential lines $x^2 - y^2 = const$ are projected onto the x-y plane.

Trapping ions can be achieved by utilizing the electric force

$$\mathbf{F} = -Q\nabla\Phi = -c\mathbf{r} \quad \text{with} \quad c = const. \quad . \tag{3}$$

As a consequence of Earnshaw's theorem, static electric fields alone cannot confine charged particles. Without losing generality, we define a general po-

tential $\Phi(x,y,z,t)$ which obeys a quadratic dependence in Cartesian coordinates (x,y,z) .

$$\Phi(x,y,z,t) = \Phi_0(t) \cdot (ax^2 + by^2 + cz^2) \tag{4}$$

If we neglect space-charges, we find the boundary condition $a + b + c = 0$ by applying Laplace's equation

$$\Delta\Phi = \frac{\partial^2\Phi}{\partial x^2} + \frac{\partial^2\Phi}{\partial y^2} + \frac{\partial^2\Phi}{\partial z^2} = 0 \quad . \tag{5}$$

This results in the solutions $a = -b$ and $c = 0$ if the ions have to be confined only in two dimensions, and $a = b$ and $c = -2a$ to trap ions in all three dimensions. Thus, in a linear trap configuration with hyperbolic trap electrodes shown in Figure 2a the time-dependent, harmonic electric field is given by

$$\Phi_{QP}(x,y,t) = \Phi_0(t)\frac{\left(x^2 - y^2\right)}{r_0^2} \tag{6}$$

In Figures [2b,2c] the radial electric potentials and their equipotential lines corresponding to Equation 6 at times $t = 0$, $t = \pi/\Omega_{\mathrm{RF}}$ along the quadrupole axis are qualitatively shown. Figure 2d shows the time-averaged (adiabatic approximation) potential. The time-dependent amplitude $\Phi_0(t)$ consists of a AC part V_{RF} with frequency Ω_{RF}

$$\Phi_0(t) = V_{\mathrm{RF}} \cos\left(\Omega_{\mathrm{RF}}\, t\right) \quad . \tag{7}$$

Axial confinement in z-direction is achieved by a segmentation of the quadrupole electrodes in at least three parts. By applying DC voltage U_{DC} to the end-cap electrodes which are located at a characteristic distance z_0 to the trap center, a static electric potential Φ_{DC} is generated. Using the confinement solutions one gets the total electric potential by superimposing static and time-dependent contributions:

$$\Phi(x,y,z,t) = V_{\mathrm{RF}} \cos\left(\Omega_{\mathrm{RF}}\, t\right) \frac{(x^2 - y^2)}{r_0^2} + \frac{\kappa U_{\mathrm{DC}}}{z_0^2}\left(-\frac{1}{2}(x^2 + y^2) + z^2\right) \quad . \tag{8}$$

Here, κ describes a geometric correction factor.

2.1.1 Equations of motion in an ideal linear Paul trap

Following from the total electric potential in Equation 8 the equations of motion for a particle with mass m and charge Q become

$$\begin{aligned} \ddot{x} - \left(\frac{Q\kappa U_{\mathrm{DC}}}{mz_0^2} + \frac{2QV_{\mathrm{RF}}}{mr_0^2}\cos\left(\Omega_{\mathrm{RF}}\, t\right)\right)x = 0 \\ \ddot{y} - \left(\frac{Q\kappa U_{\mathrm{DC}}}{mz_0^2} - \frac{2QV_{\mathrm{RF}}}{mr_0^2}\cos\left(\Omega_{\mathrm{RF}}\, t\right)\right)y = 0 \\ \ddot{z} + \frac{2Q\kappa U_{\mathrm{DC}}}{mz_0^2}z = 0 \end{aligned} \tag{9}$$

We now transform these equations using the parameters

$$\begin{aligned} a_x = a_y = -\frac{1}{2}a_z &= -\frac{4Q\kappa U_{\mathrm{DC}}}{mz_0^2\Omega_{\mathrm{RF}}^2} \\ q_x = -q_y &= \frac{4QV_{\mathrm{RF}}}{mr_0^2\Omega_{\mathrm{RF}}^2} \\ q_z &= 0 \\ \zeta &= \Omega_{\mathrm{RF}}\, t/2 \end{aligned} \tag{10}$$

and the differential equations reduce to Mathieu's equation

$$\frac{d^2}{d\zeta^2}u + (a_u - 2q_u\cos(2\zeta)) \cdot u = 0 \quad , \; u = x, y \quad . \tag{11}$$

The solutions of this equation of motion are separated into stable and unstable

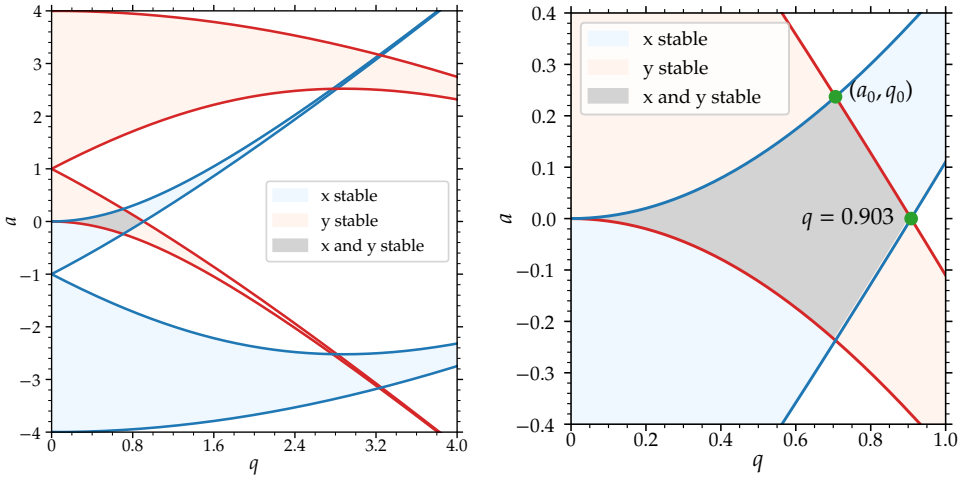

Figure 3: Stability diagram for a two-dimensional quadrupole mass spectrometer. The red and blue areas are showing the stable solutions of the Mathieu Equation 11 in x- and y-direction. In the gray area both solutions overlap and stable trapping in both directions is possible

trajectories. If the axial kinetic energy of the charged particle is smaller than κQU_{DC} only the static potential of the end-cap electrodes is necessary to store the ions in axial direction, while the stable solutions in radial x-y direction only depend on a and q. By definition these solutions are suitable for particles with similar Q/m-ratios such that different species can be stable confined. Figure [3a,3b] show stable solutions in the (a, q)-space. Symmetries occur for $a = a_x = -a_y$ and $q = q_x = q_y$. The gray area marks stable trajectories in both directions. In the stable region next to $(a = 0, q = 0)$ we approximate the solution of Mathieu's equation with $|a| \ll 1$ and $|a| \leq |q| \ll 1$ adiabatically and find

$$u(t) \cong u_1 \cos(\omega_u\, t)\left(1 + \frac{q_u}{2}\cos(\Omega_{\mathrm{RF}}\, t)\right) \tag{12}$$

with

$$\omega_u = \beta_u\Omega_{\mathrm{RF}}/2 \quad \text{and} \quad \beta_u = \sqrt{\frac{q_u^2}{2} + a_u}\,. \tag{13}$$

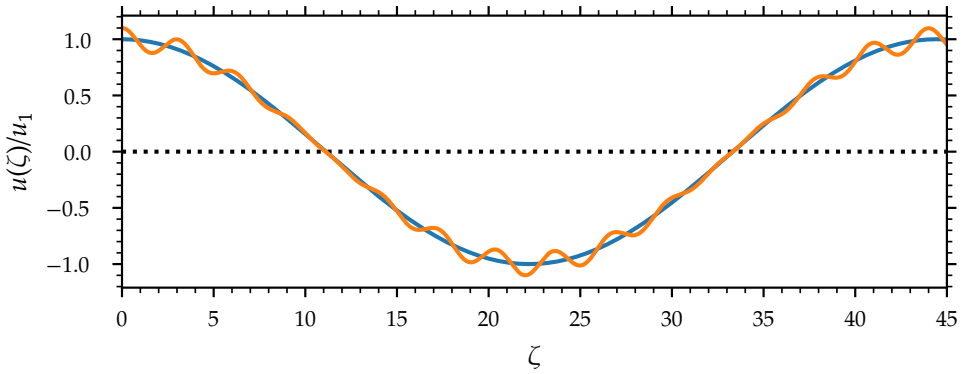

Figure 4: Trajectory of an ion in a Paul trap in $u = x, y$ direction, calculated for a radial Mathieu parameter $q = 0.2$ and $a = 0.0$ in dependence of $\zeta = \Omega_{\mathrm{RF}}\, t/2$. The blue trajectory shows only the slow secular motion while the orange curve represents secular and micromotion. The micro motion amplitude rises with increasing distance u to the centre of the quadrupole axis.

Within the parameter range $0 < \beta_u < 1$ a stable confinement can be achieved.

In axial direction the eigenfrequency of a single charged particle is given by

$$\omega_z^2 = \frac{2Q\kappa U_{\mathrm{DC}}}{mz_0^2} \tag{14}$$

while the radial motion is a product of a rapid micromotion at the trap drive frequency Ω_{RF} and a slower secular motion ω_u shown in Figure 4. On the trap axis the micromotion amplitude vanishes completely, while it maximizes to $u_1 q_u/2$ at the tipping points. Since the ion micromotion is driven by the RF potential only the amplitude of the secular motion u_1 can be directly reduced, for example with laser cooling.

2.2 TRANSITION RATES OF IONS IN A PAUL TRAP

An ion stored in a quadrupole potential holds a kinetic energy composed of the micromotion and the secular motion.Along the trap axis ($x = y = 0$) of an ideal trap ($q_z = 0$) it is according to (12) only given by the slower secular motion. Thus it is possible to reduce the amplitude and energy by laser cooling. The cooling rate depends on the lifetime of the excited state. For a two level system the energy separation is given by $E = \hbar\omega_0$. By coupling the ion to the electric field

$$\vec{E}(\vec{r}, t) = \vec{E}_0 \left[\exp\left(i\vec{k}\cdot\vec{r} - i\omega_{laser}t + i\phi_{laser}\right) + c.c.\right] \tag{15}$$

of the laser, which is approximated as a monochromatic, plain wave with wavevector $\vec{k}$ and frequency $\omega_{laser}/2\pi$ we can drive this transition. Such an interaction causes Rabi-Oscillations if $\delta = \omega_{laser} - \omega_0$ becomes sufficiently small. The population P_e of the excited state is then defined by

$$P_e(t) = -i\frac{\Omega_r}{\sqrt{|\Omega_r|^2 + \delta^2}} e^{-i\delta t/2} \sin\left(\frac{1}{2}\sqrt{|\Omega_r|^2 + \delta^2}\, t\right) . \tag{16}$$

Due to the finite lifetime τ of the excited state, a full description of the system is given by the optical Bloch equations. Rabi-Oscillations are damped, if the excited state decays spontaneously with its transition rate γ. For $t >> 1/\gamma$ the population P_e becomes stationary and the population probability becomes

$$P_e = \frac{|\Omega_r|^2/\gamma^2}{1 + 2|\Omega_r|^2/\gamma^2 + \left(2\delta/\gamma\right)^2} = \frac{s_0/2}{1 + s_0 + \left(2\delta/\gamma\right)^2} \quad . \tag{17}$$

with a saturation parameter

$$s_0 = 2\frac{|\Omega_r|^2}{\gamma^2} = \frac{I}{I_s} \tag{18}$$

which quantifies the relation of the laser intensity I and the saturation intensity of the transition $I_s = \pi hc/3\lambda^3\tau$. In equilibrium the photon scattering rate γ is given by

$$\Gamma = \gamma P_e = \frac{s_0}{2\,(1 + s_0)} \frac{\gamma}{1 + \left(2\delta/\gamma'\right)^2} \propto \frac{\left(\gamma'/2\right)^2}{\left(\gamma'/2\right)^2 + \delta^2} \tag{19}$$

which considers the power broadening factor of the laser $\gamma' = \gamma\sqrt{1 + s_0}$ and follows a Lorentzian if the laser detuning δ is varied.

2.2.1 Spectroscopic properties of Be^+-Ions

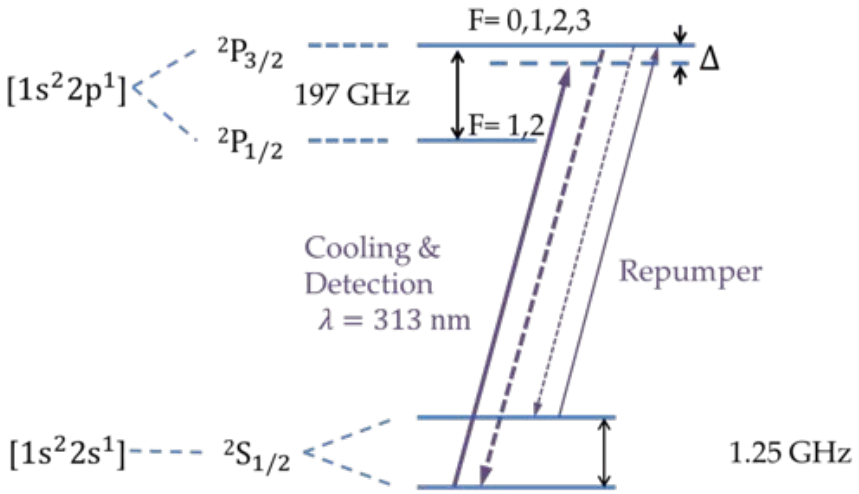

Figure 5: Level scheme of a Be^+ ion.

With the ground-state configuration [He]$2s^1$, a Be^+ ion possesses only a single valence electron and can be approximated as a quasi-single-electron system. Hence, the level scheme of the valence electron is comparably easy to access since the energy levels of the electrons within the closed shell are very well separated from the valence electron and no optical transitions within the closed shell occur. With angular momentum $L = 0$ and spin $S = 1/2$ the ground state is $^2S_{1/2}$. This level can be excited by a photon with wavelength $\lambda = 313\,\text{nm}$ into the P orbital, which obtains a fine-structure splitting of 192 GHz, due to

$L-S$ coupling. The two fine-structure levels are $^2P_{1/2}$ and $^2P_{3/2}$. With the current setup for laser cooling only the $^2P_{3/2}$ is accessed. This level has a lifetime of 8.2 ns which corresponds to a natural linewidth of $\Gamma/(2\pi) = 19.2\,\text{MHz}$, such that the $^2S_{1/2} \leftrightarrow^2 P_{3/2}$ transition is not only excellent for laser-cooling but also for the detection of the Be^+ ions. Since all states feature a hyperfine splitting due to the spin of the nucleus $I = 3/2$, the electron may decay into the $F = 1$ hyperfine state which is red detuned by 1.25 GHz from $F = 2$. Therefore needs to be transferred back into the P orbital by an additional repumper laser to keep the electron in the cooling cycle. A complete and explanation picture of this cycle can be found in [27]. In Figure 5 the relevant levels for laser cooling are shown.

2.3 EXPERIMENTAL APPARATUS

Figure 6: CAD rendering of CryPTEx II (bottom left), the beamline (bottom right), the XUV-Ebit (top right) and the XUV frequency comb (top left). Courtesy of Julian Stark.

In this section, the experimental apparatus which is shown in Figure 6, is briefly summarized. The goal of CryPTEx II is the confinement and cooling of different highly-charged ion species in an ultra-stable environment and finally the application of high-precision, XUV spectroscopy on the HCI. A compact,

room temperature EBIT is used to breed HCI, which are then extracted in bunches into a beamline to the Paul trap. For a further description and principle of operation of the EBIT I refer to [38]. Since EBITs always produce an ensemble of charge states, a time of flight separation with a kicker electrode according to the mass-to-charge ratio Q/m is applied in our setup. Deceleration to a kinetic energy of roughly 130eV/Q and pre-cooling of the bunch is achieved through two, separated pulsed drift tubes. I recommend [39], for details on a similar beamline installed at the first generation Paul trap, CryPTEx. A very important milestone in [39] is also the re-trapping technique which was applied for the first time on HCI. Inside the Paul trap, they are eventually re-trapped and sympathetically cooled down to 10 mK by a crystallized, laser-cooled cloud of beryllium ions [27]. To interrogate the HCIs with coherent XUV light, high harmonics are generated by an intensity amplified, frequency comb presented in [40]. To avoid recombination of the HCI and allow for reasonably long storage times up to hours, a background pressure $\ll 10^{-11}$ mBar needs to be reached [41, 42]. Therefore, a cryogen-free, vibration suppressing cryo supply system had been designed and assembled two times, one at the MPIK, the other one at the Physikalisch Technische Bundesanstalt Braunschweig (PTB). Both systems and their characteristics are described in [43]. The trap region is thermally uncoupled by two high purity, gold plated copper shields tied by radially mounted spokes, forming a 4 K within a 40 K region around the trap. Ions are trapped by utilizing a quasi-monolithic, superconducting niobium RFQ-resonator. Due to its superconducting character, it features extremely stable radio-frequency potentials which will lower the heating rates of trapped ions tremendously.

3 IMAGING OF COULOMB CRYSTALS

Most of the important observables of trapped ions inside a Paul trap, e.g. quantum states or the kinetic energy can be accessed via measuring the photons emitted by the cooled ion or the crystal, respectively. Therefore a crucial task is the collection and detection of light from the center of the trap. In this experiment, the singly charged $^9Be^+$ ions, which are needed for sympathetic cooling of most HCI, interact with UV lasers, while the highly-charged argon ion is excited in the optical regime. For a direct fluorescence detection of photons from both wavelength regimes using a lens-based imaging system, one has to account for the different refraction behavior of the glasses and use materials with high transparency in the UV. As an alternative, a reflective system could be used with the advantage of attaining independence to wavelength dependent imaging errors.

The prerequisites for the optical design process are given by the fixed working distance of 60 mm which had been reduced to 57 mm by modifying the slotted lid of the niobium resonator. In addition, a higher numerical aperture compared to the first generation experiment, CryPTEx, was required to increase the photon flux. Furthermore, a wavelength span from 235 nm to 441 nm needed to be accessed. Due to funding limitations the lenses should be commercially available and since they are located inside a cryogenic environment it was necessary to account for an intermediate focus in between a distance of 120 mm and 155 mm from the trap center to shield the 4 K stage from room temperature blackbody radiation using a small aperture. For typical pixel-sizes of 13 µm, a magnification of $M = 1$ would be already sufficient to resolve two ions which are separated by at least 26 µm. Modern Paul trap experiments, however, deal with inter-ionic distances down to 5 µm, which requires a higher magnification, that would lead to lower measurement errors of the distance. Therefore, the goal to reach became at least $M = 10$. On the optomechanical side it was necessary to provide a mounting mechanism which constrains the lenses with a constant force during the cool-down phase.

Throughout this chapter, the basic theoretical aspects of the optical design software are presented. Furthermore, properties of the detectors are briefly discussed as well as the optical and mechanical design. Finally, first tests, including a characterization of the magnification and resolution are shown.

3.1 OPTICS: WAVES AND RAYS

In this section, some of the important theoretical foundations of OSLO lens optics are presented, following the Lambda Research Corporation's "Optics Reference" [44] and "Principles of Optics" by Max Born and Emil Wolf [45]. The propagation of electromagnetic waves through an optical system is in most

cases described by using wavefronts or rays. Exceptions are focal regions or regions near aperture boundaries. In this section, the physical foundations are derived, starting from Maxwell's equations. In addition, common ray and wavefront models are briefly presented.

3.1.1 Maxwell's equations

The most fundamental way to describe the evolution of classical electromagnetic waves in space and time is given by Maxwell's equations, a set of four coupled first order partial differential equations, which hold at every point of a medium, whose physical properties are continuous. They couple the electric field $\boldsymbol{E}$ and magnetic induction $\boldsymbol{B}$ with the magnetic field $\boldsymbol{H}$ and the electric displacement field $\boldsymbol{D}$ by regarding the charge density ρ and the electric current density $\boldsymbol{j}$.

$$\nabla \times \boldsymbol{E} + \frac{\partial \boldsymbol{B}}{\partial t} = 0 \tag{20}$$

$$\nabla \times \boldsymbol{H} + \frac{\partial \boldsymbol{D}}{\partial t} = \boldsymbol{j} \tag{21}$$

$$\nabla \cdot \boldsymbol{D} = \rho \tag{22}$$

$$\nabla \cdot \boldsymbol{B} = 0\,. \tag{23}$$

From Ampere's law in Equation (21), one can directly see

$$\nabla \cdot \boldsymbol{j} - \nabla \cdot \frac{\partial \boldsymbol{D}}{\partial t} = 0$$

and by inserting Gauß' law (22)

$$\frac{\partial \rho}{\partial t} + \nabla \cdot \boldsymbol{j} = 0 \quad , \tag{24}$$

which demands charge conservation and shows up in an analogue relation in hydrodynamics as equation of continuity. By assuming a steady flux of radiation through an optical system, currents are present ($\boldsymbol{j} \neq 0$) and reaches a stationary state, in contrary to a static one, where all currents vanish.
Supplementing the four Maxwell equations (20)-(23) there are three relations which consider the behavior of materials under the influence of electromagnetic fields. Assuming a material as isotropic, resting and responding linear to the fields one can relate polarization and magnetization with $\boldsymbol{D}$ and $\boldsymbol{H}$ and find the constituent relations

$$\boldsymbol{D} = \epsilon \boldsymbol{E} \quad , \tag{25}$$

$$\boldsymbol{H} = \frac{1}{\mu}\boldsymbol{B} \quad , \tag{26}$$

$$\boldsymbol{j} = \sigma \boldsymbol{E} \quad , \tag{27}$$

where μ is the relative permeability, ϵ the permittivity and σ the specific conductivity of a given material. Inserting these material equations into Maxwell's one can derive a wave equation for the electric field. In this case the medium is homogeneous, resulting in the wave equation

$$\nabla^2 \boldsymbol{E} = \mu\epsilon \frac{\partial^2 \boldsymbol{E}}{\partial t^2} + \mu\sigma \frac{\partial \boldsymbol{E}}{\partial t} \quad . \tag{28}$$

In analogy to Equation (28) one finds the wave equation for the magnetic field. Some materials in optical designs are dielectrics. Then, the conductivity $\sigma \approx 0$ vanishes. Therefore, charges and currents can be neglected ($\boldsymbol{j} = 0$, $\rho = 0$) and the wave equation reduces to

$$\nabla^2 \boldsymbol{E} = \epsilon\mu \frac{\partial^2 \boldsymbol{E}}{\partial t^2} \quad , \tag{29}$$

with $v_{\text{ph}} = 1/\sqrt{\epsilon\mu}$ as speed of light in a medium. For a monochromatic wave with wavelength $\lambda = v_{\text{ph}}/\nu = 2\pi v_{\text{ph}}/\omega$ the simplest solution of (29) is assuming sinusoidal waveforms

$$\boldsymbol{E}(\boldsymbol{r}, t) = \boldsymbol{E}_r(\boldsymbol{r}) \exp(\pm i\omega t) \ . \tag{30}$$

This solution consists of a rapidly time varying term in the exponent and a slowly changing amplitude $\boldsymbol{E}_r$. Usually, the time-variation of $\boldsymbol{E}_r$ can be neglected, such that the wave equation reduces to Helmholtz' equation

$$\nabla^2 \boldsymbol{E} + k^2 \boldsymbol{E} = 0 \quad , \tag{31}$$

with wave-vector $k = \sqrt{\mu\epsilon}\omega = 2\pi/\lambda$. At the boundary between two homogeneous media the transverse direction of the propagation vector $\boldsymbol{k}$ does not change due to energy-momentum conservation. If the surface is perpendicular to the z-direction $k_{x1} = k_{x2}$ is postulated. Therefore, with the refractive index $n_i = \epsilon_i \mu_i$ Snell's law of refraction is derived immediately with

$$\begin{aligned} k_{x1} &= k_{x2} \quad , \\ n_1 k_0 \sin(\theta_1) &= n_2 k_0 \sin(\theta_2) \quad , \\ n_1 \sin(\theta_1) &= n_2 \sin(\theta_2) \quad , \end{aligned} \tag{32}$$

where $k_0 = \omega/c$ is the wavenumber and $c = 1/\sqrt{\epsilon_0 \mu_0}$ is the speed of light in vacuum. If incident angles are large enough, the $\sin(n_1/n_2)$ requires to become larger than 1 to fulfill Equation (32). In such cases, the ray is reflected at the surface. This critical condition is defined as $\theta_{\text{crit}} = \sin^{-1}(n_1/n_2)$ and well known as internal reflectance.

3.1.2 Wavefront aberrations

In the non-Gaussian regime of optics, each optical element added to a beam induces an error to the front of a traveling wave since at incident large angles a sine cannot any longer be approximated with $\sin\theta \approx \theta$. The wavefront is defined as a set of points with an equal phase. Aberrations are deviations from an object's geometry induced by an optical system. Classically, these are divided into two types: Chromatic aberrations, which describe the errors due to wavelength-dependent material properties and monochromatic aberrations, which are typically coma, astigmatism, spherical aberrations and distortions. The last are highly influenced by material tolerances, thicknesses and positioning of the lenses as well as apertures, focal length and magnification. Usually, all of these types coexist in a refractive optical system. A quantification of monochromatic imaging errors is usually done within a Seidel or Zernike analysis.

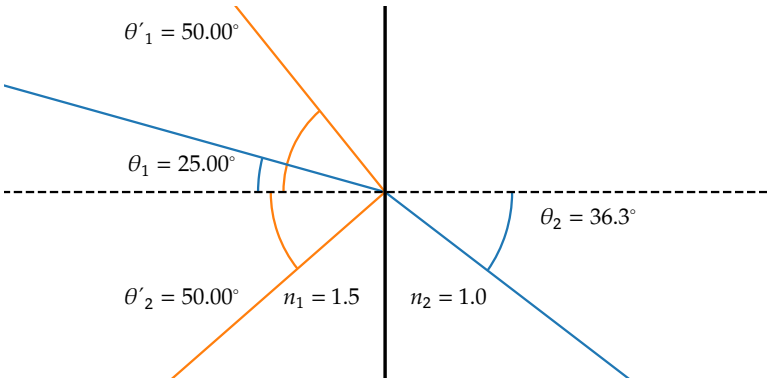

Figure 7: Illustration of Snell's law: Two rays (blue, orange) move through medium 1 with refractive index $n_1 = 1.5$. At the boundary of medium 2 ($n_2 = 1.0$) the blue ray with incident angle $\theta_1 = 25°$ is being refracted at an angle $\theta_2 = \sin^{-1}(n_1/n_2)\theta_1 = 36.3°$ while the orange is reflected since $\theta'_1 > \theta_{\text{crit}}$.

3.1.3 Zernike Polynomials

In a circular optical system the wavefront $W(x, y)$ can be decomposed into a series of polynomials. This set is complete and orthogonal over the interior of the unit circle. Thus, ($x = \rho\sin(\theta), y = \rho\cos(\theta)$) are expressed in polar coordinates to take advantage of the symmetries. The polynomial $Z(\rho, \theta)$ with radial and angular coordinates ρ and θ can be separated into a product of functions $R(\rho)$ and a complex exponential $G(\theta)$

$$Z_n^m(\rho\sin\theta, \rho\cos\theta) = R_n^m(\rho)\, G_m(\theta) = R_n^m(\rho)\, \exp(im\theta) \quad , \tag{33}$$

where $m \lessgtr 0$, $n \geqslant |m|$, $(n - |m|) \mod 2 = 0$ and $n, m \in \mathbb{Z}$. For the radial part the polynomials are given by

$$R_n^m(\rho) = \sum_{s=0}^{(n-m)/2} (-1)^s \frac{(n-s)!}{s!(\frac{n+m}{2} - s)!(\frac{n-m}{2} - s)!} \rho^{n-2s} \, . \tag{34}$$

They are normalized, $R_n^m(1) = 1$, and separable since they satisfy the relation

$$\int_0^1 R_n^m(\rho) R_{n'}^{m'}(\rho)\rho \mathrm{d}\rho = \frac{1}{2(n+1)}\delta_{nn'} \, .$$

Hence, the total wavefront aberration is given by

$$W(\rho, \theta) = A_0 + \sum_{n=1}^{\infty}\left[A_n R_n^0(\rho) + \sum_{m=1}^{n} R_n^m \left(B_{nm}\cos(m\theta) + C_{nm}\sin(m\theta)\right)\right] \quad . \tag{35}$$

with expansion coefficients A_n, B_{nm} and C_{nm}. Due to their orthogonality, the variance σ^2 of the wavefront aberration can be simply calculated and becomes

$$\sigma^2 = \sum_{n=1}^{\infty}\left(\frac{A_n^2}{2n+1} + \frac{1}{2}\sum_{m=1}^{n}\frac{B_{nm}^2 + C_{nm}^2}{2n+1-m}\right) \tag{36}$$

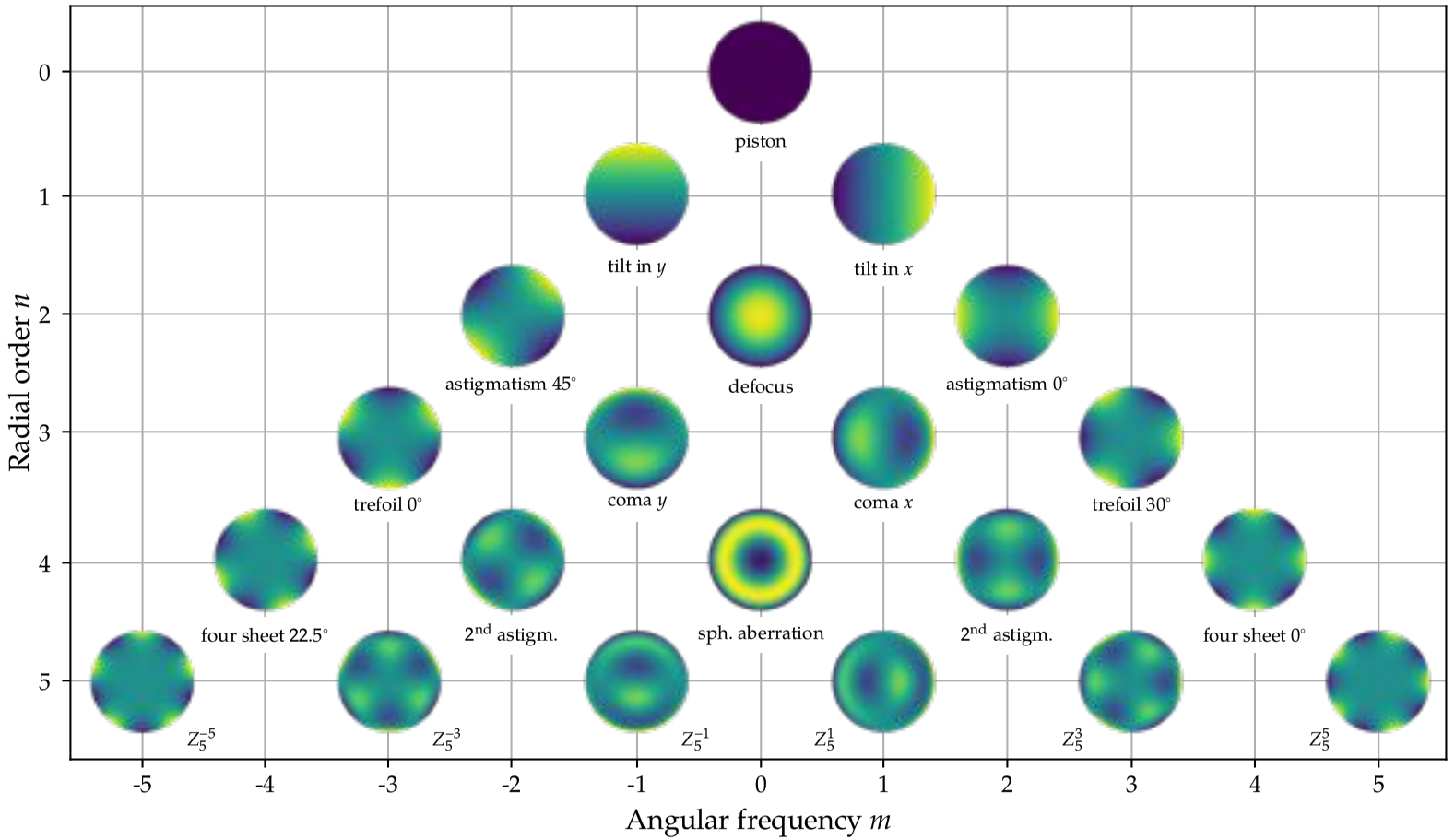

Figure 8: The first five radial orders of the Zernike polynomials $Z_n^m(r, \phi)$. By expanding $W(r, \phi)$ one can see, that the different terms contribute in a uniquely to the final wavefront, e.g. $(Z_0^0, Z_1^{\pm 1}, Z_2^0)$ are representing the image position, while $(Z_2^{\pm 2}, Z_3^{\pm 3}, Z_4^0)$ describe 3rd order distortions, such as spherical aberrations.

In Figure 8 the first five radial orders of the Zernike polynomials are shown. Each term contributes uniquely to the final wavefront. Here, the image position is defined by the Polynomials $Z_0^0, Z_1^{\pm}, Z_2^0$, while 3rd order aberrations can be represented with $Z_2^{\pm 2}$, $Z_3^{\pm 3}$ and Z_4^0. All included terms are weighted with the expansion coefficients and finally added to the final wavefront. Usually, these polynomials are integrated in an optics simulation software to quantify distortions and optimize the optical system.

3.1.4 Point spread function

A point in the object space is never projected onto a point in the image space but rather in a plane with position dependent intensity and can be quantified by the point spread function (PSF) [46]. If this function is known, a fundamental characteristic of an imaging system or a linear filter kernel is already given and one can calculate the shape of any 3D-object in the image plane. The response of an optical system to a point source at (x', y') in the image plane is described by

$$PSF(x', y') = E \tag{37}$$

depending only on the irradiance $E = |\Psi(x', y')|^2$. Here the integral over a pupil surface S

$$\Psi(x, y) = \int_S \Psi'(x', y') \exp\left(\frac{-i\,k\,\boldsymbol{x}\,\boldsymbol{x}'}{f}\right) \mathrm{d}S \tag{38}$$

defines the diffraction amplitude with (x, y) as a point on the image aperture, (x', y') as a point on the image plane and the focal length f. For example a pupil of a circular aperture with radius r which modulates a complex amplitude is described by a box function with

$$\Psi(x', y') = \Pi\left(\frac{|\boldsymbol{x}'|}{2r}\right); \quad \Pi(x) = \begin{cases} 1 & |x| \leq 1/2 \\ 0 & \text{otherwise} \end{cases}. \tag{39}$$

By Fourier transforming (39) the PSF becomes the Airy function

$$E(x', y') = |\Psi_0'|^2 = \Psi_0'^2 \left(\frac{I_1(kx'r)}{2kx'r}\right) \tag{40}$$

with I_1 representing the first order Bessel function. This PSF represents a point source which is perfectly imaged through a circular objective.

3.1.5 Optical transfer function

A direct integration of the PSF in the position-space is a costly operation which can be avoided since a convolution in the position-space corresponds to a multiplication in the Fourier space. Therefore, it is more suitable to transfer an object g_0 and the PSF h first into the fourier space, multiply them and project the image $\tilde{g}_i$ back into the position-space. The Fourier transform of the PSF $\tilde{h}$ is then called optical transfer function (OTF).

$$OTF(k) = \tilde{h}(k) \tag{41}$$

This decomposition of an object into periodic structures makes it an useful tool to quantify the image quality since it is independent of the object's geometry. Due to linearity and separation of the Fourier transform it also isolates the transversal and sagittal direction. However, it returns complex numbers and is therefore difficult to interpret.

3.1.6 Modulation transfer function

A more practical measurement value of the resolution is the absolute value of the OTF, the modular transfer function (MTF).

$$MTF = |OTF| = |\tilde{h}(k)| \tag{42}$$

This value obtains only a real part and neglects phase shifts of the optical system. It can be cheaply calculated due to Parsevals theorem

$$\int_{-\infty}^{\infty} |x(t)|^2 \mathrm{d}t = \int_{-\infty}^{\infty} |\tilde{x}(\omega)|^2 \mathrm{d}\omega \tag{43}$$

with the MTF it can be directly determined in which way the frequencies in the fourier domain are modulated. With increasing wavenumber the contrast is reduced inversely. For objects separated by $d = \lambda/2NA$ which is often referred as the Abbe limit the MTF is cut off.

3.1.7 Resolution

In section 3.1.4 the PSF for a perfect, circular objective was presented in equation (40). The zeroth order maximum contains 83.9% of the energy and is surrounded by multiple rings. To be able to distinguish between two point-like sources, they need to be separated by at least

$$d = 1.22 \frac{\lambda}{2NA} \quad , \tag{44}$$

which is the distance from the maximum to the first minimum of the Airy function. This limit is illustrated in Figure 9. For a system with $NA = 0.365$, the minimal distance d at a wavelength of $\lambda = 313\,\mathrm{nm}$ is $d = 0.512\,\mu\mathrm{m}$, which corresponds to a MTF cut-off at 1953 cycles/mm or 153.1 cycles/mm at a magnification of $M = 12.7$.

3.1.8 Paraxial ray tracing

Propagation of rays through optical systems are calculated numerically with the *yui* method. In this section, all unsigned variables are in front while all signed are behind a surface j. The medium's refractive index is given by n_j and the incident ray is defined by the slope u_j and its location on the surface, the distance y_j from the optical axis. The surface incident angle is then defined as

$$u_j = \frac{y_j - y_{j-1}}{t_j} \tag{45}$$

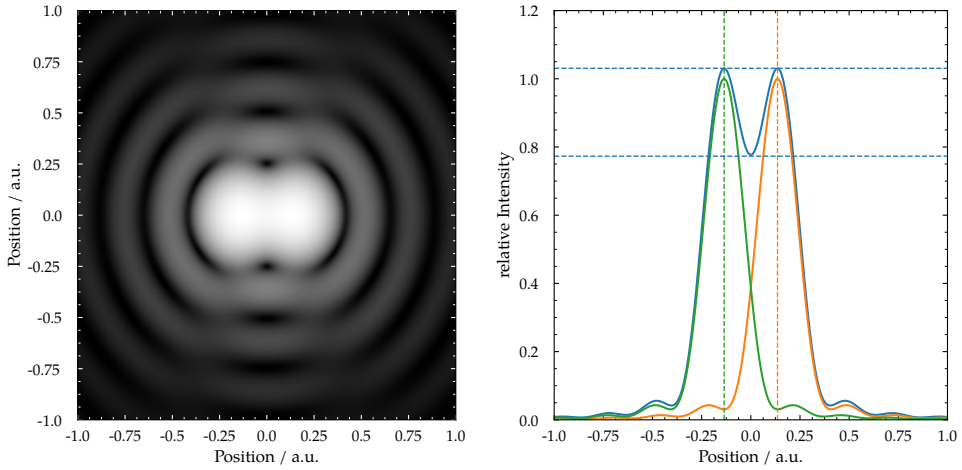

Figure 9: Qualitative illustration of two points, which are separated by the Rayleigh limit. On the left side the simulated image is shown with logarithmic intensity to increase the contrast to the diffraction rings. On the right side the linear intensity profile along $y = 0$ is shown.

The outgoin, diffracted ray on the next surfaces becomes

$$y_j = y_{j-1} + t_j u_j \tag{46}$$

where t_n is the distance between the two surfaces n and $n-1$. In a general form, the angle on the tangent of the surface can be described by

$$\begin{aligned} I_j &= U_j + \theta_j \\ I'_j &= U'_j + \theta_j \quad . \end{aligned} \tag{47}$$

Within the paraxial limit ($\sin\theta \approx \theta,\ \tan\theta \approx \theta,\ \cos\theta \approx 1$) one can write

$$\begin{aligned} i_j &= \frac{y_j}{r_j} + u_j = y_j c_j + u \quad , \\ i'_j &= \frac{y_j}{r_j} + u'_j = y_j c_j + u' \quad . \end{aligned} \tag{48}$$

Snell's law can therefore be described by

$$n_j i_j = n'_j i'_j \tag{49}$$

and it is also convenient to rewrite the slope as:

$$u' = \frac{n_j u_j - y_j \phi_j}{n'_j} \tag{50}$$

with $\phi_j = c_j(n'_j - n_j)$ being the power of the surface.

3.1.9 Matrix optics

A convenient way for a fast calculation is to rewrite the single ray trajectories into vectors and matrices. A single ray is the given by

$$\boldsymbol{R}_{j+1} = \begin{bmatrix} y_j \\ n\prime_j u\prime_j \end{bmatrix} \quad . \tag{51}$$

By passing through a surface it is translated using

$$\boldsymbol{T}'_j = \begin{bmatrix} 1 & t'_j/n'_j \\ 0 & 1 \end{bmatrix} \quad , \tag{52}$$

which results in

$$R_{j+1} = \boldsymbol{T}'_j R'_j \quad . \tag{53}$$

For a whole optical system with k surfaces the transfer matrix is given by

$$\boldsymbol{M}_{kl} = \begin{bmatrix} A'_{kl} & B'_{kl} \\ C'_{kl} & D'_{kl} \end{bmatrix} = \boldsymbol{R}_k \boldsymbol{T}_k ... \boldsymbol{T}_1 \boldsymbol{R}_1 \tag{54}$$

with coefficients A, B, C, D which compactifice the formulation since they need to be calculated only once for an optical geometry.

3.1.10 Design of aspheric surfaces

Most optical lenses and mirrors have a plane, spherical and paraboloidal surface due to the comparably easy manufacturing process. However, this restriction on simple surfaces does limit the overall performance of the optical system. For this reason, more complicated, aspheric surfaces are sometimes employed in certain systems. By adding aspherics to a system, in principle any centered system can become stigmatic, but also aplanatic for a specific wavelength. The surface profile of an asphere is often of the form of an superimposed Taylor expansion of z:

$$z(r) = \frac{r^2}{R\left(1 + \sqrt{1 - (1+\kappa)\frac{r^2}{R^2}}\right)} + \alpha_4 r^4 + \alpha_6 r^6 + ... \quad , \tag{55}$$

where κ is the conic constant, R the radius of the lens with curvature $c = 1/R$, r the radial distance from the optical axis and α_i aspherical coefficients. The conic constant defines the surface shape which is shown in Table 2. Usually

Conic constant	Surface shape
$\kappa = -1$	paraboloid
$\kappa < -1$	hyperboloid
$\kappa = 0$	sphere
$\kappa > 0$	oblate ellipsoid
$0 > \kappa > -1$	prolate ellipsoid

Table 2: Surface shapes of an asphere depending on the conic constant κ.

these kinds of lenses are designed to reduce the number of lenses and make the optical system more compact. In addition, aberrations of the total system can be reduced or removed.

Lens design in OSLO

Within OSLO it is possible to design and optimize aspheric surfaces with coefficients up to the nth order. The most convenient way to start is by adding a single lens (two surfaces) to the file. Usually, it is necessary to start with a common spherical lens to get an idea of the curvature. Then, in the "Special" column of the lens spreadsheet editor, it is necessary to activate the "Conic" option. After that, an aspheric shape needs to be chosen. Usually, the "Polynomial Asphere" is a sufficient option. However, if more aspheric coefficients are needed the "Standard Asphere" should be used. Within the "Optimize" window, "Variables" have to be assigned to the coefficients of the lens surface. At this point, no restrictions have to be chosen. With the "Slider-wheels" the surface can be roughly optimized. For the starting values of the aspheric coefficients small values should be chosen (e.g. $\alpha_4 \approx \pm 10^{-7}$, $\alpha_6 \approx \pm 10^{-9}$, $\alpha_8 \approx \pm 10^{-12}$, $\alpha_{10} \approx \pm 10^{-15}$). The next step is fixing the "Variables" to roughly the same order of magnitude of the actual values. In this work, an aberration based error function was defined with "Optimize > Generate error function > Aberration operands" to optimize the whole setup. In the beginning, the operand weights are equally set to 1. Within the definition column, an arithmetical operand and a constant can be added. This is of importance if e.g. the focal length needs to be fixed. The "Optimize > Iterate" function starts the error function minimization. If the system converges and focuses the rays properly onto the predefined image plane it needs to be checked if any variable reached the boundary condition. Furthermore, aberration weights can be adjusted to modify the system. After a few iterations, the lens or objective should reach its global minimum absolute error. Further surfaces can be added and the whole system can again be optimized step by step.

3.2 DETECTION OF THE FLUORESCENCE

A typical photon collecting detector is a photo multiplier tube (PMT) which is sensitive to single photons but not able to resolve in space while a charged coupled device (CCD) can spatially resolve the ions, but produces in many cases too much noise to detect and count single photons. In our setup we combined a PMT [1] of the company HAMAMATSU and a comparably fast electron multiplying charged coupled device (EMCCD) from Andor [2] to be able to measure not only small count rates as well as variations in fluorescence but also spatially resolve the Be^+ ions.

3.2.1 The EMCCD

Due to the low-light conditions it is mandatory to use a low noise detector. An EMCCD removes the noise limitation of the output amplifier and the video chain electronics, which is the typical limitation of any CCD. This can be achieved by applying a gain process which introduces low noise, right before the charges

1 *H10682-210*
2 *iXon Ultra 888*

are converted to voltages. The noise of a conventional, scientific CCD can be expressed as

$$\sigma_{CCD} = \sqrt{\sigma_{RN}^2 + \sigma_{DN}^2 + \sigma_{CN}^2 + \sigma_{SHOT}^2} \quad , \tag{56}$$

where $\sigma_{DN} = \sqrt{I_{DN}\, t_{Exp}}$ is the dark current noise depending on the exposure time t_{Exp} while σ_{RN} is the read-noise of the chip. Since the dark current $I_{DN} \propto T^{3/2} \exp\left(-E_g/(2k_BT)\right)$ is purely statistical and depends on the temperature T of the sensor a convenient way to reduce this kind of noise is cooling down the CCD with liquid nitrogen or a thermoelectric cooler. Here k_B is the Boltzmann constant and E_g the band gap of the semiconductor. Another statistical process due to the quantized nature of electrons and photons is $\sigma_{SHOT} = \sqrt{D_{QE}\, N_{Ph}}$, the shot noise with quantum efficiency D_{QE} and number of photons N_{Ph}. In addition the transfer of the stored electrons can induce tunneling effects, which causes a clock-induced-charge noise σ_{CN}. In contrary to a conventional CCD, the EMCCD obtains a gain register placed between the shift register and the output amplifier. Due to electron impact ionization, in each stage of the gain register a secondary electron can be released with probability $p \approx 2\%$. The overall gain is then defined as $g = (1+p)^{N_{Reg}}$ at one of N_{Reg} stages in the gain register. Therefore the noise signal needs to be modified to

$$\sigma_{EMCCD} = \sqrt{\sigma_{RN}^2 + F^2 g^2 (\sigma_{DN}^2 + \sigma_{CN}^2 + \sigma_{SHOT}^2)} \quad . \tag{57}$$

By approximating the excess noise factor $F^2 \approx 2$ [47] one now estimates the signal-to-noise ratio SNR_{EMCCD} with a signal $S = gD_{QE}N_{Ph}$ to

$$SNR_{EMCCD} = \frac{D_{QE}\, N_{Ph}}{\sqrt{\sigma_{RN}^2/g^2 + 2\,(\sigma_{DN}^2 + \sigma_{CN}^2 + \sigma_{SHOT}^2)}} \quad . \tag{58}$$

If typical small contributions of σ_{CN} and σ_{DN} are neglected and high gains are applied then the SNR in the shot noise limited regime reduces to

$$SNR_{EMCCD} = \frac{D_{QE}\, N_{Ph}}{\sqrt{2 D_{QE}\, N_{Ph}}} \quad , \tag{59}$$

which is lower by a factor of $\sqrt{2}$ compared to a conventional CCD. If the laser is tuned on resonance, the 313 nm cooling transition rate for a single Be^+ is $\Gamma/(2\pi) = 19.2$ MHz. By assuming an entry lens with numerical aperture $NA = 0.4$ the photon flux through the optical system becomes $\Phi = 9.62{\cdot}10^5$photons/s. Since each of the nine optical elements (eight lenses, one window) absorbs roughly 5% of the incident photon flux at each detector is reduced to $\Phi_{Det} = 2.35{\cdot}10^5$photons/s. If 60% of the flux is focused onto a 8×8 pixel area, the signal on each pixel is $S = D_{QE}\, N_{Ph} = 770$ with an exposure time of $t_{Exp} = 1$ second and a quantum efficiency of $D_{QE} = 35\%$. Therefore the corresponding signal-to-noise ratio is $SNR_{EMCCD} \approx 20$ and even for an exposure time of 0.1 s still about 6.

Andor's back illuminated *iXon Ultra 888* is equipped with a Peltier element which cools the $1024 \times 1024\, px^2$ E2V sensor down to an operating temperature of $-75^{\circ}C$ and therefore reduces the dark current to a level orders of

magnitudes below 1 $e/px/s$. A UVB coating and sealing in a vacuum guarantees a sensor quantum efficiency of 35% at 313 nm. The well depth of each of the 13 µm × 13 µm wide pixel is 86200 e/px with a clock induced charge of $2.24 \cdot 10^{-3}$ events/px [48]. Due to the size of the pixel the maximum resolution at a magnification $M = 12.7$ is $d_{EMCCD} = 2px/M = 2.05\,\mu m$ according to Nyquist's theorem.

3.2.2 The PMT

In general a PMT amplifies the signal of an electron released from a photo electrode by an incident photon due to the photo effect. Amplification is achieved by accelerating the photo-electron onto another electrode called a dynode. At impact, secondary electrons are emitted and again accelerated towards another dynode. This process is repeated multiple times until roughly 10^6 electrons are generated. An anode then collects the electrons and generates an electric signal which is sent to a data acquisition system. In theory, it could be possible to detect less than a photon per second, however dark counts due to the electronics or cosmic rays induce always an error signal of statistical nature which needs to be considered. On the other side, the maximum count rate is usually limited by the time between the generation of the photo-electron and neutralization of the current at the anode. This characteristic is called pulse-pair resolution or dead time. In the last subsection it was calculated, that the photon flux on each detector will be about $\Phi_{\text{Det}} = 2.35 \cdot 10^5$photon/s at 313 nm wavelength. Therefore the installed PMT is suitable since its pulse-pair resolution is typically 20 ns which corresponds to a saturation count rate of $5 \cdot 10^7$/s.

3.3 INTER-IONIC DISTANCE OF TRAPPED Be^+ IONS

By estimating the inter-ionic distance inside the trap, an upper resolution limit of the optical system can be calculated. For a single chain of N trapped ions of charge Q and mass m, the position $z_i(t)$ of the i-th ion can be calculated with the static harmonic potential [49]

$$V = \sum_{i=1}^{N} \frac{1}{2} m\omega_z^2 z_i(t)^2 + \sum_{i \neq j}^{N} \frac{Q^2}{8\pi\epsilon_0} \frac{1}{|z_i(t) - z_j(t)|} \quad . \tag{60}$$

By assuming that the ions are thermalized they are oscillating only around an equilibrium position such that the ion positions are given by:

$$N = 2: \quad z_{1,0} = -\sqrt[3]{\frac{Q^2}{16\pi\epsilon_0 m\omega_z^2}}, \qquad z_{2,0} = \sqrt[3]{\frac{Q^2}{16\pi\epsilon_0 m\omega_z^2}} \quad ,$$

$$N = 3: \quad z_{1,0} = -\sqrt[3]{\frac{5Q^2}{16\pi\epsilon_0 m\omega_z^2}}, \qquad z_{2,0} = 0, \qquad z_{3,0} = \sqrt[3]{\frac{5Q^2}{16\pi\epsilon_0 m\omega_z^2}} \quad .$$

For higher N the solutions have to be computed numerically [50]. Assuming a trap frequency $\omega_z/2\pi = 1.2$ MHz, two singly ionized beryllium ions with mass $m_{\text{Be}} = 9$ u are separated by $d_{N=2} \approx 27.8\,\mu m$, while for three ions the distance is $d_{N=3} \approx 23.8\,\mu m$. It was shown that the separation scales with $N^{-0.559}$ for large ion chains [50].

3.4 OPTICAL DESIGN

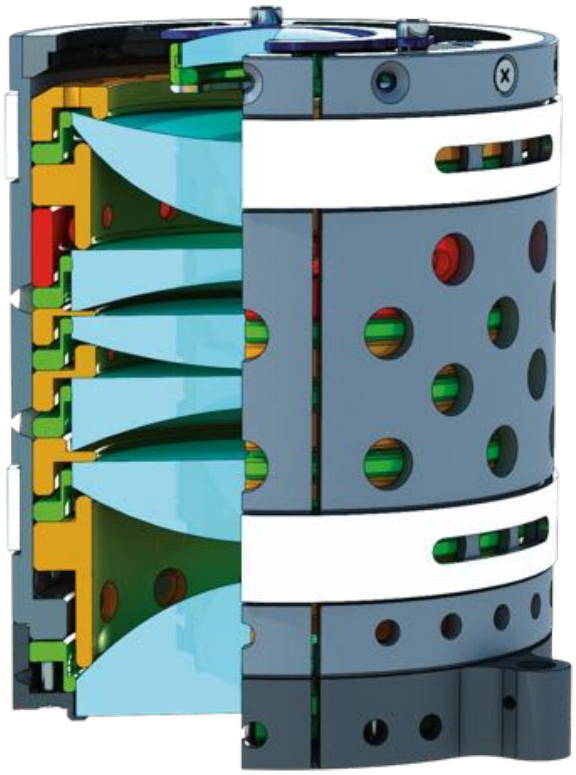

Figure 10: Illustration of the lens stack. At the bottom in dark gray a mounting ring is fixed by four M3 screws on top of the niobium resonator. Twelve M2 screws hold the cage (gray) which centers the rings inside the tower. The green rings, also shown in Figure 14, are designed to clamp and center the lenses while not destroying them in the cool down phase. Orange rings separate the lenses axially and the red ring prevents destruction due to axial pressure by the thrust pieces shown together with the top ring colored in black in Figure 15.

In this section the optical and geometrical design processes of the imaging system are discussed, starting with the given prerequisites. The behavior of the chosen materials is introduced and the final design calculated in OSLO presented. During the commissioning of CryPTEx II it is planned to sympathetically cool Ar^{13+} with beryllium ions. Therefore the detectors explained in Section 3.2 need access to the Be^{+} cooling transition at 313 nm and the Ar^{13+} M1 spectroscopy line at 441 nm. In addition, the 235 nm resonance enhanced two-photon ionization of $^{9}Be^{+}$ needs to be detected for diagnostics. In the UV range, transmissions of more than 90 % are only achievable with a few glasses such as UV fused silica (UVFS), calcium fluoride (CaF2) and sapphire. However, refractive optical systems cause chromatic aberrations and internal reflections, which produce stray light. Thus in the beginning of the design studies reflective Schwarzschild objectives [51] had been considered. Since the secondary mirror for a system with numerical aperture $NA = 0.4$ would have been located within the resonator and could have compromised the high qual-

ity factor. This type of system had been neglected in the further studies. In addition, the field of depth of theses kinds of optical systems is reduced due to the comparably low focus length. However, a system with $NA = 0.26$ and an optimized obscuration ratio is presented in Chapter 4.

The minimal working distance is given by the niobium flange on top of the

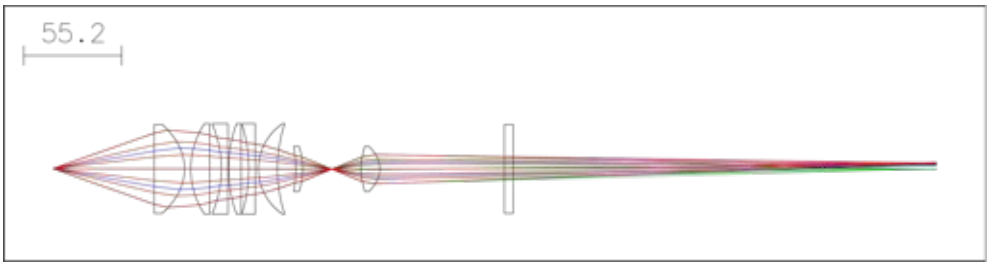

Figure 11: Drawing of the whole optical system, which was designed in this work. With a working distance of 57 mm, the stack on the left is directly mounted on top of the resonator. In between the first seven lenses at 4 K and the bi-asphere at 40 K an intermediate focus enables effective shielding of blackbody-radiation from room temperature. The magnification in the commissioning phase was set to $M = 12.7$. With a design wavelength of 313 nm, Be^+ ions can be spatially resolved on a detector.

resonator lid and was reduced by decreasing the wall thickness of the outer ring by 2 mm and cutting another 1.5 mm off the grid. Therefore, the distance from the first lens to the trap center is only 57 mm. Thus, a single aspheric lens with focal length $f = 60$ mm and $NA = 0.365$ could serve as photon collector and directly refocus on a CCD or a PMT outside the vacuum through a single window. Due to the cryogenic trap environment this would have caused a tremendous input of blackbody radiation not only on the ions, but also on the 4 K stage. Additional lenses were introduced to refocus the fluorescence of the ions to an intermediate focus at a pinhole between the 4 K and 40 K stage at a distance of 157 mm from the trap center. To achieve this for the given wavelength range with limited financial resources, a set of six commercially available lenses and additionally one special model of a concave lens presented in Table 3 were selected. With the assumption of a single lens refocusing the photons to the intermediate focus, a chromatic aberration can be estimated. With the lensmaker equation

$$\frac{1}{f} = (n-1)\left(\frac{1}{R_1} - \frac{1}{R_2} + \frac{(n-1)\,d}{nR_1R_2}\right) \tag{61}$$

one can calculate the different foci for a perfect lens. At room temperature, the refraction indices are given by:

Material	$n_{235\,\mathrm{nm}}$	$n_{313\,\mathrm{nm}}$	$n_{441\,\mathrm{nm}}$	Source
Fused Silica (293.15 K)	1.5166	1.4844	1.4663	Malitson (1965) [52]
Calcium Fluorite (293.15 K)	1.4734	1.4517	1.4392	Malitson (1963) [53]

This results in a dispersion of roughly 13 mm between $f_{235\,\mathrm{nm}}$ and $f_{441\,\mathrm{nm}}$ for a lens with a back-focus of 87 mm. Therefore a pinhole of a few millimeter

Table 3: Description of the used lenses starting with an asphere fabricated by the company Edmund Optics as first element next to the trap center. The first seven lenses are stacked in a tower on top of the niobium resonator at 4 K. Lens 8 is located behind the intermediate focus at the 40 K stage and refocuses the fluorescence to the EMCCD and the PMT outside the vacuum.

Lens	Type	Material	Name	Manufacturer
1	asphere	UVFS	67268	Edmund Optics
2	convex	UVFS	SPX043	Newport
3	concave	CaF2	67112	Knight Optical
4	convex	UVFS	PCX-50.8U-150	Lambda Research
5	concave	CaF2	112-5519E	Eksma Optics
6	p. meniscus	UVFS	LE4412	Thorlabs
7	p. meniscus	CaF2	LE5414	Thorlabs
8	bi-asphere	UVFS	Custom	Aspheriicon

diameter in the 313 nm focus would absorb most 235 nm and 441 nm fluorescence photons. To reduce this kind of aberration the concave lenses are made of calcium fluorite. Simulations in OSLO have shown, that the dispersion of the effective focus behind the 1″-meniscus lens was reduced to $\Delta f = 2.6\,\mathrm{mm}$. This allows all important wavelengths to pass a diaphragm with 2 mm diameter.

After selecting types and materials of the lenses and reducing chromatic aberrations, the 313 nm cooling transition focus was optimized, since it will be used to image and localize the ion crystals. The object radius was set to 250 µm and all aberration weights have been equally set to 1. Before starting the optimization algorithm, lens distances were chosen to be variable. After some non converging approaches the curvature of lens 3 was identified to cause this problem. Therefore it became variable since the number of commercial available concave CaF2 lenses with this size and radius were very limited. The final parameters of the stack are presented in Table 4.

With the given parameters in Table 4, the typical optical characteristics can be simulated. The point spread function analysis of the lens stack is shown in Figure 12. Here, the Strehl ratio is calculated to be 0.13 on-center which is far from the diffraction limit > 0.839. In addition, the contrast is lost if the point source is located off center. This can be caused by coma, which is also revealed by the wavefront analysis in Figure 13. Since the peak spreads and is projected off-center on the camera. However, the patch size is smaller than one pixel ($\mathrm{px} = 13\,\mu\mathrm{m}$) and about 85% of the fractional energy is always irradiated on a 3×3 pixel-grid, which is at this point sufficient. Behind the intermediate focus a 1" bi-asphere is used to refocus the photons onto the detectors. The diffraction limited lens was originally designed for the twin experiment at the PTB [29]. Since two more spare lenses were ordered it was possible to use one of them for this setup. In this optical design of the work,

Table 4: Alignment of the lens stack optimized by OSLO with number of Surface, radius of the curvature, thickness, aperture radius in millimeter and the materials.

Surface	Radius	Thickness	Aperture Radius	Glass
Obj	–	57.00	0.25	Vacuum
ASP	∞	17.00	20.15	UVFS
2	–	3.50	25.00	Vacuum
3	45.90	10.67	25.40	UVFS
4	∞	6.58	25.40	Vacuum
5	−63.50	3.60	25.40	CaF2
6	∞	0.50	25.40	Vacuum
7	76.28	7.00	25.40	Silica
8	∞	4.30	25.40	Vacuum
9	−83.60	3.60	25.40	CaF2
10	∞	1.84	25.40	Vacuum
11	30.60	10.70	25.40	UVFS
12	80.90	10.25	25.40	Vacuum
13	−75.90	4.00	12.70	CaF2
14	−40.00	0.00	12.70	Vacuum
FOC	–	32.65	0.22	Vacuum

the lenses properties are used to avoid additional aberrations. Furthermore, it can be used to increase or decrease the magnification by changing the distance to the intermediate focus. This will, however, decrease the flux of the 235 nm and 441 nm fluorescence since these wavelengths are not any longer properly refocused onto the detectors. Since the M1 transition of Ar^{13+} cycles at 100 Hz, it is mandatory to decrease the magnification to $M = 7.8$, which corresponds to a distance of 11.6 mm to the focus. A window was designed to pass the refocused beam out of the vacuum chamber. The thickness of the UVFS substrate with 38 mm diameter is 9.5 mm. Stray-light due to reflections is reduced to 0.1% at 313 nm by coating all surfaces with a *V*-coating.

3.5 CRYOGENIC DESIGN

After finishing the optical design, a system needed to be designed to support the lenses and keep them in position. Due to the large difference between room temperature and the 4 K/40 K stages, a standard lens mount might destroy the lenses in the cool-down phase. In Table 5 the scalings of the typical materials used in this setup are shown. One can see, that the thermal compression integral of fused silica is nearly 0. Thus, mounted on an inflexible socket, the UVFS lenses would burst due to the radial pressure of the shrinking holder material. As a solution an aluminum ring shown in Figure 14 with 40 small arms was developed together with the MPIK construction and the workshop. A complete set of arms is able to fixate and center the lens in radial direction and a decent amount of force is needed to push the lens in and

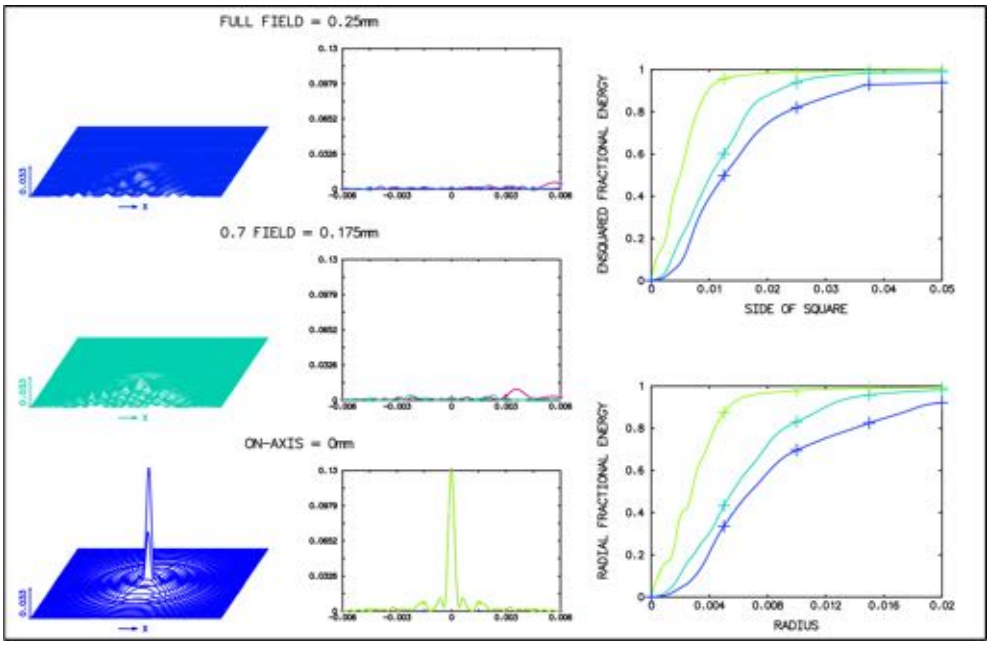

Figure 12: Analysis of the PSF on- and off-axis for the lens stack with lenses 1 – 7. On axis the Strehl-ratio is simulated to be 0.13 which is far from the diffraction limit > 0.85. Off-axis the peak is not observable anymore due to occuring aberrations.

out. Due to the wall thickness of 0.35 mm, a single arm which is 1 mm broad can be bend even by applying a fraction of a Newton such that the total radial pressure on the lens stays constant in the cool-down process. For the

Table 5: Thermal shrinking of the materials used in this work from 300 K to a given temperature.

Material	$\Delta L/L$ at 4 K (%)	$\Delta L/L$ at 77 K (%)
Aluminium	0.415	0.393
Stainless steel	0.296	0.281
Copper	0.324	0.298
PTFE (Teflon^{TM})	2.14	1.941
Fused Silica	–0.008	–0.002
Calcium Fluorite	–	0.284

2″ lenses the axial positions are defined by separation rings placed between each lens. Since the manufacturing tolerances of the distance rings were larger than the scaling, it was decided to neglect a rescaling of the lengths. The separation rings are shown in orange in Figures [10,32]. Due to the curvature of the UVFS meniscus lens with surface numbers 13 and 14, a second mounting ring pushes it down to prevent a vertical displacement. The whole stack of rings for the 2″ system is pushed down by three thrust pieces screwed in a ring which also supports the 1″ meniscus lens with three arms as shown in Figure 15. The final ring as well as the supporting cage which centers all rings

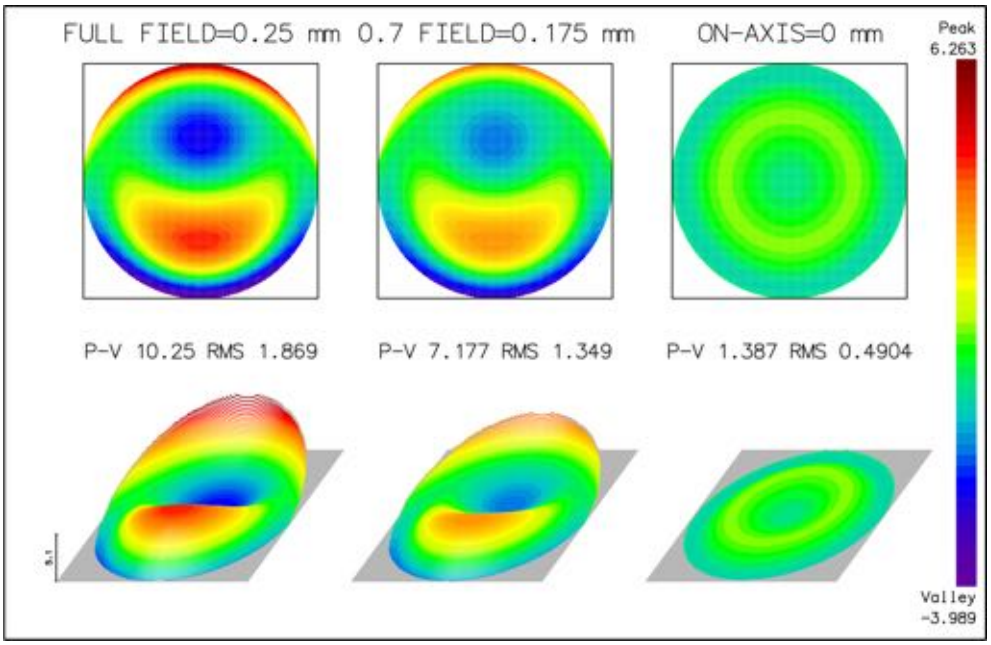

Figure 13: Full field analysis of the wavefront. While photons irradiated from the center of the object experience only comparably small spherical aberrations, the off-center wavefronts are distorted by coma and a tilt in y-direction. This may be caused by the Edmund asphere, since it is designed for collimation. In Section 4.1, which outlines proposals for future updates, the first asphere was modified to counteract on these aberrations.

and the mount on the resonator contain a 3 mm slit such that the radial compression pressure again is minimized. Since the cage is slit over a distance of 73 mm, two clamps are mounted to stabilize the stack.To evacuate the whole stack properly each ring is kitted with cuts and holes as shown in Figures [10- 15]. Blackbody radiation not only heats up the trapped ions and causes systematics in high-precision spectroscopy, but also increases the thermal energy which is absorbed by the material within the 4 K-stage and needs to be dissipated through the cryogenic setup. In the worst case, the energy input increases so far, that the superconducting resonator can't be operated without quenching. A quench would increase the electrical resistance, which nearly vanishes in the superconducting state and the stored power dissipates instantaneously as heat. to prevent this, a 2 mm wide pinhole shown in Figure 16 was placed in the intermediate focus on the 40 K-stage. On top of the focus the PTB asphere is located. Surrounding both systems, the lens stack as well as the last lens, two aluminum heat shields are mounted with holes just as wide as the calculated beam diameters. To thermalize the lens tower on top of the resonator, multiple copper braids air pinched against the aluminum cage and more important the mounting ring at the resonator.

3.6 OPTOMECHANICAL STRESS TESTS

Before the lens stack was mounted on top of the resonator, cool down tests had been successfully carried out to prove that the system stays intact while

Figure 14: Illustration of a ring holder for a 2″ lens. The ring is partially segmented into 40 flexible arms with 1 mm separation. The inner diameter measures 50.5 mm and is therefore undersized to clamp and center the lenses. The wall thickness of the arms is 0.35 mm. Each ring is anodized to reduce stray light reflections.

cooling down. If the Edmund asphere would have been damaged by the radial pressure of the shrinking surrounds, glass pieces could have fallen into the resonator and as a result the quality factor of the resonance would have been decreased. Therefore it was first thermalized on a copper plate which was then directly mounted on the crold-head of the cryogenic storage ring test-bench at MPIK. Due to the small volume a cool-down cycle from 300 K down to 4 K took about 1 d, which is a fraction of the usual cycle at CryPTEx II (≈ 7 d).

3.7 FIRST CHARACTERIZATIONS OF THE IMAGING SYSTEM

A critical part in this system was the alignment of the stack and confirmation of the resolution power which was also simulated within the OSLO environment. Since the inter-ionic distance in a two-ion crystal measures about 27.8 µm [39] pinholes with diameters from 20 µm to 5 µm were utilized as target. Due to the 13 µm pixel size of the Andor EMCCD, a standard web cam complementary metal-oxide-semiconductor (CMOS) chip with 3 µm pixel size was employed as detector. The targets were illuminated utilizing the 313 nm cooling laser. To avoid damages due to the high power, the intensity was reduced with a $\lambda/2$-plate and a Glan-Taylor polarizer. Since the lens stack needed to be completely illuminated, a concave 0.5″ lens with $f = 30$ mm widened up the beam which was then collimated and refocused onto the pinhole by two 2″ concave lenses with $f = 100$ mm and $f = 75$ mm, respectively. The pinhole was mounted on a x-y manipulator such that it could be moved and aligned with respect to the focus. In addition, the lens stack as well as the CMOS were mounted on a x-y-z manipulator.

Figure 15: Illustration of the final ring (dark grey) on top of the lens stack. The anodized ring is fixed by eight M3 screws to the aluminum cage and cut by a 3 mm slit. Three arms are setting and centering the 1″ meniscus lens. The mounting rings of the other lenses are pushed down by three M4 thrust pieces which are screwed into the arms.

3.7.1 First images with the lens stack

The resolution power of the lens stack can be directly estimated within OSLO as shown in Figure 17. With the setup described in the last section pinholes with three different sizes (5 µm, 10 µm, 20 µm) have been observed. In Figure 18 the mean of 200 images of each pinhole is shown. One can observe that the 20 µm pinhole was not equally illuminated. This can be explained in many different ways. First of all are the lasers located in the lab a level below and directly shot through the ceiling onto the breadboards which led not only to a spot size of roughly 10 mm but also increased positioning instabilities. This lead to a continuous variation of the beam location. In addition the floor of the lab is rather unstable such that movements inside and outside the lab caused vibrations and a relative movement of the beam energy. Therefore, it was temping to actively stabilize the beam with a point stabilization. However, due to the low beam energy this did not work properly since the detector of the beam stabilization could not collect enough photons. Hence, the signal intensity through the collimator was continuously varied such that a reproducible measurement of e.g. the depth of focus or a quantification of aberrations and the imaging quality was not possible.

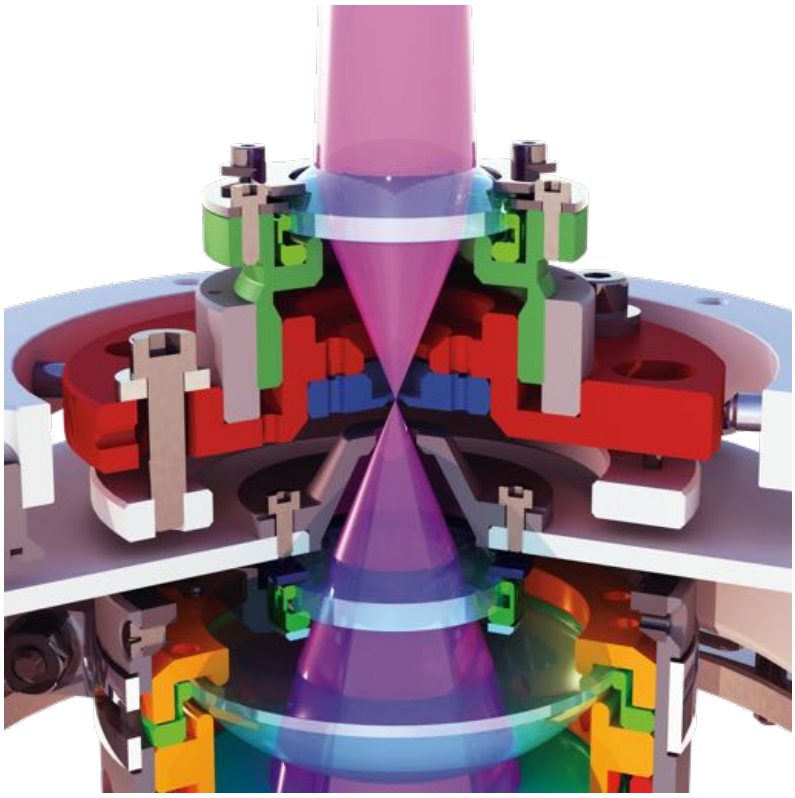

Figure 16: Illustration of the intermediate focus. In the bottom picture, both meniscus lenses are shown. An aluminum shield which is mounted on the 4 K-shield. Additionally, an anodized aluminum hat with a 4 mm hole is mounted with three screws on top of the shield to reduce reflections of stray light. In blue, a 2 mm pinhole is mounted on a movable ring holder shown in red. Both pieces are made of anodized aluminum. The ring holder is fixed by three screws in axial direction on the 40 K heat shield. In addition to the diaphragm a stainless steel threaded bush (gray) is fixated on the ring. Thus, the holder for the bi-asphere colored in dark green can be screwed in and out by 2.5 mm in each direction.

3.7.2 Characterization of the magnification

Due to the flexible design of the setup it is possible to change the distance of the second asphere mounted on top of the 40 K stage by $\Delta z = \pm 2.5\,\mathrm{mm}$. Therefore, one can adjust the back-focus length and the magnification of the system. The cooling laser was again used as light source. This time the power had been reduced with the Glen-Taylor and the $\lambda/2$-plate to a few micro-Watt to avoid damages of the target and the EMCCD. A UVFS diffuser had been mounted right infront of a negative NBS 1963A resolution-test target of the company Thorlabs. Since the diffuser spread the laser light not evenly, it was constantly rotated. Due to the properties of the target a minimum resolution of 18 cycles/mm could be tested. This is twice the separation of a two-ion beryllium crystal trapped, with axial frequency $\omega_z/2\pi = 1.2\,\mathrm{MHz}$ calculated in Section 3.7.3, namely 56 µm. The target was placed in focus in front of the lens stack, which was mounted together with the bi-asphere on a x-y manipulator. Another linear stage provided the manipulation of the asphere in z-direction. After alignment, the position of the asphere was shifted along the optical axis

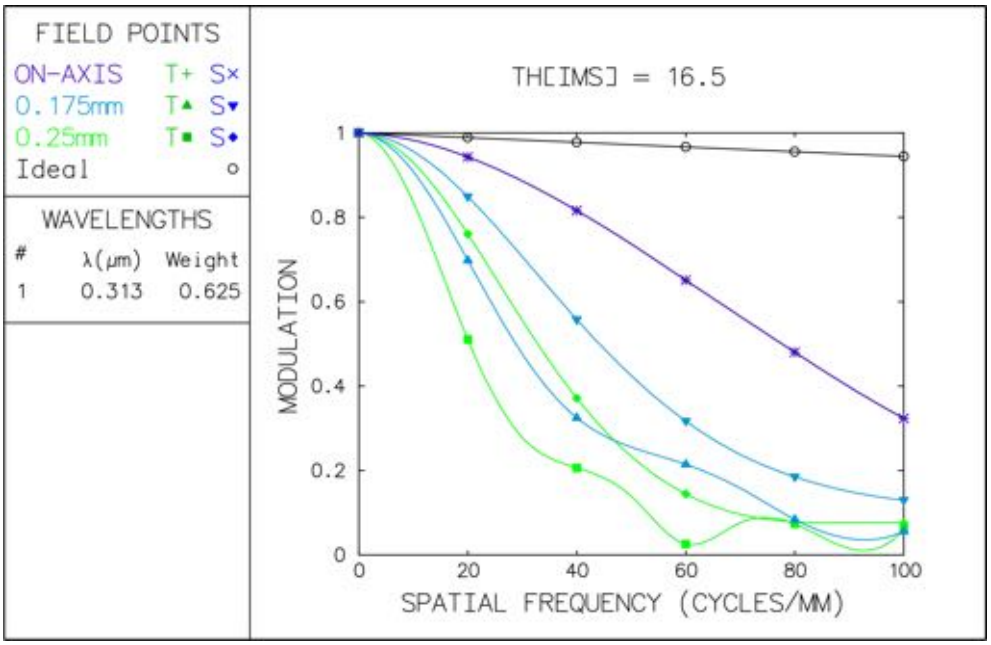

Figure 17: Simulation of the modular transfer function in OSLO. While the performance of the lens stack is far from the diffraction limit, on axis points are still resolved far above 100 cycles/mm. At the edge of a crystal with 250 μm radius the tangential MTF falls below 0.2 at 40 cycles/mm, which corresponds to a resolution of $d = 25\,\mu\text{m}$.

which resulted in a change of the magnification and a shift of the imaging plane.

3.7.3 Determination of the resolution

By utilizing the resolution test target the edge response of the objective can be estimated. In Figure 20 a simulated image of a grid with a side length of 100 μm is compared with a cutout of the test target with similar scaling. While the spacing inside the simulated grid is 25 μm, the lines of the projected eight are separated by 28 μm. Both images show a comparable behavior, however, a quantification of the resolution is only possible by analyzing the edges. Unfortunately OSLO did not provide distribution densities for the simulation, such that only the images which were taken by the EMCCD could be analyzed.

Since the maximum spatial frequency on the NBS 1963A target was only 18 cycles/mm, a resolution limit was achieved by extracting the intensity gradients of the horizontal lines. A simple edge detection algorithm determined the area containing the steepest slope. Here, the intensity signal I was first convolved with a Gaussian kernel of length five containing a width of $\sigma = 1.0\text{px}$

$$G = \begin{bmatrix} 0.169 & 0.215 & 0.232 & 0.215 & 0.169 \end{bmatrix} .$$

In addition a derivative kernel

$$D = \begin{bmatrix} 1 & 0 & -1 \end{bmatrix}$$

was deployed on the noise filtered signal resulting in $p_u = D * (G * I)$. The local maxima of $|p_u|$ represent now the steepest slope on each edge. In the $1/e$

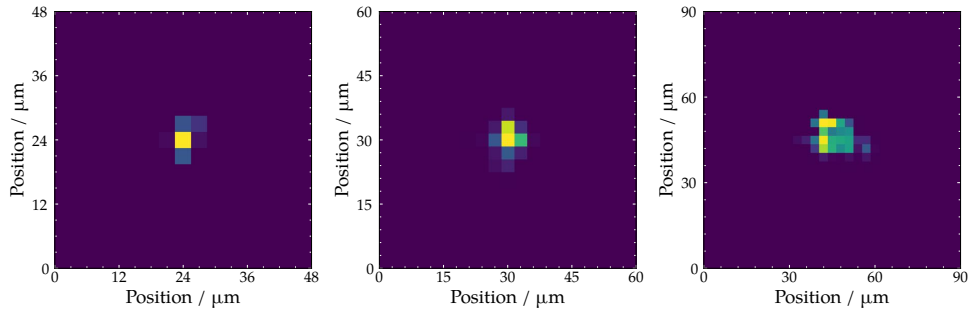

Figure 18: Images of a 5, 10, 20µm pinhole, taken by a CMOS with 3 µm pixel size in the intermediate focus behind the lens stack. While images (a) and (b) show the expected results and yield the pinhole sizes, (c) is distorted and asymmetrically projected on the CMOS. This is a result of the unstable ground which deforms already by moving through the laboratory.

neighborhood of each local maximum it was assumed that the slope in I is nearly linear. Thus, in this area linear fits of type $f(x) = ax + b$ were employed on the signal I as shown in Figure 21. A quantification of the resolution is then given by $d = (I_{90-10}/a) \cdot (px/M)$, with I_{90-10} corresponding to the intensity difference of the linear region. The averaged resolution is $< d >= 7.09(1.16)$ µm over the whole cycle of horizontal lines.

3.8 LENS ALIGNMENT ON THE SUPERCONDUCTING RESONATOR

With the magnification-to-distance relation the objective could be mounted inside the vacuum chamber. Since no guiding wire probe was available at that moment it was decided to align the lens stack with respect to the electrodes and the grid of the niobium flange. By adding copper braids between the tower and the shields, a distance of 2 mm between the gold plated 4 K cover and the lens cover could have caused electrical shorts. To prevent this Kapton stripes are covering the shield from a direct contact with the braids. Since the diaphragm and the bi-asphere are self-centering, the whole mount on the 40 K stage carefully adjusted with the asphere screwed completely inside the winding to image the illumination of the pinhole. If the light cone is well centered ,a fine adjustment was applied with the asphere's focus further away from the diaphragm until the pinhole cut-off was radially symmetrical relative to the niobium flange. Lastly, the distance of the bi-spheric lens to the resonator was optimized to reach a magnification of $M \approx 12.7$. Due to thermal contraction of the copper shields and the resonator itself during cooldown from 300 K to 4 K and 40 K respectively, an offset of +0.16 mm for the position of the asphere was determined and had been considered.

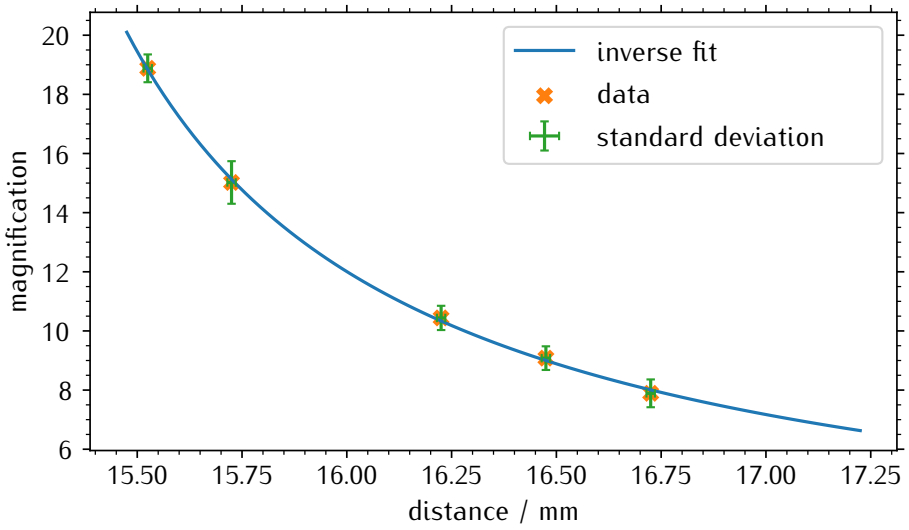

(a)

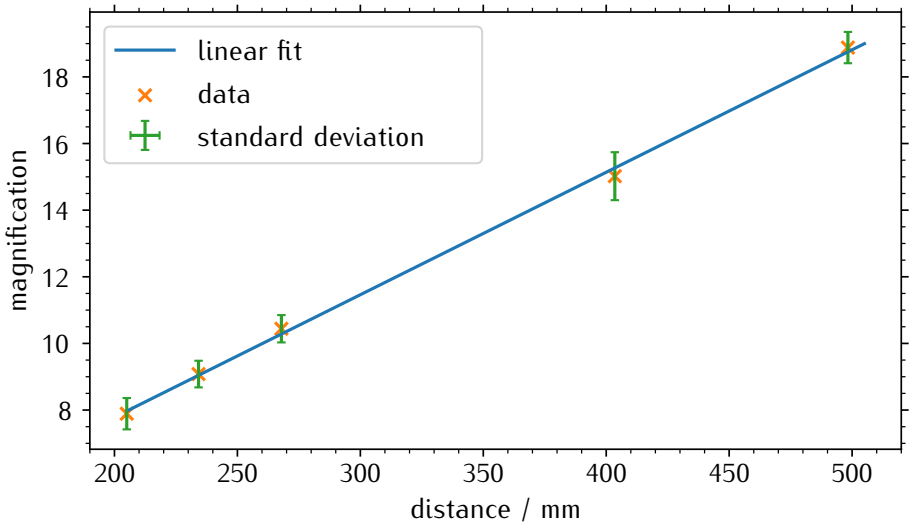

(b)

Figure 19: (a)Characterization the magnification in dependence of the lens distance to the intermediate focus by moving the bi-aspheric lens along the optical axis. An inverse function $f(x) = a/(b-x)$ had been fitted on the data points. (b) Magnification in dependence of the distance from the bi-asphere to the EMCCD.

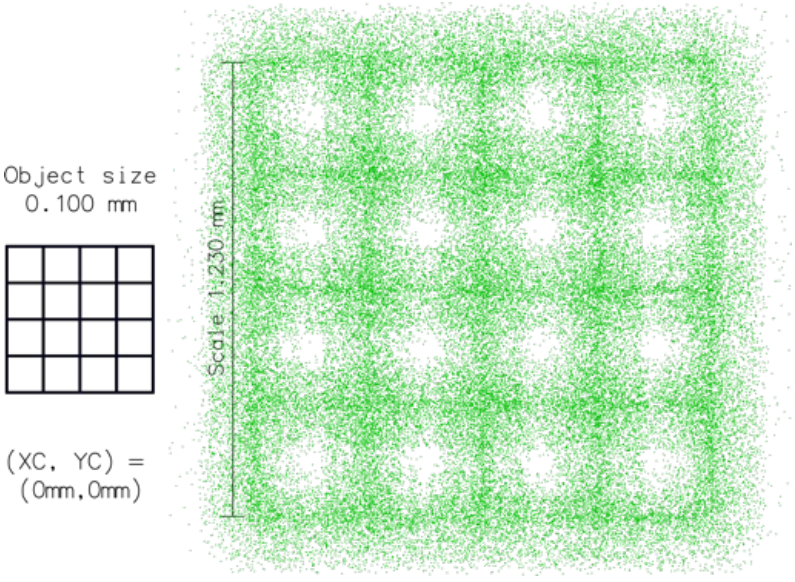

(a)

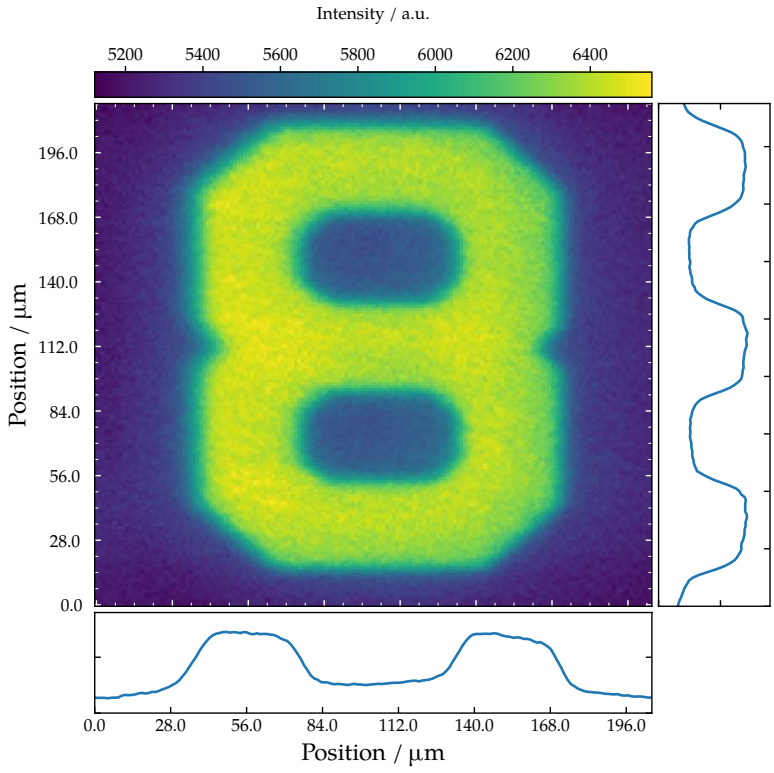

(b)

Figure 20: Comparison between a simulated and a real image with comparable scalings. (a) Ray tracing simulation of a grid with 100 µm side-length. (b) Cutout of a resolution target image at magnification $M = 10.47$. On the right plot the mean marginal intensity along the y-axis for the x-axis region 93.4 – 118.3 µm is shown. This corresponds to 20 px. On the bottom, the same was done for the x-axis from 89.7.4 – 151.9 µm which correspond to 20 px on the EMCCD.

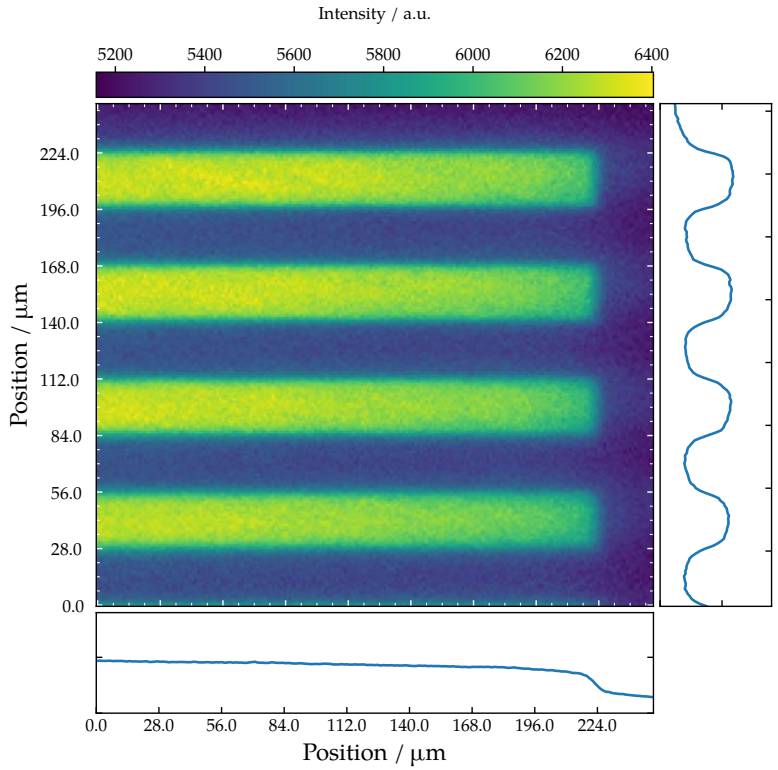

(a)

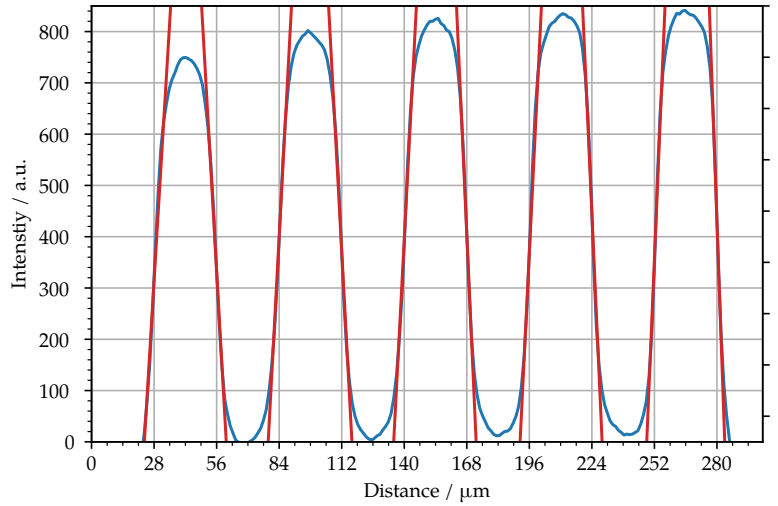

Figure 21: Cutout of a resolution target image at magnification $M = 10.47$. On the right plot the mean marginal intensity along the y-axis for the x-axis region 186.8 – 199.2µm is shown. This corresponds to 10px. On the bottom, the same was done for the x-axis from 62.3 – 80.9µm, which correspond to 50px on the EMCCD. (b) Linear fits $f(x) = ax + b$ (red) on the averaged signal (blue) of the projected signal the horizontal lines. The resolution value determined from the slope and the 10-to-90% intensity is given by $d = (I_{90-10}/a) \cdot (px/M)$. Within this area a mean value of $< d >= 7.09(1.16)$µm was determined.

4 UPGRADES

Throughout the last chapter it was shown that the system built and assembled in this work reaches the requirements listed in Section 3.4. However, upgrades may become necessary to be able to decrease integration times of the EMCCD and resolve ion dynamics within large crystals [32]. For example, the inter-ionic distance in a linear chain of $N = 50$ beryllium ions is about 4.8 µm for an axial trap frequency of 1.2 MHz assuming the scaling introduced in Section 3.7.3. The improvements can be achieved by increasing the Strehl ratio and reducing the number of optical elements to increase the photon transmittance. Furthermore a reflective optical system could become usable for direct fluorescence detection of a highly charged ion or another singly charged ion species inside the trap if it features a transition with scattering rate in the range of 10 kHz. This could also enable sufficient pixel-binning to probe quantum logic schemes and detect motional states directly on the EMCCD or select single ions on a multi pixel PMT. In this chapter, three different optical systems which were simulated in OSLO are presented.

4.1 MODIFICATION OF THE FIRST ASPHERE

To maintain the ability of an efficient fluorescence collection for the whole wavelength range from 235 nm to 441 nm the lens stack needs to stay in place. With the first asphere a lens was placed into the system which was not designed for a working distance of 57 mm at a wavelength of 313 nm. In addition, these kind of aspheric lenses are usually optimized to focus a collimated beam to a fixed distance but not vice versa. Therefore, the curvature of the Edmund asphere has been modified in OSLO to decrease aberrations and increase the Strehl ratio for photons with 313 nm wavelength. The new coefficients are shown in Table 6. In Figure 33 the PSF for three points in the object plane (on-axis,125 µm off-axis, 250 µm off-axis) is shown. Compared to the currently used asphere, the Strehl-ratio is increased by a factor of 20 to $I/I_0 = 0.378$ for the final PSF with the 40 K.

Table 6: Coefficients for the modified asphere which has a radius $r = 25$ mm and an numerical aperture of $NA = 0.4$. The distance to the trap center is 65 mm.

Surface	κ	α_4	α_6	α_8	α_{10}
1	–1.1080	$-3.2215 \cdot 10^{-6}$	$-6.1063 \cdot 10^{-10}$	$-1.8183 \cdot 10^{-14}$	$-2.00 \cdot 10^{-16}$

In addition, it was possible to decrease the peak-to-valley ratio of the wavefront by a factor of two, which indicates a tremendous reduction of the aberrations. In Figure 34 the simulated wavefront is shown. The lateral magnification increased slightly to $M = 13.7$, which indicates a small shift of the intermedi-

ate focus. Therefore, simulations show that the pinhole needs to be readjusted and moved 0.5 mm away from the tap center, to maintain an effective transmission of the other wavelengths. Additionally, only the spacer between the modified asphere and the convex lens needs to be changed. Thus it is probably the simplest upgrade for the current optical system and will allow to resolve sub 5 µm ion separations as shown in Figure 36.

4.2 REPLACEMENT OF THE LENS STACK WITH A BI-ASPHERIC LENS

Within the theory section 3.1 it was stated, that a single asphere is not only able to replace multiple lenses, but also reduce aberrations. In this section all lenses on the 4 K stage were replaced by a single bi-asphere which reduces most monochromatic aberrations and pushes the performance of the objective into the refraction limited regime. However the chromatic correction is lost, such that the 235 nm and 441 nm are not refocused on the slit between the two cryogenic shields. Thus, an effective photon collection at these wavelengths is no longer possible. The first surface of the collecting asphere is 65 mm away from the trap center and the lens diameter increased to 55 mm to keep the numerical aperture above 0.3 at $NA = 0.325$. An overview of the bi-aspheric lens parameters is given in Table 7. The lens was optimized to become near diffraction-limited over the full size of a 500 µm × 500 µm coulomb crystal. The Rayleigh limit of a $NA = 0.325$ lens at 313 nm is $d = 0.59$ µm. Therefore in the image plane the first minimum of the Airy function is only 13.5 µm away from the peak as shown in Figure 23 assuming the simulated magnification of $M = 23.1$. Hence it can't be resolved due to the 13 µm pixel size of the EMCCD and is reduced to $d_{\mathrm{EMCCD}} = 2px/M = 1.13$ µm. This is still sufficient, even for large crystals or trapping frequencies exceeding the 1.2 MHz. Since the PTB bi-asphere is still movable along the optical axis it is possible to increase the magnification at some point. However, that may cause an increase in aberrations, since the first asphere now optimized and even corrects the errors of the second lens at 40 K to increase the Strehl ratio even on the edges of the crystal. A single bi-asphere on top of the resonator would decrease misalign-

Table 7: First refocussing bi-asphere which has a radius $r = 27.5$ mm and an numerical aperture of $NA = 0.325$. The distance to the trap center is 65 mm.

Surface	κ	α_4	α_6	α_8	α_{10}
1	−2.3119	$-4.9387 \cdot 10^{-7}$	$2.729 \cdot 10^{-10}$	–	$-3.8076 \cdot 10^{-16}$
2	−2.1143	$-5.6097 \cdot 10^{-7}$	$3.1955 \cdot 10^{-10}$	–	$-3.9369 \cdot 10^{-16}$

ment errors due to tolerances or manual adjustment. In addition, less straylight is guided into the system due to the reduced number of surfaces. For a setup which does not rely on the fluorescence collection of the spectroscopy ion for example motional state detection can be implemented utilizing a Raman laser system as presented in [29]. Here, the modified objective would fit better since the nearly diffraction-limited properties are beneficial to filter out

noise signals right in front of the PMT without loosing photons of the 313 nm transition. Furthermore, the depth-of-field is conserved.

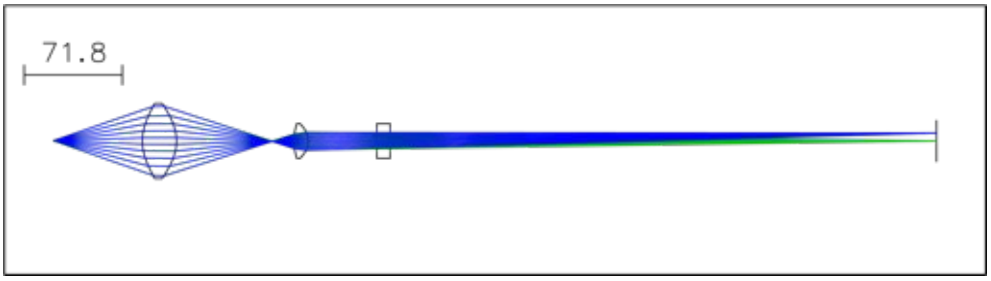

Figure 22: Drawing of the optical elements with a bi-asphere mounted at 4 K, replacing the lens stack. In Section 4.2 the design developed in OSLO is discussed. At a distance of 65 mm from the object plane to the first surface the lens is located. The intermediate focus and PTB bi-asphere are both still located at 157 mm and 176 mm distance from the object. The magnification has been increased to $M = 23.1$ at the image plane located 646 mm away from the object.

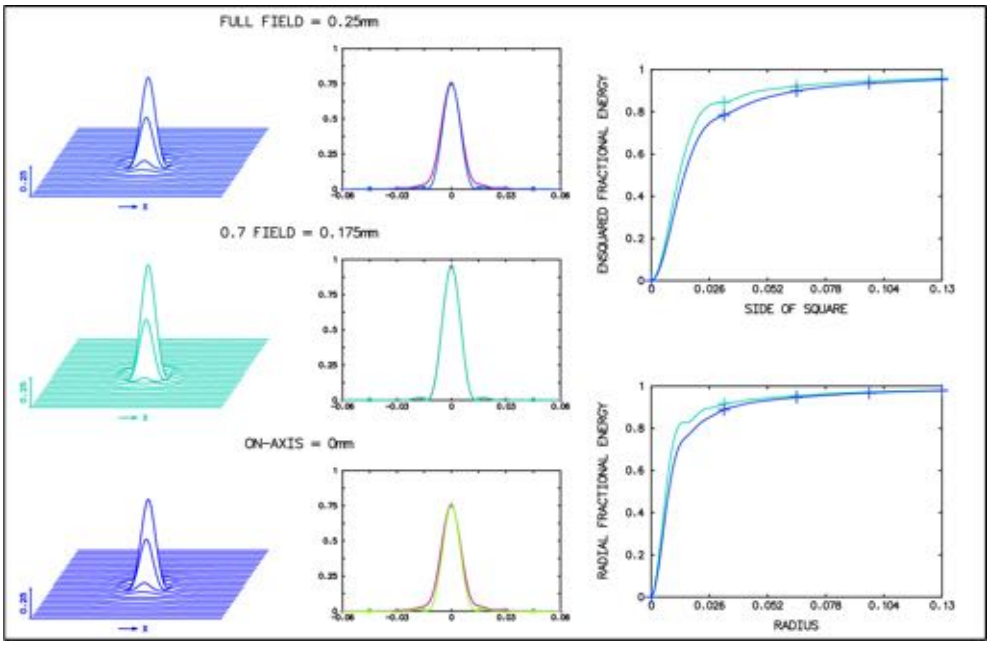

Figure 23: PSF simulation of a $NA = 0.325$ optical system with two bi-aspheres and magnification $M = 23.1$. The minimal Strehl ratio in the focus is $I/I_0 \approx 0.75$ at the center and the border of an object with 250 µm radius. On the right side the ensquared fractional energy is plotted. It is shown, that ≈ 90% of the photons are focused onto a $3x3$ pixel array.

4.3 DESIGN OF A REFLECTIVE SCHWARZSCHILD OBJECTIVE

The disadvantage of refractive objectives presented in this work is the chromatic behavior. By replacing a lens system with an reflective mirror system

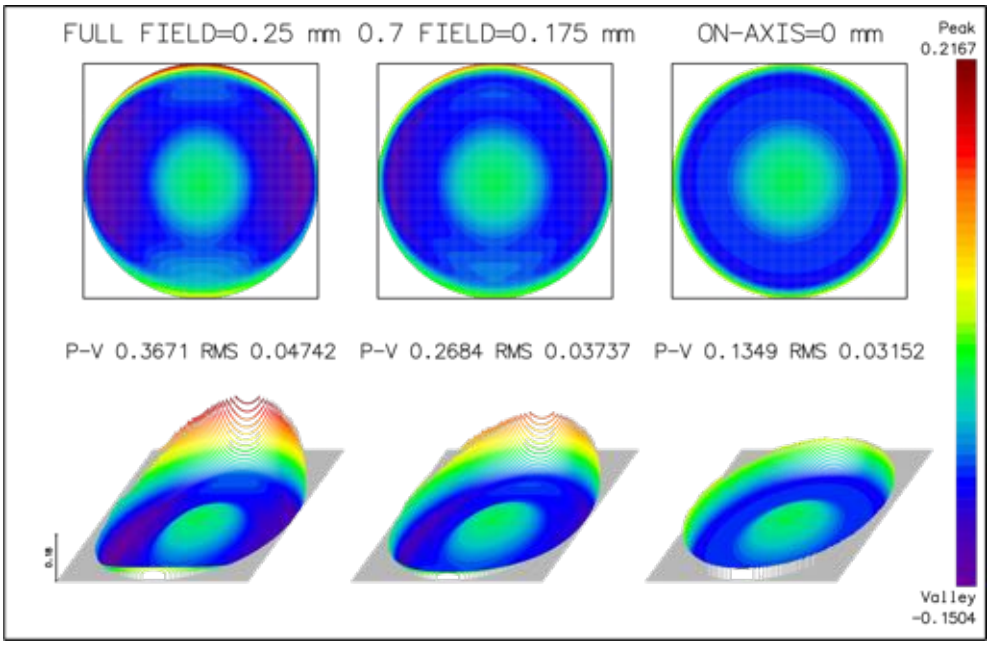

Figure 24: Analysis of the wavefront aberrations for the lens system shown in Section 4.2. The peak-to-valley values as well as the RMS are reduced by an order of magnitude compared to the values in Figure 13. In the Zernike picture presented in Figure 8, a small 3rd order 0° astigmatism contributes mostly to the residual aberrations.

these kind of chromatic aberrations become obsolete. Thus, it is possible to resolve and observe multiple ion species on a single detector. Typical mirror designs are based on a Schwarzschild type objective which is of importance e.g. in EUV lithography [51,54,55].

By neglecting obscuration due to the secondary mirror a numerical aperture of $NA = 0.35$ can be achieved, if a primary mirror with diameter $D = 60\,\text{mm}$ is placed at a distance of $b = 80\,\text{mm}$ to the trap center. This results in an effective focal length of $f = b/\left(\sqrt{5}+2\right) = 18.9\,\text{mm}$. Therefore the secondary mirror would be separated by $d = 2 \cdot f = 37.8\,\text{mm}$ from the primary mirror and would be located inside the resonator. As a result, a system with such a numerical aperture comparable to the previous proposals is not realizable without compromising the quality factor of the trap. However, a feasible distance from the trap center to the primary mirror would be $b = 120\,\text{mm}$ which results in $f = 28.32\,\text{mm}$ and $d = 56.65\,\text{mm}$. For a mirror diameter of $D_1 = 70\,\text{mm}$ and curvature $R_1 = f \cdot \left(\sqrt{5}+1\right) = 91.672\,\text{mm}$ the minimum size of the secondary mirror is $D_2 = D_1/\left(\sqrt{5}+2\right) = 16.52\,\text{mm}$ with curvature $R_2 = f \cdot \left(\sqrt{5}-1\right) = 35.0\,\text{mm}$. These parameters result in a nearly perfectly collimated beam from the secondary mirror to the to a detector outside the vacuum chamber. By modifying the concave curvatures to $R_1' = 91.23\,\text{mm}$ and $R_2' = 35.43\,\text{mm}$ a nearly perfect imaging with magnification $M = 22.5$ of the object plane can be obtained onto a detector about 700 mm away from the trap center. The minimum Strehl number of this system is $I/I_0 > 0.99$ within a 0.5 mm field of view with a maximum wavefront peak-to-valley ratio of 0.1965 and 0.04 root mean squared as shown in Figures 28 and 29. Due to the sec-

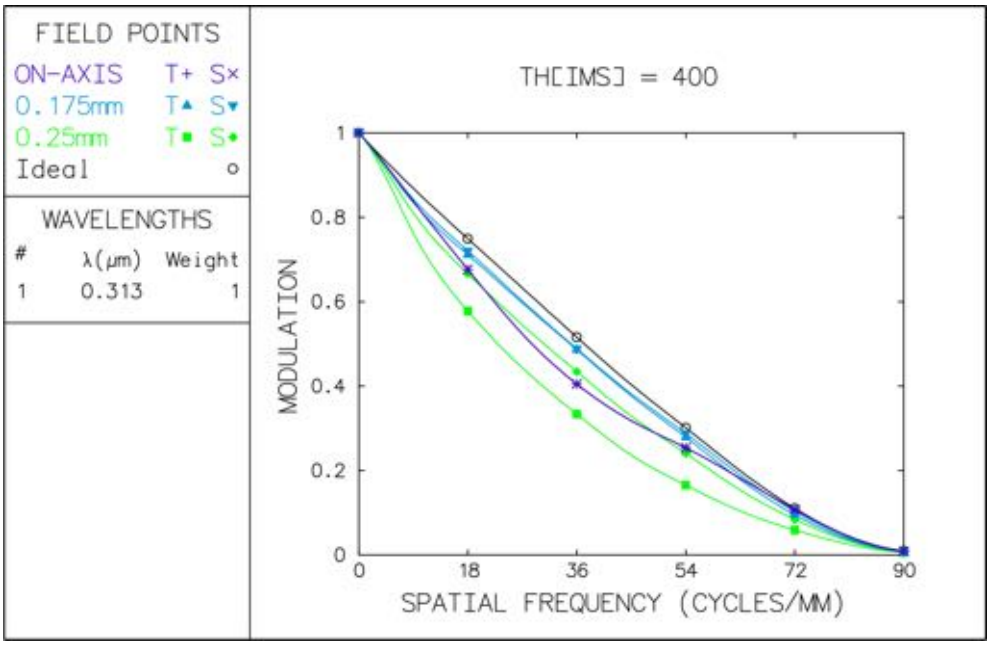

Figure 25: MTF simulation of a $NA = 0.325$ optical system with two bi-aspheres and magnification $M = 23.1$. The Abbe limit for this system is $d = 0.481\,\mu\text{m}$ which corresponds to $M \cdot 90$ cylces/mm. With the design described in Section 4.2 the diffraction limit can be reached over the whole crystal size of $500\,\mu\text{m} \times 500\,\mu\text{m}$ and current limitations are only given by the EMCCD detector.

ondary mirror, parts of the fluorescence are absorbed which reduces the numerical aperture as well as the MTF such that the contrast is reduced and the object smears out. For a standard Schwarzschild objective the obscuration is usually in the range of 20%. Thus variable approaches were made to decrease the obscuration ratio for example by modifying the mirror shape and adding aspheric properties to them [56]. By adding a conic constant to both mirrors it was possible to reduce the diameter of the secondary mirror to 11 mm and the distance to the primary mirror to $d = 55\,\text{mm}$, which reduces the obscuration by 40%. The alignment of the system is shown in Table 8 and plotted in Figure 27. Additionally, the conic constants are given with $\kappa_1 = -7.0894 \cdot 10^{-2}$ and $\kappa_2 = -3.9621 \cdot 10^{-1}$ for the primary and secondary mirror, respectively. Due to these settings the lateral magnification increased to $M = 27.46$. In Figure 30 the simulated MTF is shown. Here, the secondary mirror did not absorb any photons, such that the whole PSF is shown and also the MTF is not deformed. It needs to be considered, that Schwarzschild type optics are sensitive to misalignment. Therefore, the optomechanics are critical for this system, while the substrates and spacers should be ideally made of fused silica due to the extremely low expansion coefficient. In particular a manipulation of the distance to the trap center becomes more critical due to the reduced focus length resulting in a smaller field of depth.

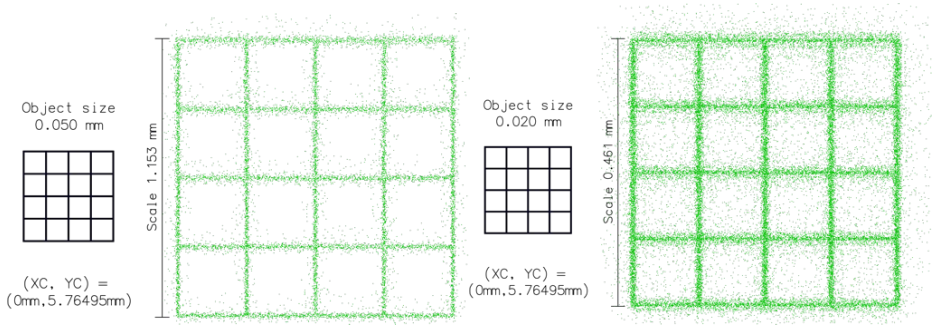

(a) 50 µm grid **(b)** 20 µm grid

Figure 26: Raytracing simulations of the lens system described in Section 4.2 with a grid as object. In the left figure the grid has a side length of 50 µm and in the right 20 µm. It is shown, that a 5 µm line separation is clearly resolvable.

Table 8: Alignment of Schwarzschild objective optimized by OSLO. Surface 1 and 3 are the mirror surfaces while surface 5 is the viewport.

SRF	Radius	Thickness	Aperture radius	Material
Obj	–	120.00	0.25	Vacuum
1	−83.00	–	35.00	refl. hatch
2	–	−55.00	35.00	Vacuum
3	−17.2103	–	5.5	refl. hatch
4	–	175.00	25.40	Vacuum
5	–	9.5	17.5	Silica
IMS	∞	255.00	25.40	CCD

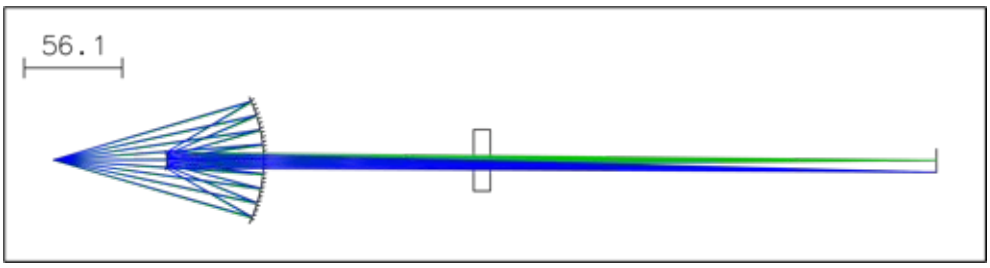

Figure 27: Drawing of the Schwarzschild mirror system, which was designed in this work and is presented in Section 4.3. At a distance of 120 mm from the object plane, the primary, collecting mirror is mounted. Separated by 55 mm to the primary mirror, one finds the secondary mirror with 11 mm diameter. The magnification has been increased by a factor of more than two, to $M = 27.46$, compared to the lens system in Chapter 3. Furthermore a reflective optical system has no chromatic aberrations which allows for a simultaneous fluorescence detection of multiple ion species.

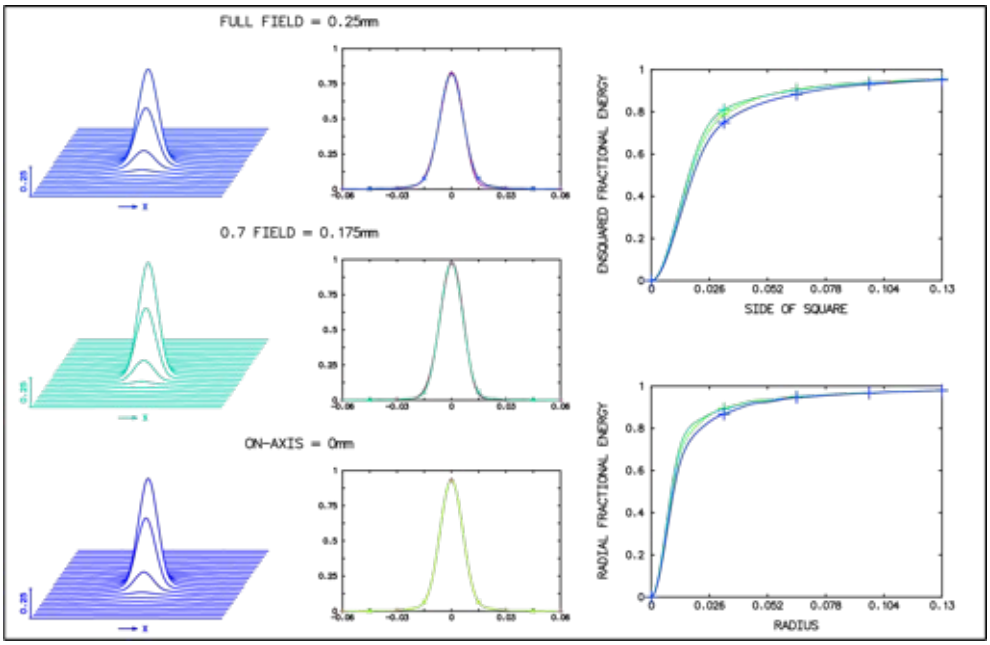

Figure 28: PSF simulation of a $NA = 0.26$ optical system with Schwarzschild mirrors and magnification $M = 27.46$ as described in Section 4.3. The minimal Strehl ratio in the focus is $I/I_0 \approx 0.83$ at the center and the border of an object with 250 µm radius. On the right side the ensquared fractional energy is plotted. It is shown, that ≈ 90% of the energy is focused onto a 3*x*3 pixel array for all three wavelengths. In this simulation the absorption of the secondary mirror is not included. However, only the central part of the wavefront is cut out, such that the Strehl ratio should not change dramatically.

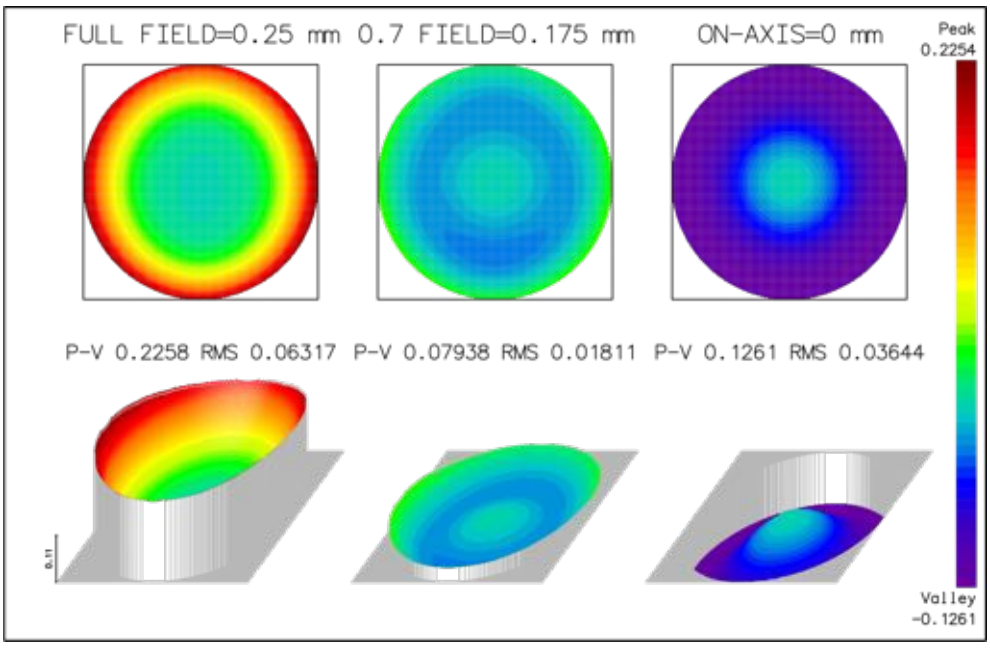

Figure 29: Analysis of the wavefront aberrations for the Schwarzschild mirror system shown in Section 4.3. Compared to the currently installed setup the peak-to-valley values as well as the RMS had been reduced down to 0.2 and 0.06, respectively.

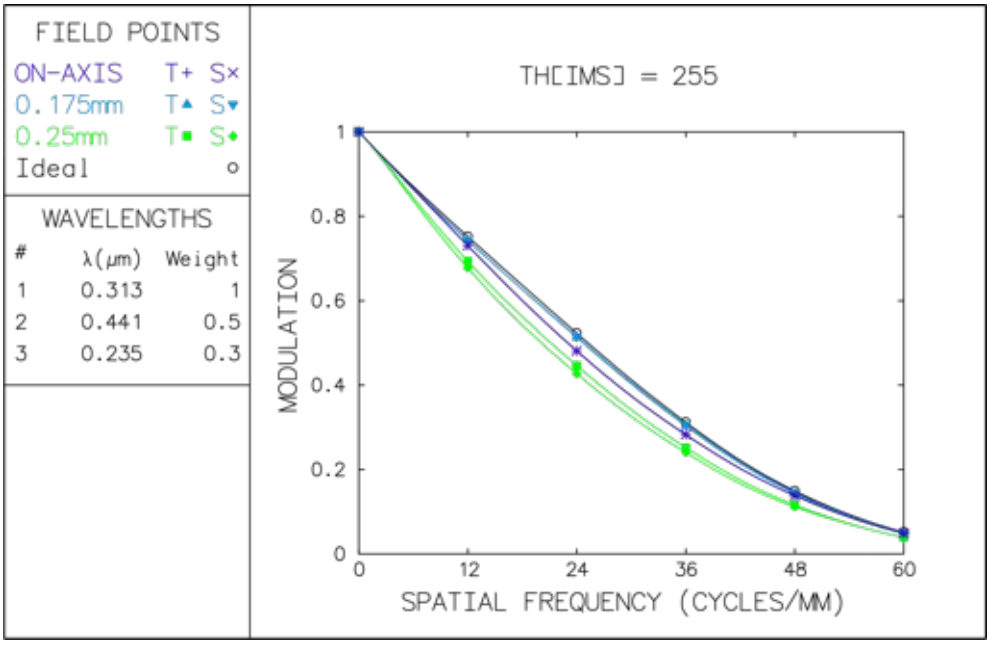

Figure 30: MTF simulation of a $NA = 0.26$ Schwarzschild-like optics and magnification $M = 27.46$. At a wavelength of 313 nm the Abbe limit for this system is $d = 0.6\,\mu m$ which corresponds to $M \cdot 60.5$ cylces/mm. With the design described in Section 4.3 the diffraction limit can be reached over the whole crystal size of $500\,\mu m \times 500\,\mu m$ for all wavelengths and current limitations are only given by the EMCCD detector which can resolve $d_{EMCCD} = 0.947\,\mu m$.

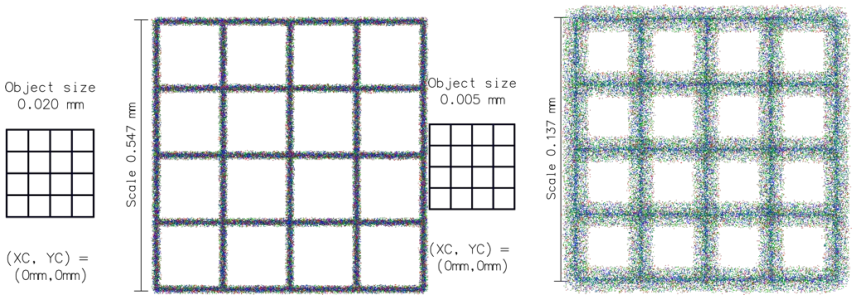

(a) 20 μm grid **(b)** 5 μm grid

Figure 31: Raytracing simulations of the mirror system described in Section 4.3 with a grid as object. In the left figure, the grid has a side length of 20 μm and on the right 5 μm. Green dots are for 313 nm, blue for 441 nm and red for 235 nm wavelength.

5 CONCLUSION AND OUTLOOK

Within this work, an optical system with $NA = 0.365$ consisting of seven commercially available lenses and one special fabricated bi-asphere was developed to image laser-cooled Beryllium ions confined in a quasi-monolithic, superconducting Paul trap resonator at a transition wavelength of 313 nm. Due to the characteristics of the trap, the objective has a working distance of 57 mm and is located inside the vacuum chamber, right on top of the resonator at 4 K. Thus, special lens holders and spacers were designed to be able to keep the lenses intact during cool-down. In addition, the optical setup includes an intermediate focus which allows reducing the exposure of blackbody radiation on the trap and the ions, since a 2 mm pinhole could be installed on the 40 K stage. To keep the ability to detect fluorescence of the resonant two-photon enhanced ionization process and the M1 transition of Ar^{13+} different glass materials were employed in the optical design. This reduced the dispersion of the effective focal length to 2.6 mm and transmit photons in a range from 235 nm to 441 nm through the diaphragm. Different in-air characterizations at room temperature were performed utilizing the 313 nm laser different pinholes with sizes of 5 μm, 10 μm and 20 μm had been illuminated and imaged through the lens stack. Unfortunately, it was not possible to carry out further characterizations of the field of depth or quantifying the imaging quality since the optical setup in front of the lens stack was too sensitive and too unstable due to the floor and the long baseline of the laser. Therefore, the 40 K bi-asphere was installed to try further characterizations on the magnification.

First characterization measurements with a resolution target in air and at room temperature using the 313 nm laser resulted in an averaged resolution of $< d >= 7.09(1.16)\mu m$ at a magnification of $M = 10.47$. While the maximum imaging resolution d of a self illuminating object with wavelength $\lambda = 313$ nm viewed through a spherical objective with numerical aperture $NA = 0.365$, which is given by the Rayleigh-Limit $d = 1.22\lambda/2NA = 0.52\,\mu m$ could not be reached with this system due to a high loss of modulation in the frequency response, residual aberrations caused by the lens system and the need for a intermediate focus to reduce the influence of blackbody radiation on the ions and the cryogenic setup, it is still capable to resolve a two ion crystals with an inter-ionic distance of 27.6 μm which is typical for an axial trapping frequency at $\omega_z/2\pi = 1.2$ MHz. Furthermore, the magnification dependence on the distance to the intermediate focus was measured, which is an important characteristic of the optical system since it is necessary to adjust the vertical position of the bi-asphere when the chamber is warm and vented.

On the optomechanical side, the lens fixtures by now have been tested multiple times during the cool-down and warm-up cycles of the commissioning

phase of the resonator. However, to improve the setup it needs to be considered to reduce the number of degrees of freedom in the relative alignment of the 40 K bi-asphere and the lens stack. In particular, the movement in radial directions needs to be restricted to provide a reliable reproducibility of the optical imaging system. A missalingment of the lenses after maintenance could cost weeks due to the cool-down/ warm-up cycle time of about two to three weeks. Furthermore, the magnification should be ideally being able to be modified while the ion trap is pumped and cooled down to become more flexible since the fluorescence of the M1 transition is collected more efficiently at magnifications from 7.8× to 10×.

To improve the optical properties of the system without completely removing it an optimized asphere that replaces the first 4 K lens was developed. This raises the on-axis Strehl ratio to $I/I_0 = 0.378$ and might increase the resolution below $d = 5\,\mu\text{m}$, which is the inter-ionic distance of the beryllium ions in a large chain of 50 ions at an axial trapping frequency of 1.2 MHz. This study maintains the ability to efficiently collect photons of all previously mentioned wavelengths.

Instead of the lens stack on top of the resonator, a single bi-aspheric lens with $NA = 0.325$ could serve to reach a near-diffraction-limited system with magnification $M = 23.1$ and a minimum Strehl ratio $I/I_0 = 0.75$ over the whole $500\,\mu\text{m} \times 500\,\mu\text{m}$ crystal. With this design, it would be possible to resolve two objects separated by $d = 0.59\,\mu\text{m}$, which would allow for shorter integration times of the EMCCD. Furthermore, due to reduced aberrations, it could reduce the stray-light on flux-sensitive PMT measurements for example in future quantum-logic-scheme based Raman experiments. The downside of this solution is the loss of the other wavelengths since they are not any more focused properly on the intermediate focus. Therefore, direct fluorescence spectroscopy around 441 nm of the HCI is no longer possible.

Finally, a reflective Schwarzschild-type objective with $NA = 0.26$ and Strehl ratio of at least 0.83 in the predefined field-of-view was presented. By removing all refractive elements except for the viewport substrate, chromatic aberrations are canceled and mixed Coulomb crystals consisting of different ion species could be simultaneously detected on a EMCCD. To reduce obscuration by 40%, the secondary mirror diameter was optimized and both mirrors became slightly conic. With such a system the diaphragm needs to be removed to avoid additional refractive elements which cause an increase in the room-temperature blackbody radiation input on the 4 K stage. It was shown in [27] that a tube system can decrease the input of thermal radiation. Therefore this might be considered if such a system could reach the development phase. In addition to the blackbody radiation input, an optomechanical design needs to be developed to challenge the sensitivity to a relative mirror misalignment and the expansion/shrinking due to the temperature of the gradient.

While each of the systems has its up- and downsides it should be considered to maximize the flux on a single pixel to be able to increase contrast and decrease the needed minimal integration times. This can enable the possibility

to temporally resolve dynamics inside the trap environment by locking the EMCCD to the trapping frequencies as already shown in Penning traps [57]. Besides, a mirror system could be used to directly image the HCI fluorescence on the detector if it can be accessed in the optical or UV and provides the cycling frequency high enough.

Currently, the CryPTEx II setup is in the commissioning phase and no ions could be loaded and imaged in the trap due to difficulties with the laser system. If this is resolved, the next steps regarding the imaging system are an estimation of the magnification value for the current configuration with higher accuracy as already shown in [27,58]. Furthermore, a single ion could be loaded and shifted through the trap to estimate the PSF and aberrations of the optics as well as the field of depth.

We have to continually be jumping off cliffs and developing our wings on the way down.

— Kurt Vonnegut [59]

ACKNOWLEDGMENTS

I thank the people, who supported me and pushed me in the right directions to keep me on the track.

Without the outstanding performance of the workshop and the construction, the opto-mechanics would not have been manufactured and assembled in such a short time. Throughout the manufacturing process remaining adjustments were embedded quasi in situ without problems. I'm grateful that we were allowed to test the opto-mechanics at the CSR test-bench. The optical system was designed and optimized with the software OSLO provided by Tanja Mehlstäubler from the PTB. Due to a well established cooperation the bi-aspheric lens was kindly provided by Piet O. Schmidt and his group at the PTB.

A APPENDIX

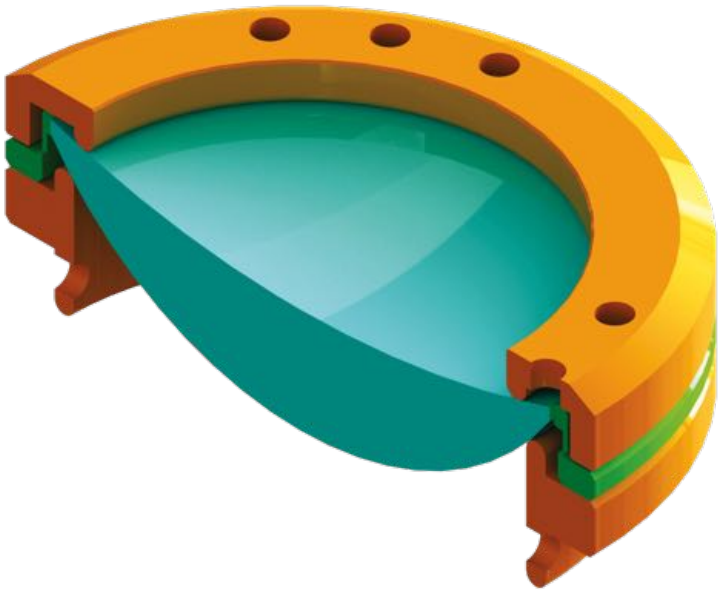

Figure 32: Illustration of the 2″ meniscus mount. On top a ventilated ring pushes the lens uniformly into the radial clamps shown in green. On the bottom it is placed on a distance ring, separating the meniscus from the backside of a concave lens.

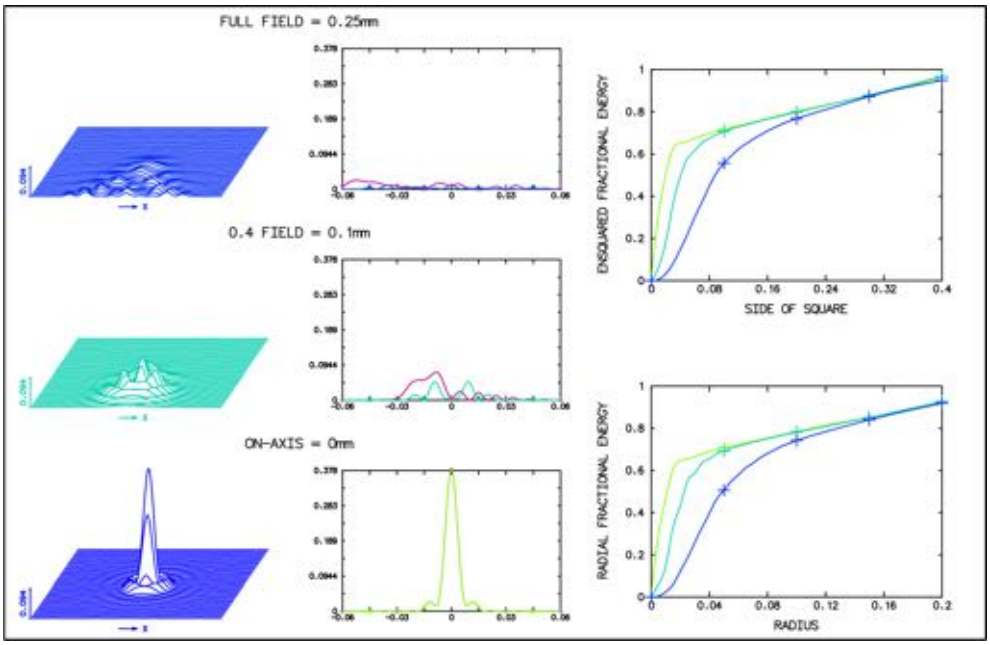

Figure 33: PSF simulation of a optical system with an optimized asphere as collecting lens which is presented in Section 4.1 . The maximum Strehl ratio in the focus is $I/I_{max} \approx 0.375$ at the center. For the outer regions of the target the performance of the system decreases significantly. On the right side the ensquared fractional energy is plotted. It is shown, that ≈ 65% of the energy is focused onto a 3*x*3 pixel array.

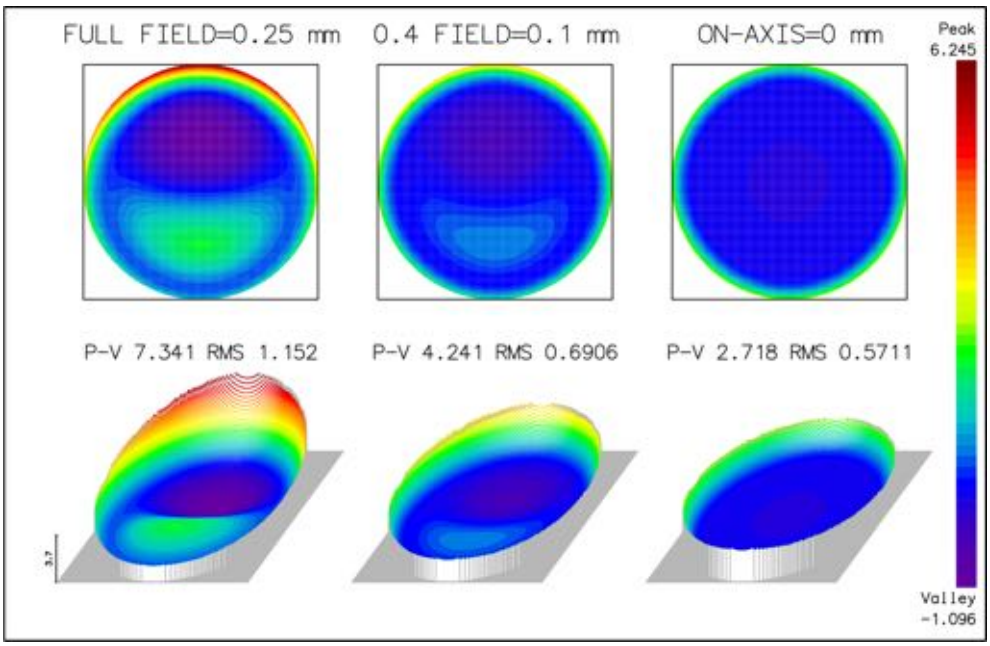

Figure 34: Analysis of the wavefront aberrations for the lens system shown in Section 4.1. Peak-to-valley and root-mean-squared values and were decreased by a factor of at least two compared to the currently mounted system.

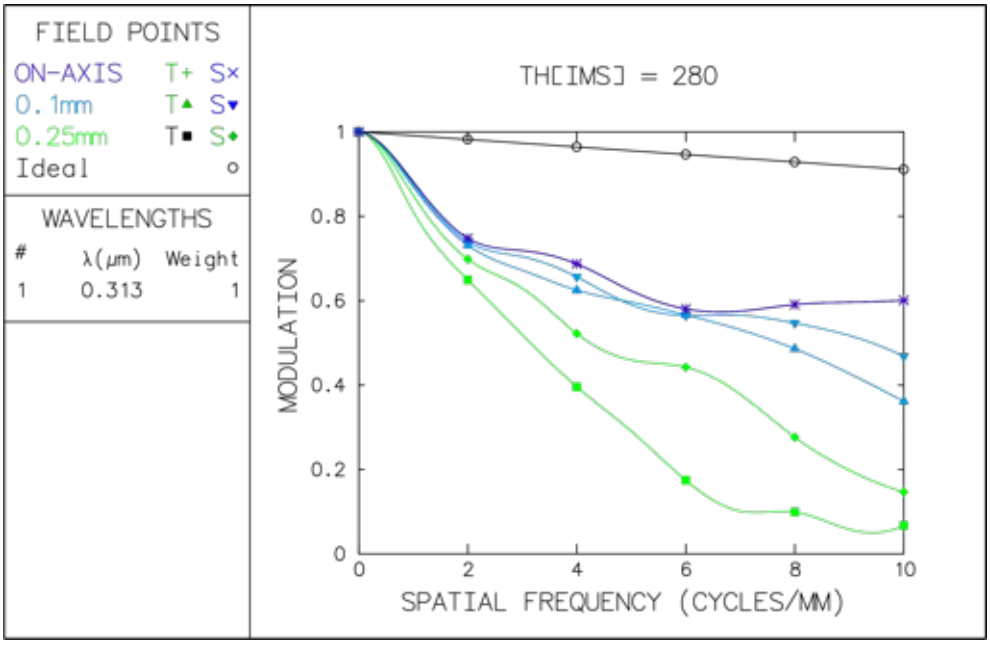

Figure 35: MTF simulation of a $NA = 0.365$ optical system with a modified asphere as collecting lens and magnification $M = 13.7$ as described in Section 4.1.

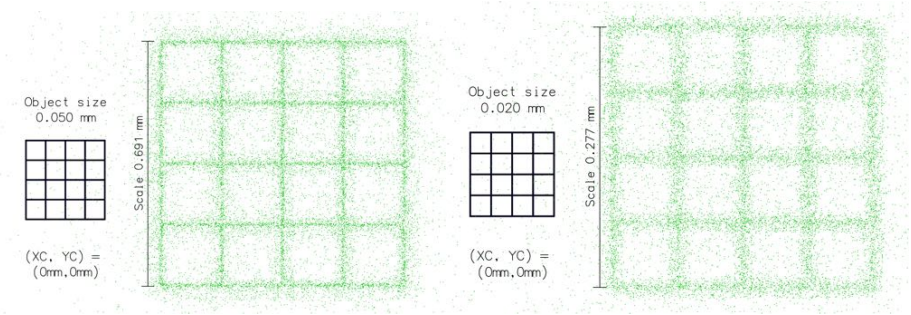

(a) 50 μm sidelength **(b)** 20 μm sidelength

Figure 36: Raytracing simulations of the lens system described in Section 4.1 with a grid as object. On the left figure the grid has a side length of 50 μm and on the right 20 μm. It is shown, that a 5 μm line separation is clearly resolvable.

B | OPTOMECHANICAL DRAWINGS

In this chapter, the drawings of the optomechanical design are attached. These were created by the construction workshop at the MPIK and based on the author's draft including the given requirements, ideas and conceptions.

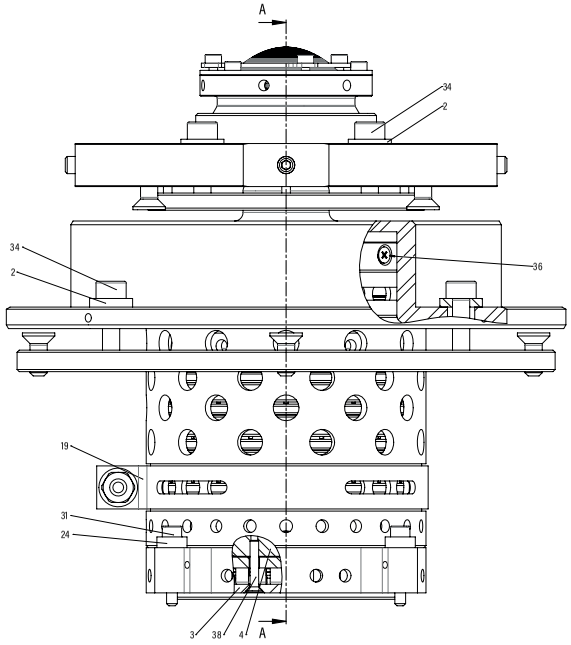

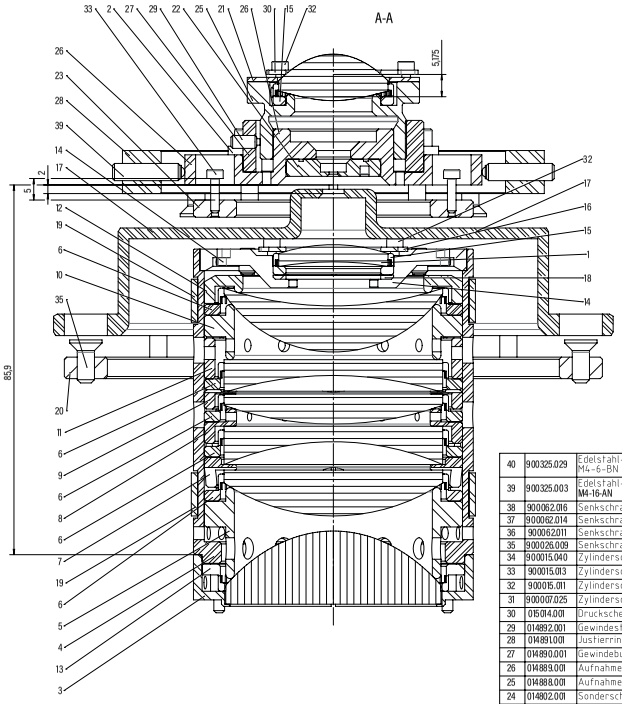

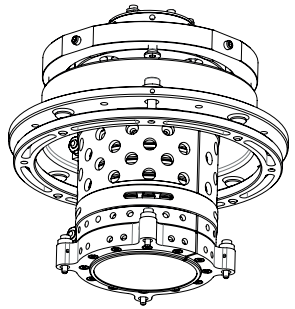

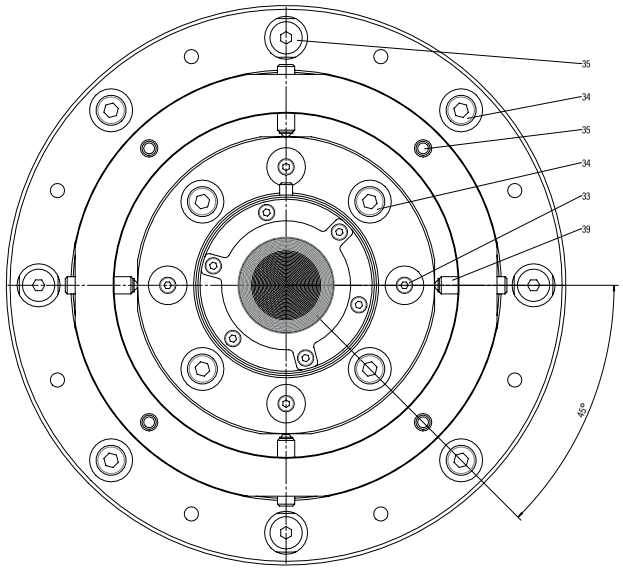

Pos.	Nummer	Benennung	Anz.	Abmessung	Material	Anmerkung	Rev.
40	900325.029	Edelstahl-Kugelspannschraube GN 605 - M4-6-BN	3	M4 × 6	1.4301 (X5CrNi18-10)	Kaufteil	
39	900325.003	Edelstahl-Kugelspannschraube GN 605 - M4-16-AN	4	M4 × 16	1.4301 (X5CrNi18-10)	Kaufteil	
38	900062.016	Senkschraube ISO 7046 – M2 × 12	12	M2 × 12	A4-70, UHV	Normteil	A
37	900062.014	Senkschraube ISO 7046 – M2 × 8	8	M2 × 8	A4-70, UHV	Normteil	A
36	900062.011	Senkschraube ISO 7046 – M2 × 4	10	M2 × 4	A4-70, UHV	Normteil	A
35	900026.009	Senkschraube ISO 10642 – M4 × 10	8	M4 × 10	A4-70, versilbert	Normteil	A
34	900015.040	Zylinderschraube ISO 4762 – M4 × 16	8	M4 × 16	A4-70, UHV	Normteil	A
33	900015.013	Zylinderschraube ISO 4762 – M2 × 8	4	M2 × 8	A4-70, UHV	Normteil	A
32	900015.011	Zylinderschraube ISO 4762 – M2 × 5	12	M2 × 5	A4-70, UHV	Normteil	A
31	900007.025	Zylinderschraube ISO 4762 – M2,5 × 16	4	M2,5 × 16	A4-70, versilbert	Normteil	A
30	015014.001	Druckscheibe 22	1	Ø4,0 – t= 1	EN AW-5083 [AlMg4,5Mn0,7]		A
29	014892.001	Gewindestift M3x6 #GN 913.5-M3-6-KU	1			Fa. GANTER	A
28	014891.001	Justierring 01	1	Ø100 – L= 10	EN AW-5083 [AlMg4,5Mn0,7]		A
27	014890.001	Gewindebuchse M34x0,5	1	Ø42 – L= 12	AISI Type 316L Edelstahl		A
26	014889.001	Aufnahme 23	1	Ø70 – L= 14	EN AW-5083 [AlMg4,5Mn0,7]	schwarz eloxiert	A
25	014888.001	Aufnahme 22	1	Ø40 – L= 18	EN AW-5083 [AlMg4,5Mn0,7]	schwarz eloxiert	A
24	014802.001	Sonderscheibe 02	4	Ø7 – t= 2,5	AISI Type 316L Edelstahl		A
23	014791.001	Montagering 02	1	Ø65 – t= 4	AISI Type 316L Edelstahl		A
22	014790.001	Diaphragm 02	1	Ø22 – L= 4	EN AW-5083 [AlMg4,5Mn0,7]	schwarz eloxiert	A
21	014780.001	Sicherungsscheibe 21	1	Ø4,0 – t= 1	EN AW-5083 [AlMg4,5Mn0,7]	schwarz eloxiert	A
20	014773.001	Monatagering 21	1	Ø125 – t= 5	1.4435 (X2CrNiMo18-14-3)		A
19	014770.001	Schelle 01 Komplett	2				
18	014760.001	Passscheibe 01	1	Ø28 – t= 0,967	EN AW-5083 [AlMg4,5Mn0,7]	schwarz eloxiert	A
17	014759.011	Abdeckung 21	1	Ø130 – L= 34	EN AW-5083 [AlMg4,5Mn0,7]	innen eloxiert, außen blank	A
16	014758.011	Druckscheibe 21	1	Ø38 – t= 1	EN AW-5083 [AlMg4,5Mn0,7]	schwarz eloxiert	A
15	014757.001	Zentrierring 22	2	Ø25 – t= 5	EN AW-5083 [AlMg4,5Mn0,7]	schwarz eloxiert	A
14	014755.011	Abschlussring 01	1	Ø62 – L= 9	EN AW-5083 [AlMg4,5Mn0,7]	schwarz eloxiert	A
13	014754.001	Zentrierring 22	1	Ø61 – L= 6,3	EN AW-5083 [AlMg4,5Mn0,7]	schwarz eloxiert	A
12	014753.001	Abstandsring 26	1	Ø60 – L= 6,5	EN AW-5083 [AlMg4,5Mn0,7]	schwarz eloxiert	A
11	014752.001	Sicherungsring 01	1	Ø60 – L= 9,5	EN AW-5083 [AlMg4,5Mn0,7]	schwarz eloxiert	A
10	014751.001	Abstandsring 25	1	Ø60 – L= 12,83	EN AW-5083 [AlMg4,5Mn0,7]	schwarz eloxiert	A
9	014750.001	Abstandsring 24	1	Ø60 – L= 4,5	EN AW-5083 [AlMg4,5Mn0,7]	schwarz eloxiert	A
8	014749.001	Abstandsring 23	1	Ø60 – L= 8,026	EN AW-5083 [AlMg4,5Mn0,7]	schwarz eloxiert	A
7	014748.001	Abstandsring 22	1	Ø60 – L= 7	EN AW-5083 [AlMg4,5Mn0,7]	schwarz eloxiert	A
6	014747.001	Zentrierring 21	5	Ø60 – L= 6,3	EN AW-5083 [AlMg4,5Mn0,7]	schwarz eloxiert	A
5	014744.001	Abstandsring 21	1	Ø60 – t= 12	EN AW-5083 [AlMg4,5Mn0,7]	schwarz eloxiert	A
4	014740.001	Rohr 20	1	Ø65 – L= 71	EN AW-5083 [AlMg4,5Mn0,7]	innen eloxiert, außen blank	A
3	014739.011	Quadrupol – Linsenklemmung 20	1	65 × 65 × 12	EN AW-5083 [AlMg4,5Mn0,7]	innen eloxiert, außen blank	A
2	014338.001	Sonderscheibe 01	8	Ø10 – t= 2	AISI Type 316L Edelstahl		A
1	014248.001	Linse 02	1		Glas, Schott SF2	beigestellt	A

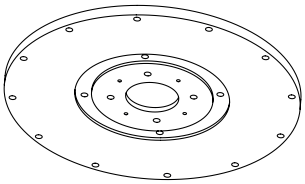

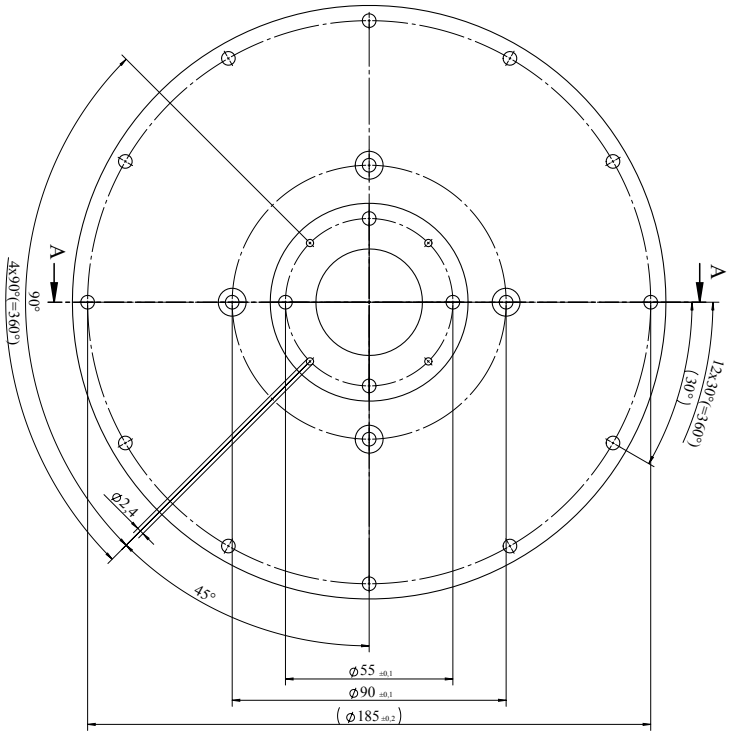
A
A
4x90°(=360°)
90°
12x30°(=360°)
30°
ø2,4
45°
ø55 ±0,1
ø90 ±0,1
(ø185 ±0,2)

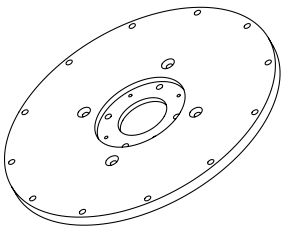

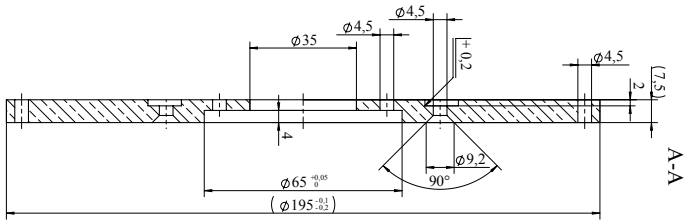
ø4,5
ø4,5
ø4,5
ø35
+0,2
ø4,5
(7,5)
2
4
ø9,2
90°
ø65 +0,05 0
(ø195 -0,1 -0,2)
A-A

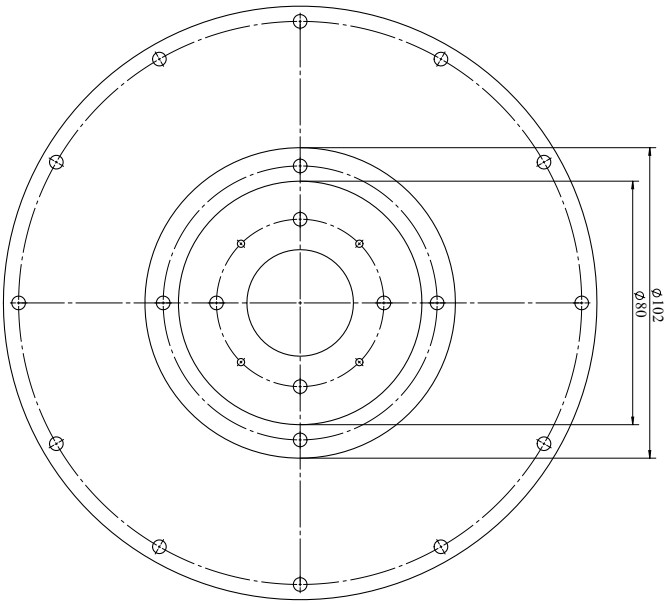
ø102
ø80

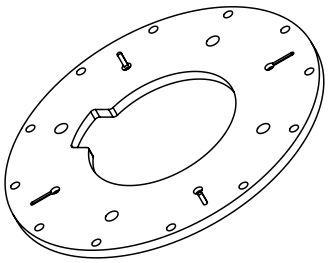

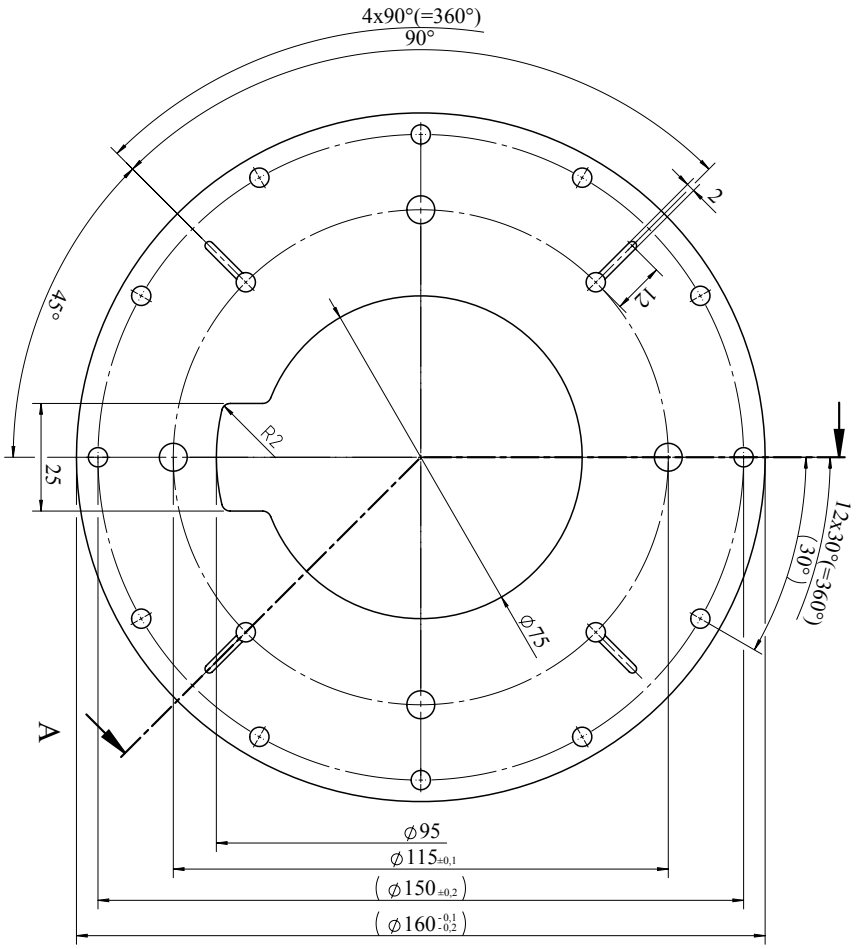
4x90°(=360°)
90°
45°
2
12
R2
25
12x30°(=360°)
30°
ø75
A
ø95
ø115±0,1
(ø150±0,2)
(ø160-0,1-0,2)

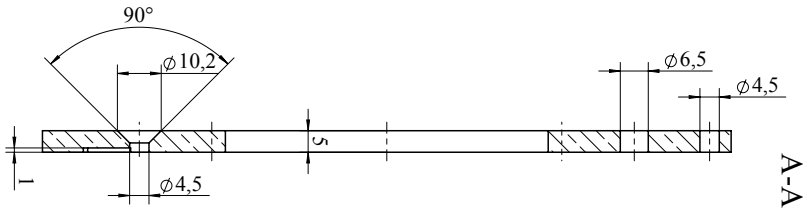
90°
ø10,2
ø6,5
ø4,5
5
1
ø4,5
A-A

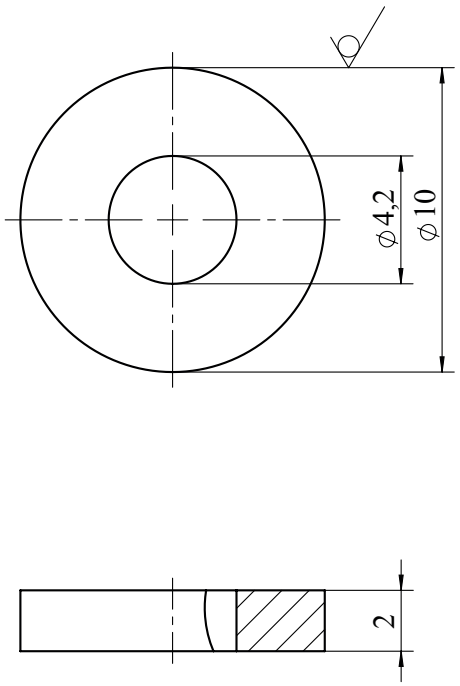

AISI Type 316L Edelstahl

Sonderscheibe 01

237 - CryPTEx 2.0

Komponenten-Nr.: 014338.001

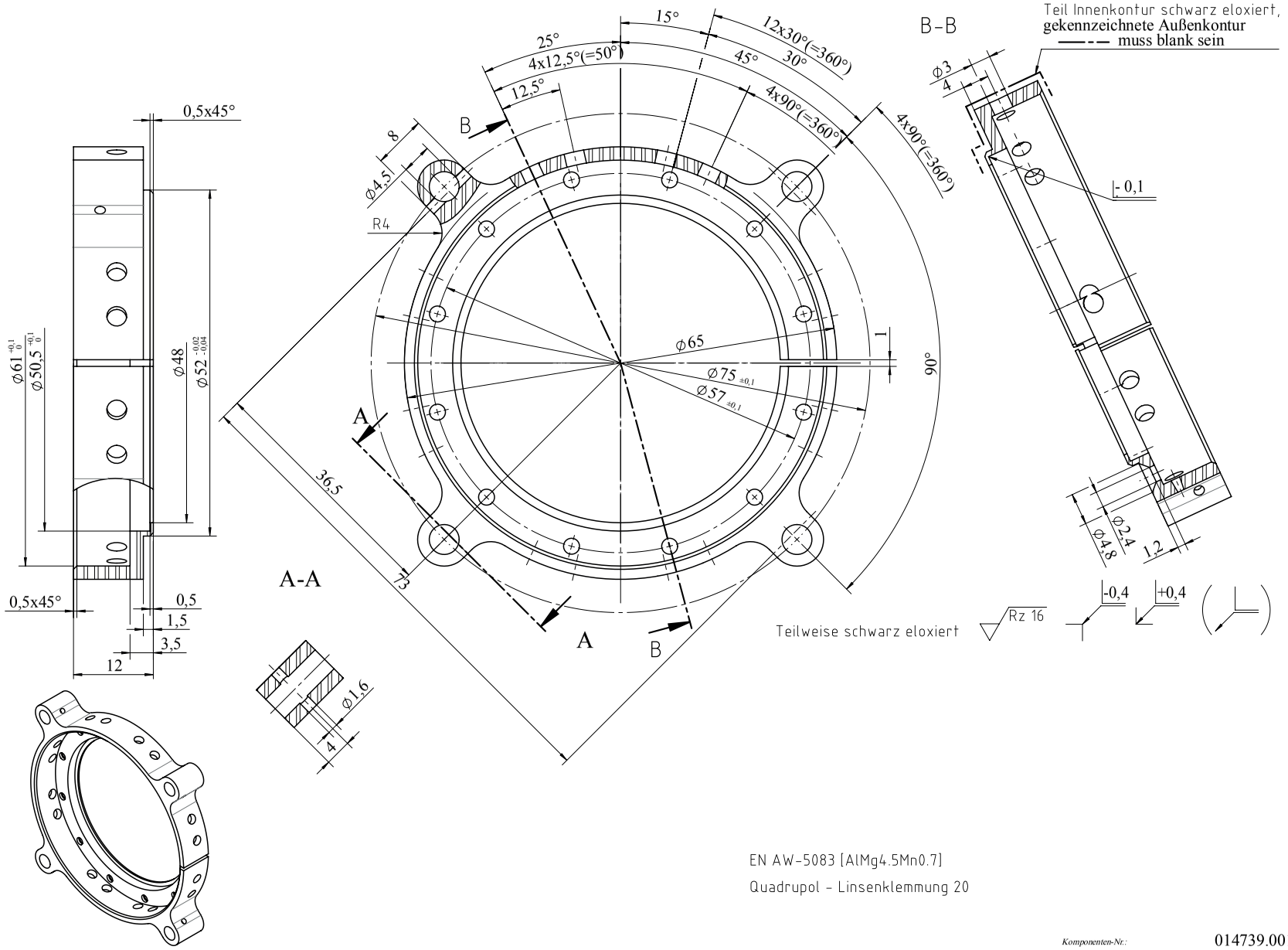

EN AW-5083 [AlMg4.5Mn0.7]

Quadrupol - Linsenklemmung 20

Komponenten-Nr.: 014739.001

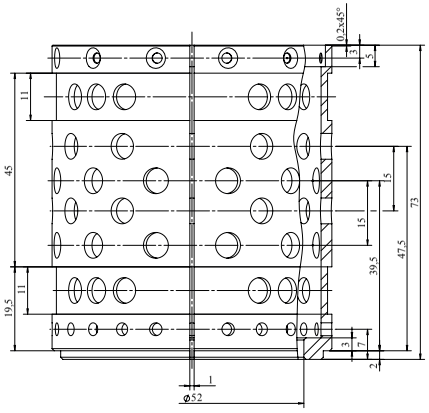

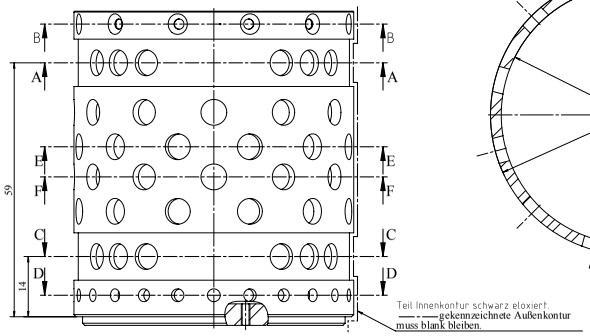

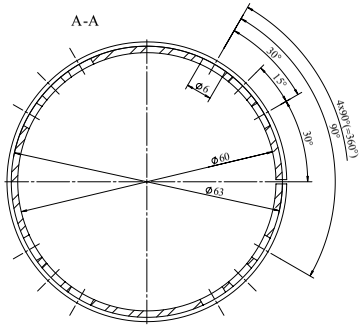

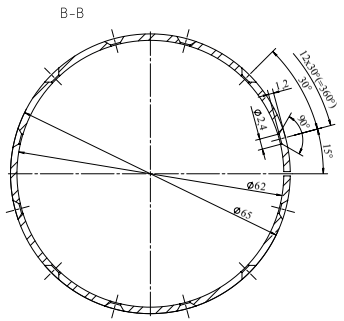

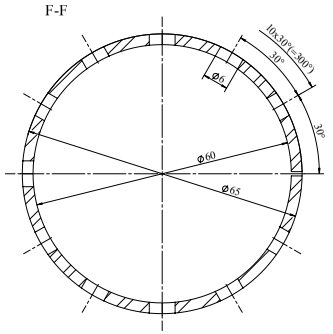

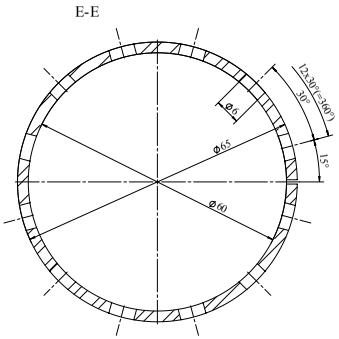

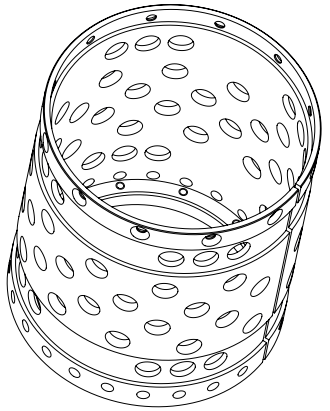

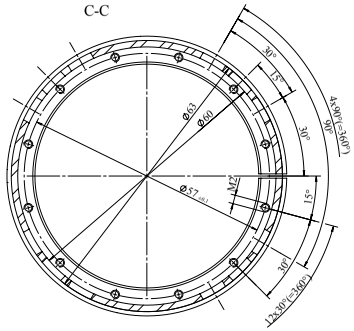

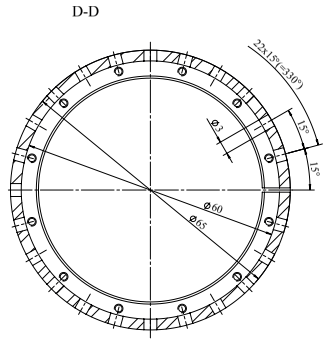

Teilweise schwarz eloxiert

Nicht bemaßte Fasen 0,5x45°

EN AW-5083 [AlMg4,5Mn0,7]
Rohr 20

Kompensation-Nr.: 014740.001

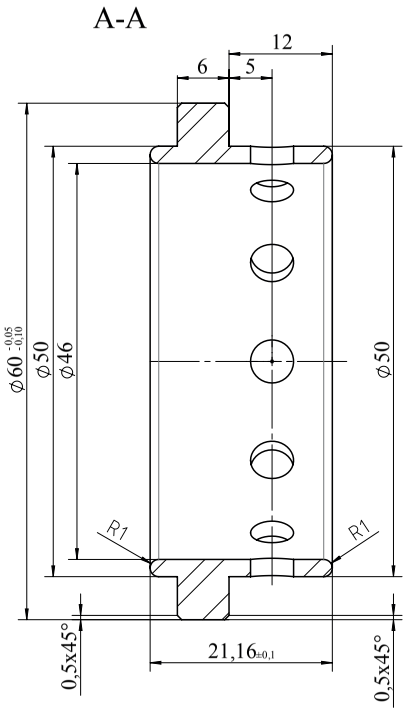

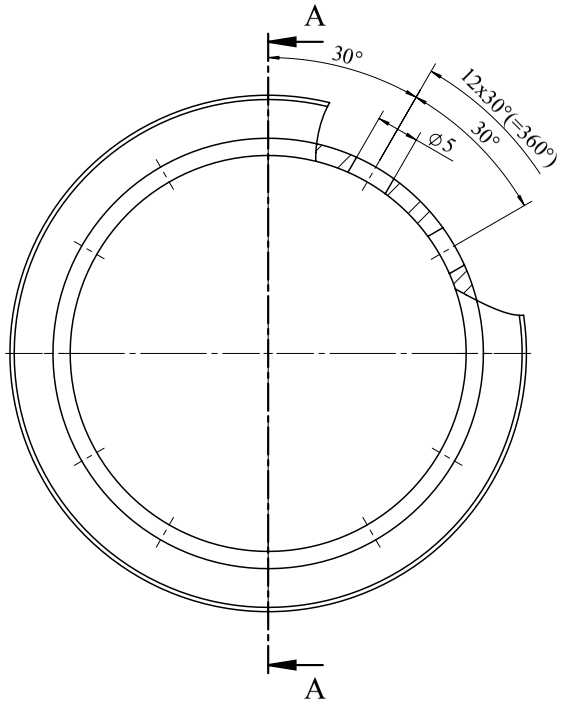

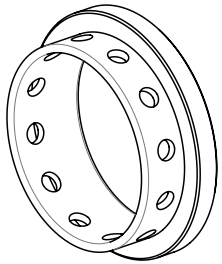

schwarz eloxiert

EN AW-5083 [AlMg4.5Mn0.7]

Abstandsring 21

Komponenten-Nr.: 014744.001

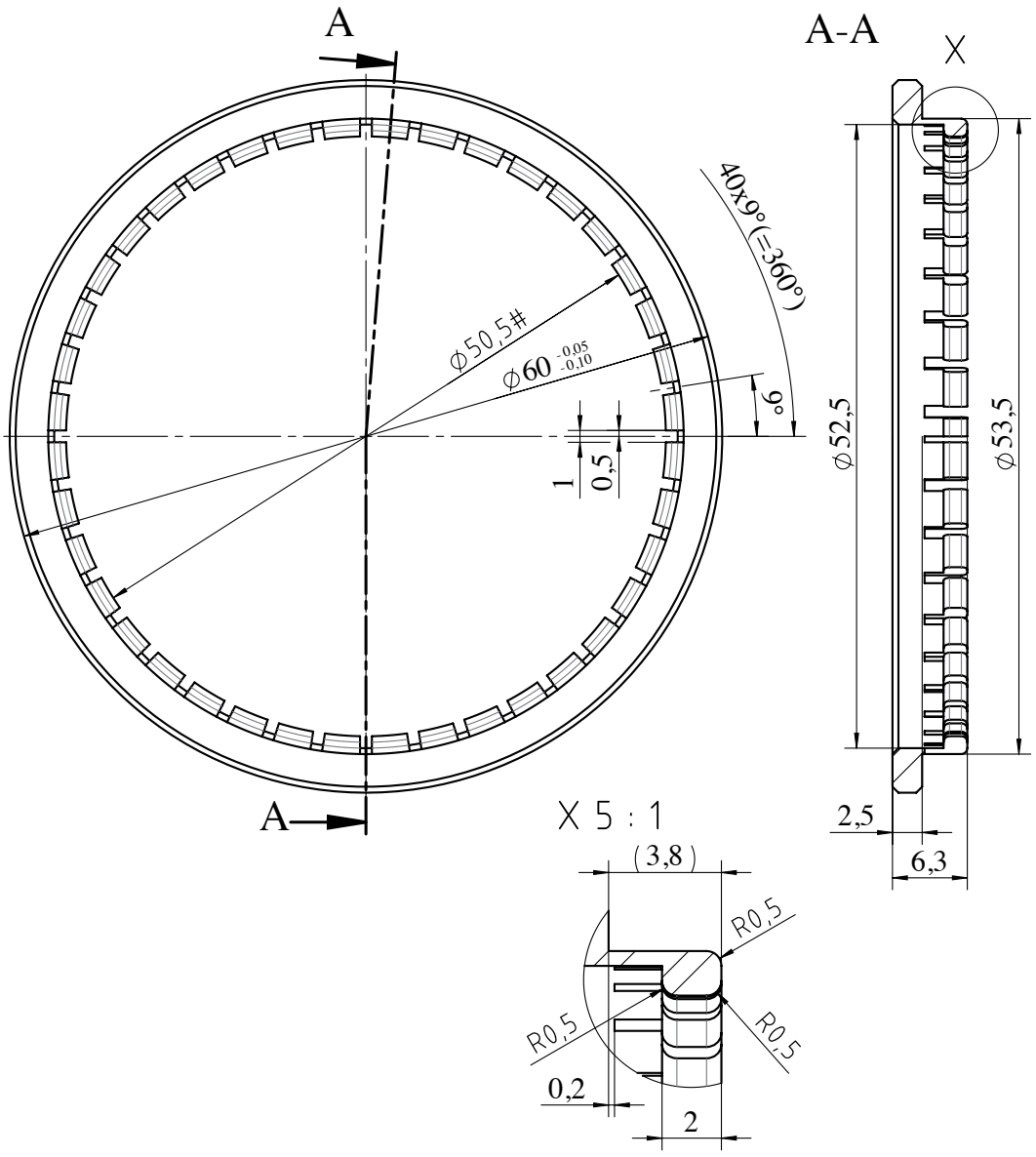

schwarz eloxiert

Nicht bemaßte Fasen 0,5x45°

EN AW-5083 [AlMg4.5Mn0.7]

Zentrierring 21

Komponenten-Nr.: 014747.001

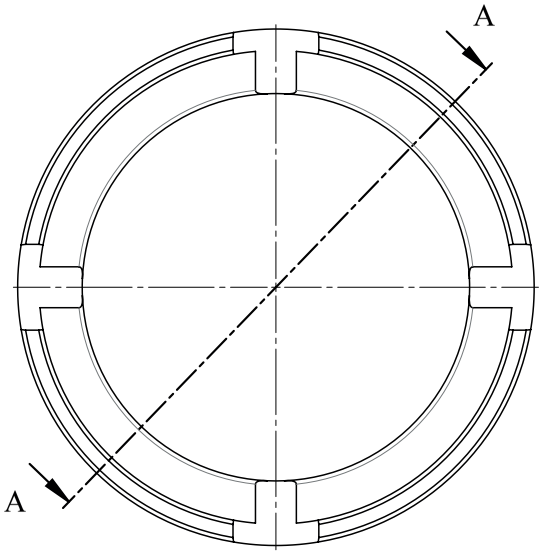

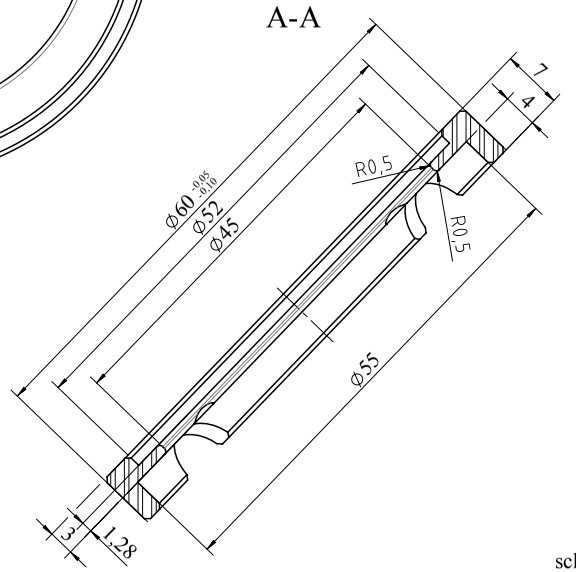

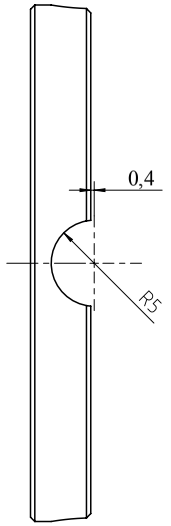

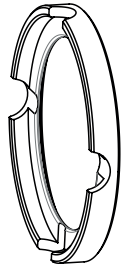

schwarz eloxiert

Nicht bemßte Fasen 0,5x45°

EN AW-5083 [AlMg4.5Mn0.7]

Abstandsring 22

Komponenten-Nr.: 014748.001

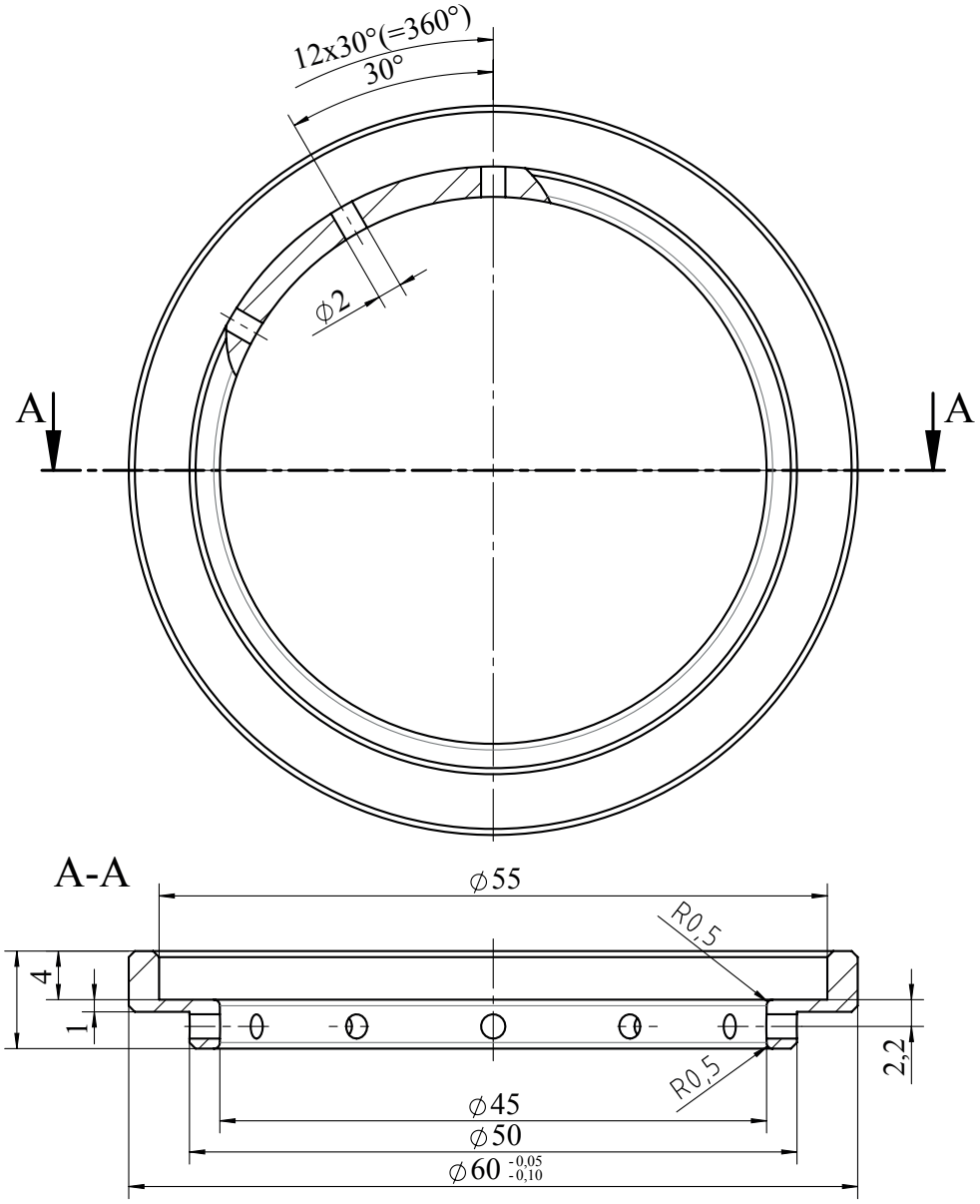

Nicht bemeaßte Fasen 0,5x45°

schwarz eloxiert

EN AW-5083 [AlMg4.5Mn0.7]

Abstandsring 23

Komponenten-Nr.: 014749.001

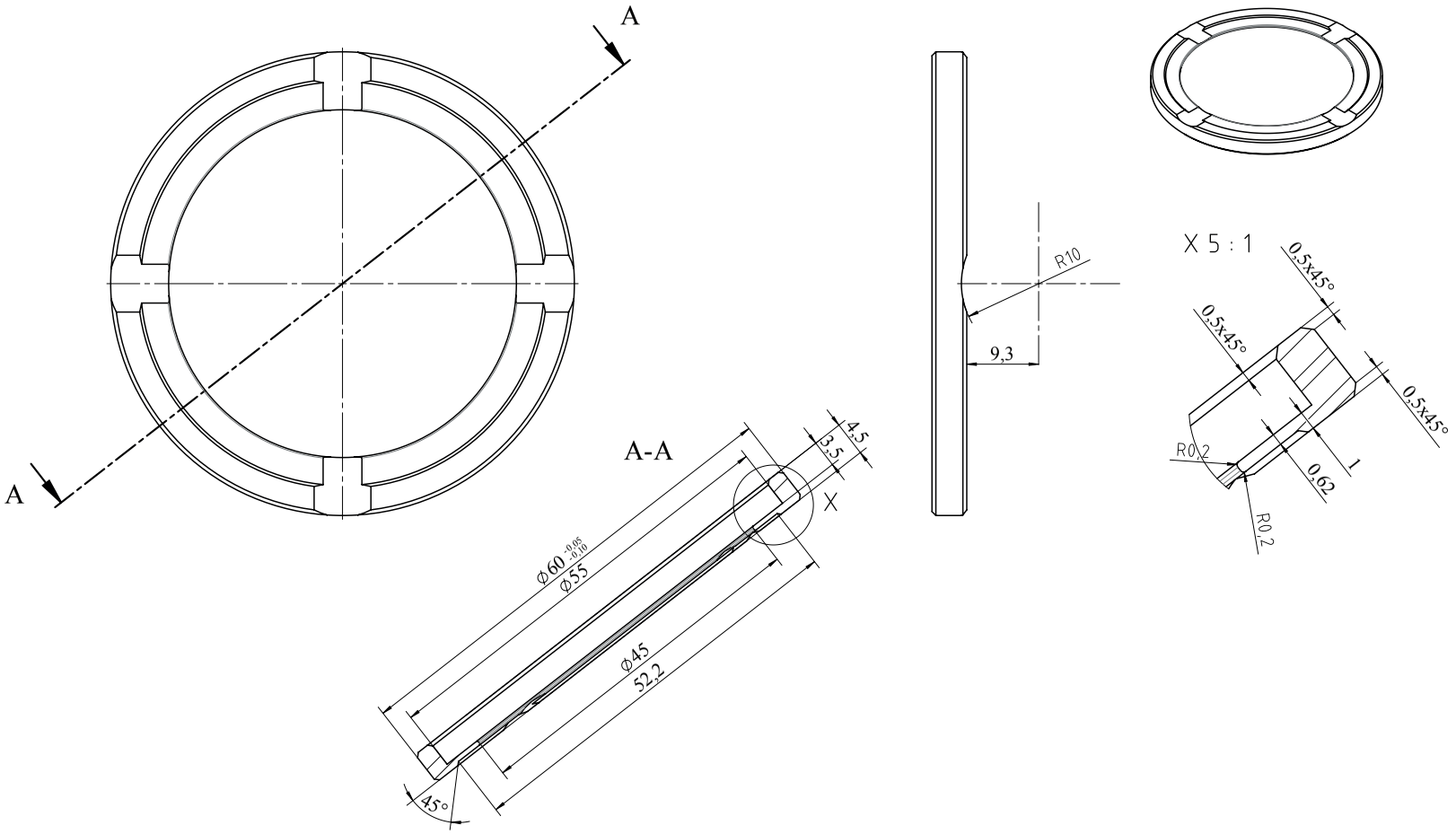

schwarz eloxiert

EN AW-5083 [AlMg4.5Mn0.7]

Abstandsring 24

Komponenten-Nr.: 014750.001

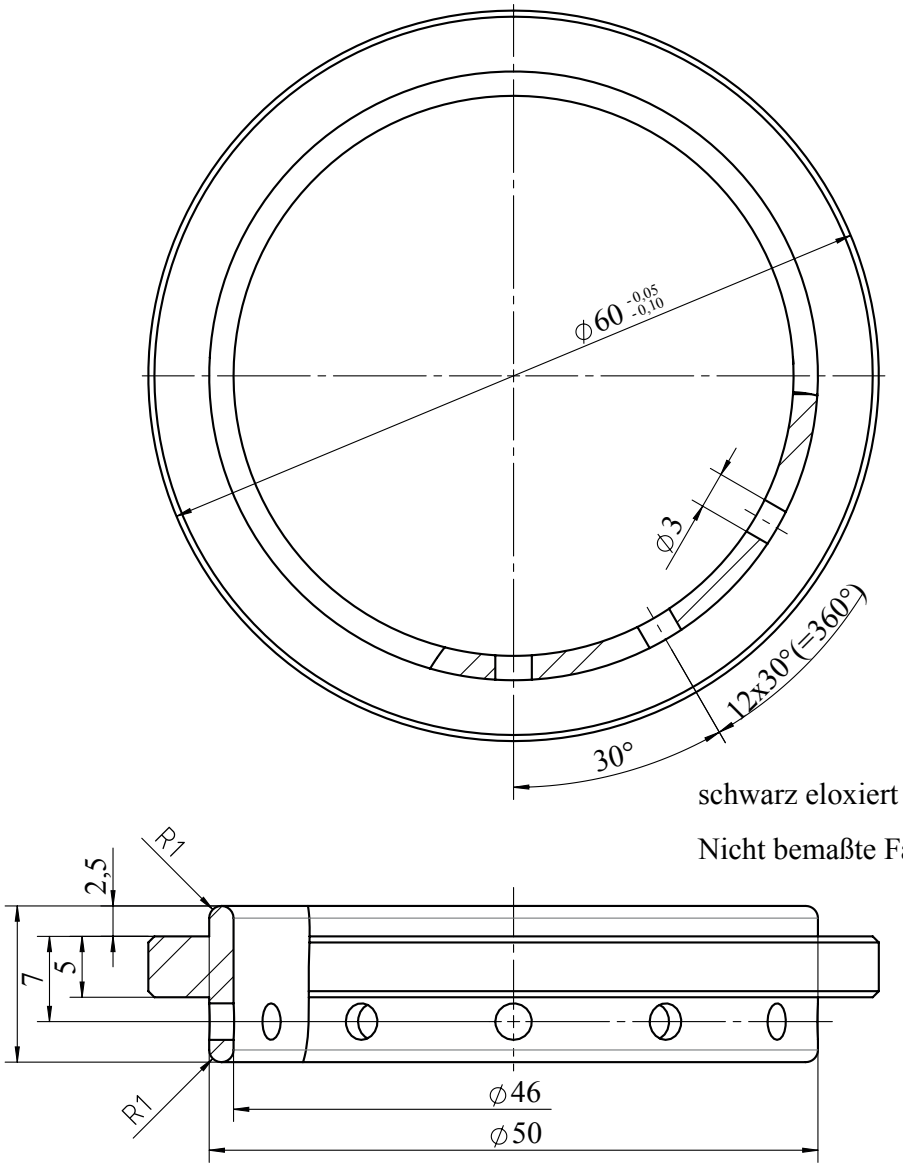

schwarz eloxiert

Nicht bemaßte Fasen 0,5x45°

Material: EN AW-5083 [AlMg4.5Mn0.7]

Benennung: Abstandsring 25

Komponenten-Nr.: 014751.001

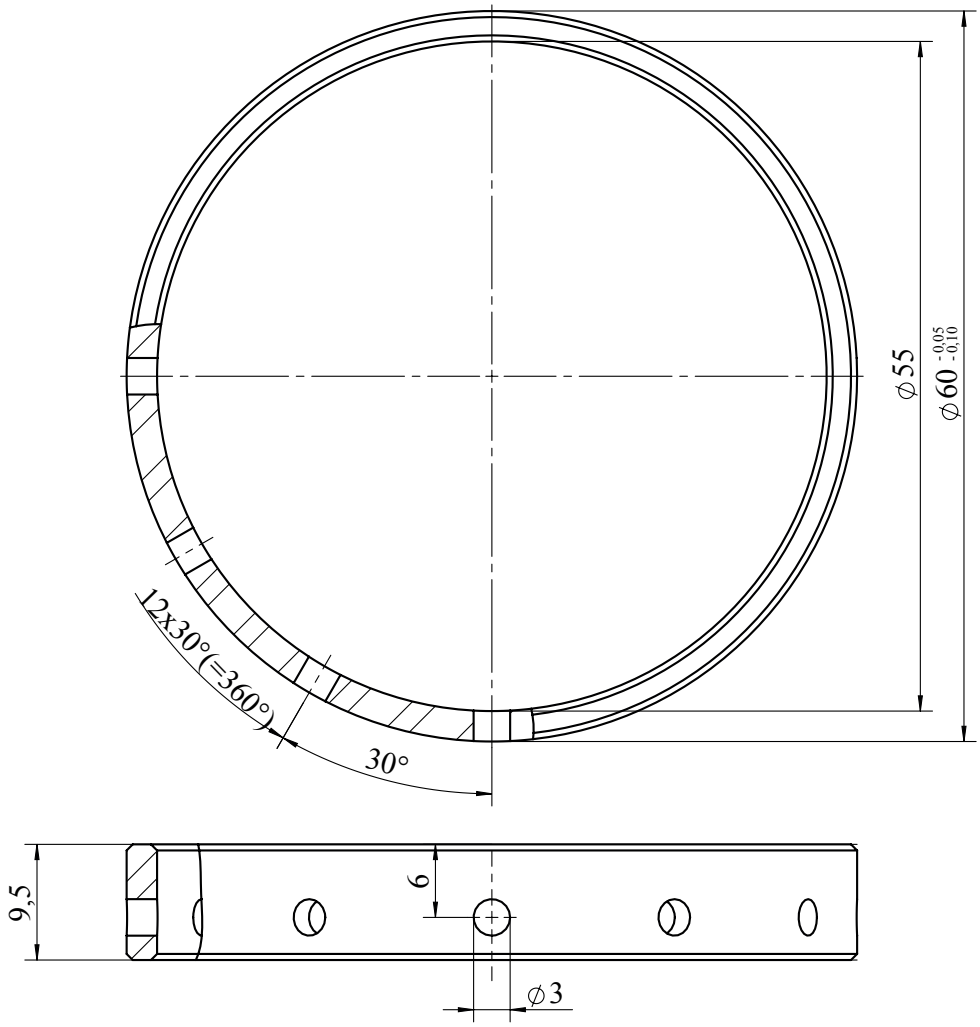

schwarz eloxiert

Nicht bemaßte Fasen 0,5x45°

EN AW-5083 [AlMg4.5Mn0.7]

Sicherungsring 01

Komponenten-Nr.: 014752.001

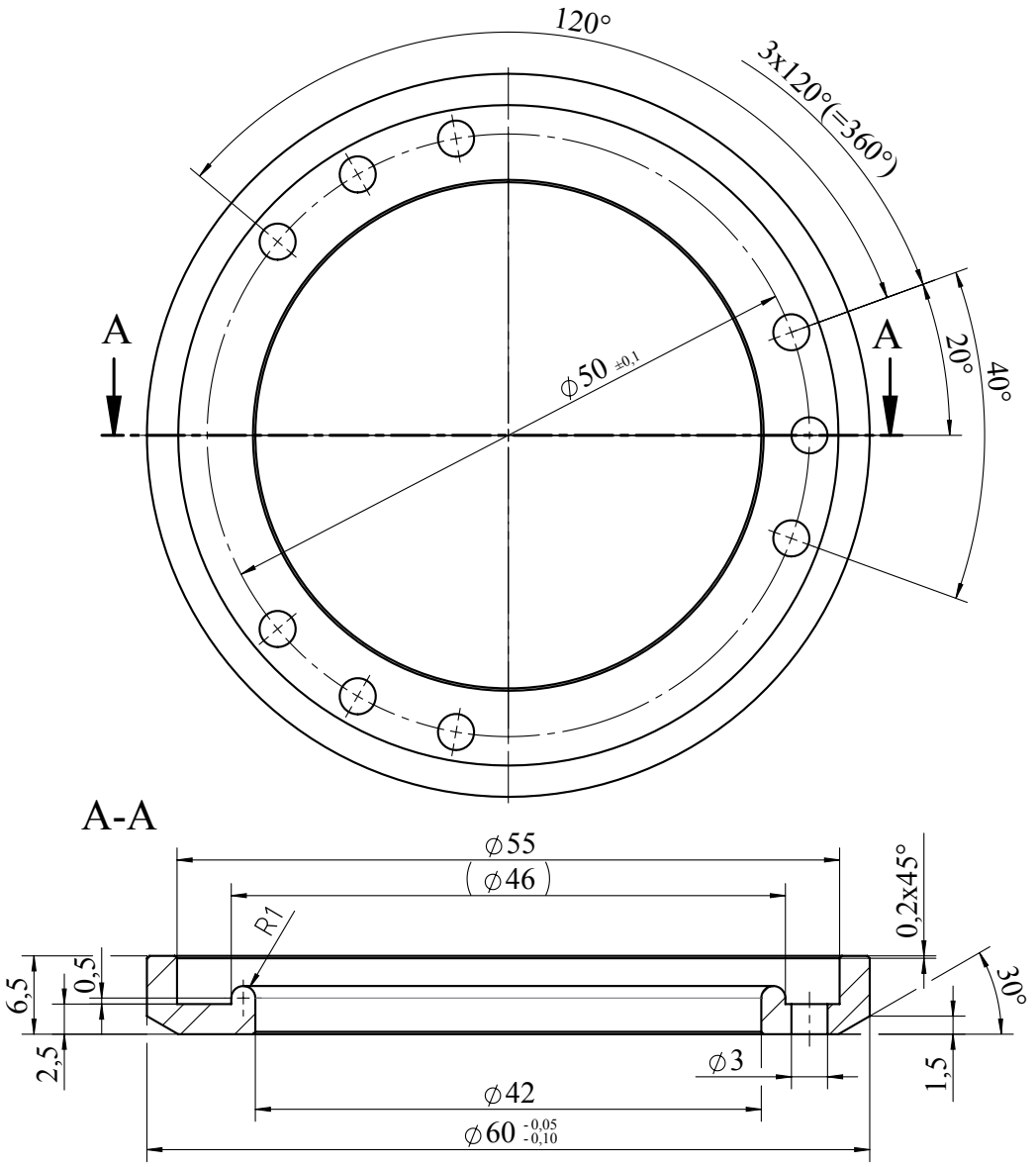

schwarz eloxiert

Nicht bemaßte Fasen 0,2x45°

EN AW-5083 [AlMg4.5Mn0.7]

Abstandsring 26

Komponenten-Nr.: 014753.001

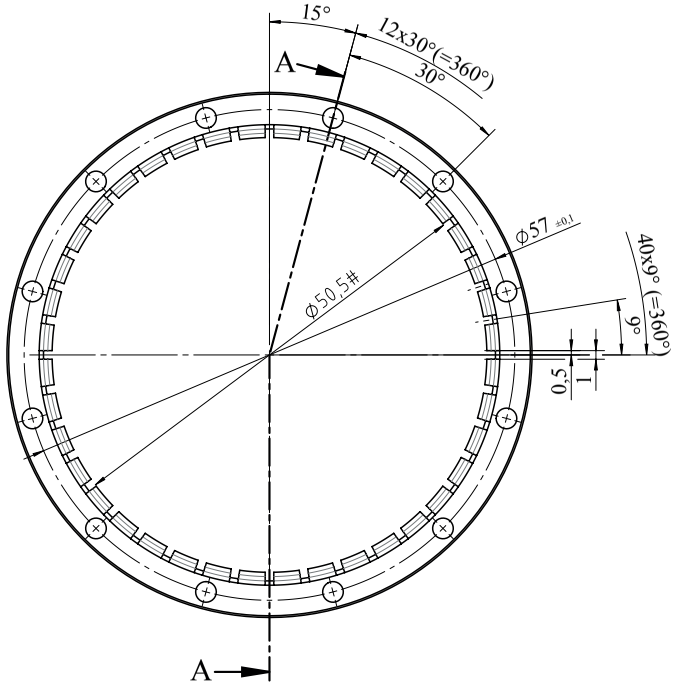

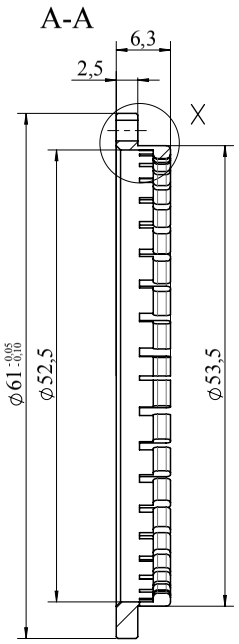

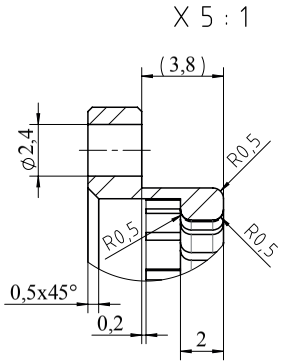

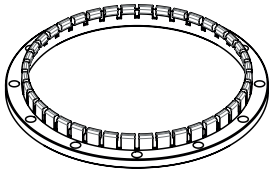

schwarz eloxiert

Nicht bemaßte Fasen 0,2x45°

EN AW-5083 [AlMg4.5Mn0.7]

Zentrierring 22

Komponenten-Nr.: 014754.001

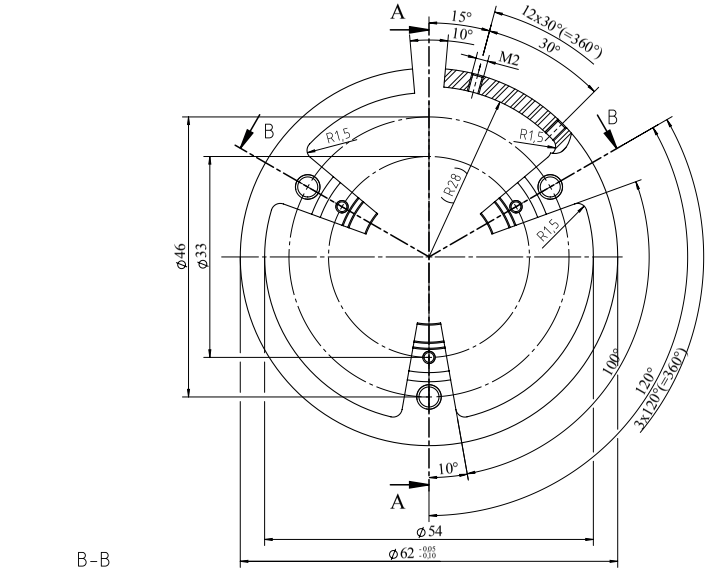

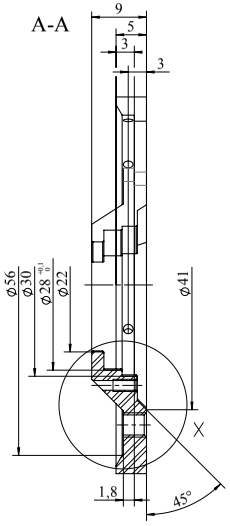

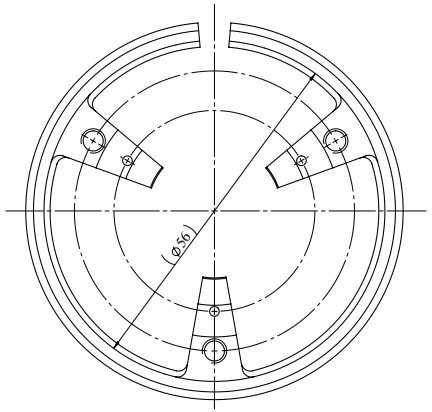

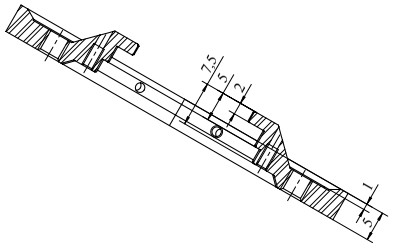

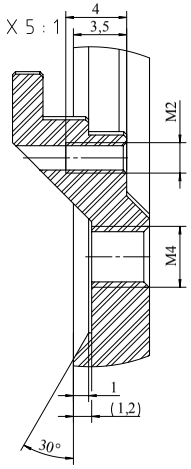

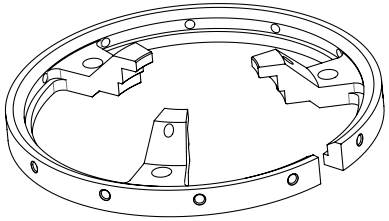

schwarz eloxiert

Nicht bemaßte Fasen 0,2x45°

EN AW-5083 [AlMg4.5Mn0.7]

Abschlussring 01

Komponenten-Nr.: 014755.001

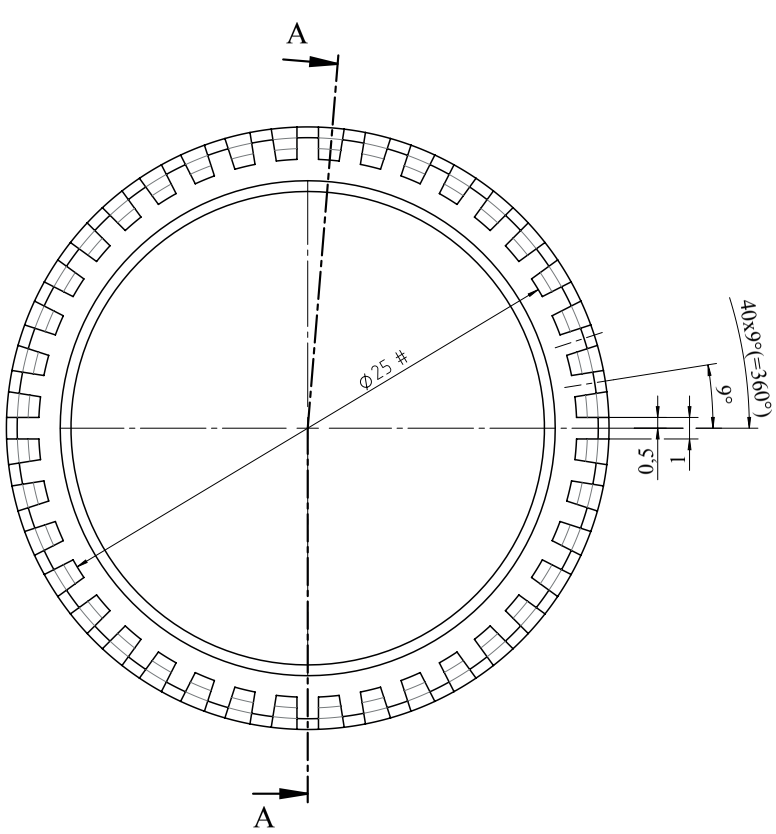

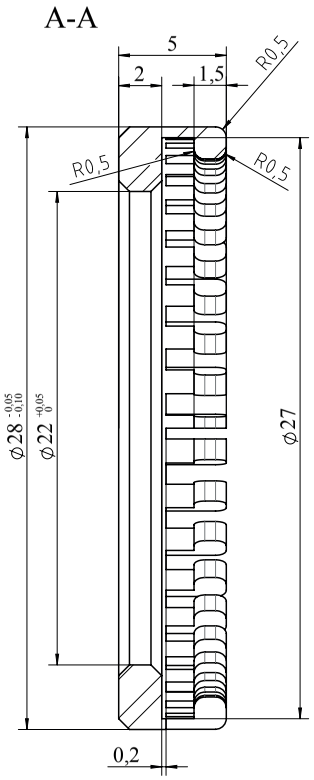

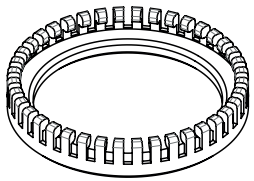

schwarz eloxiert

Nicht bemaßte Fasen 0,5x45°

EN AW-5083 [AlMg4.5Mn0.7]

Zentrierring 22

Komponenten-Nr.: 014757.001

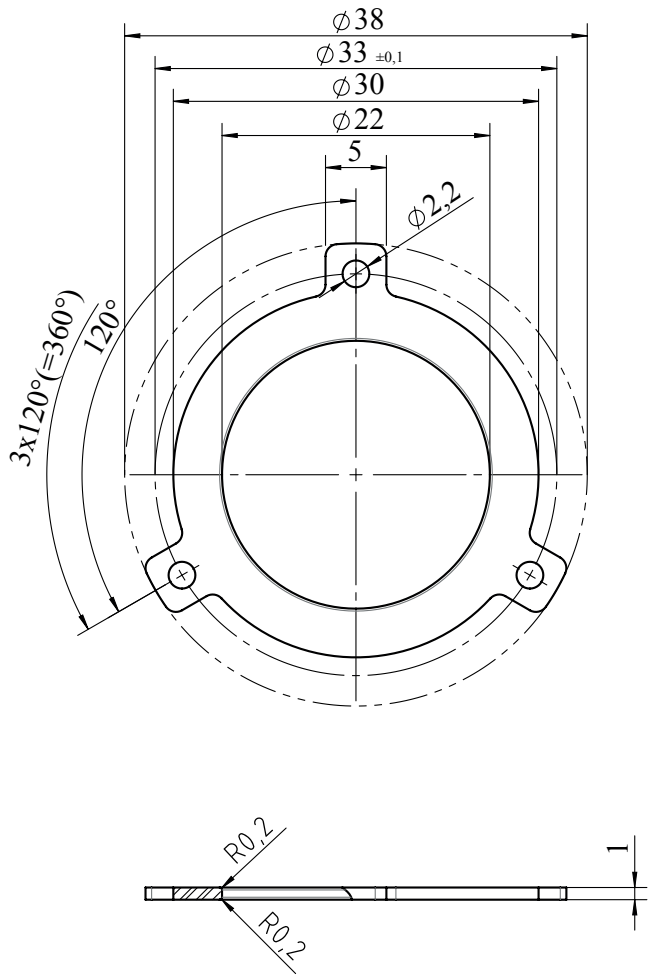

schwarz eloxiert

Nicht bemaßte Radien R1

EN AW-5083 [AlMg4.5Mn0.7]

Druckscheibe 21

Komponenten-Nr.: 014758.001

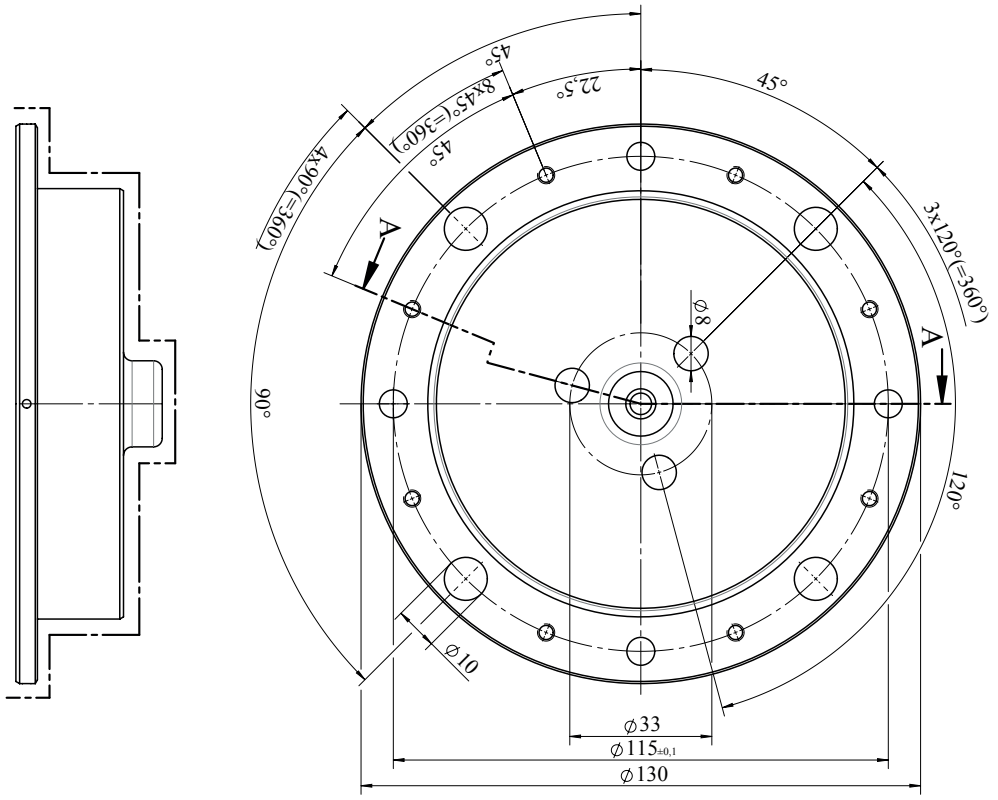

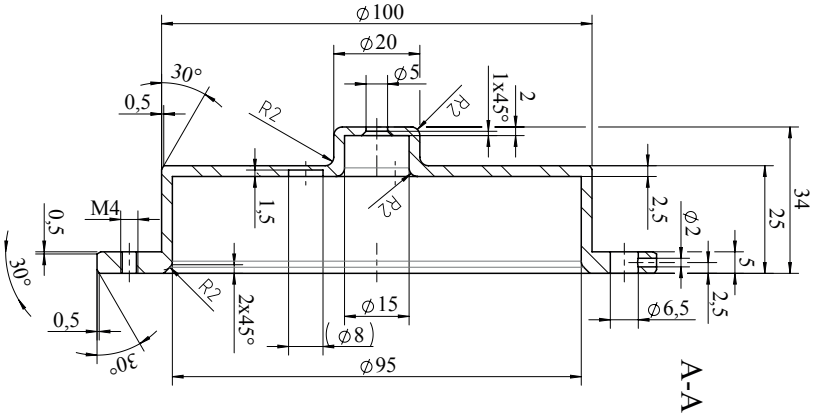

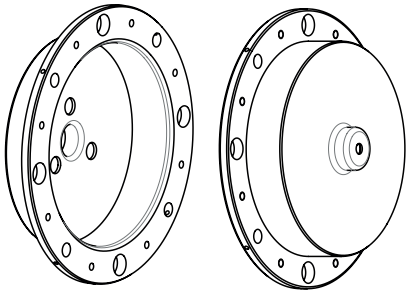

innen schwarz eloxiert
außen blank
EN AW-5083 [AlMg4.5Mn0.7]
Abdeckung 21

Komponenten-Nr.: 014759.001

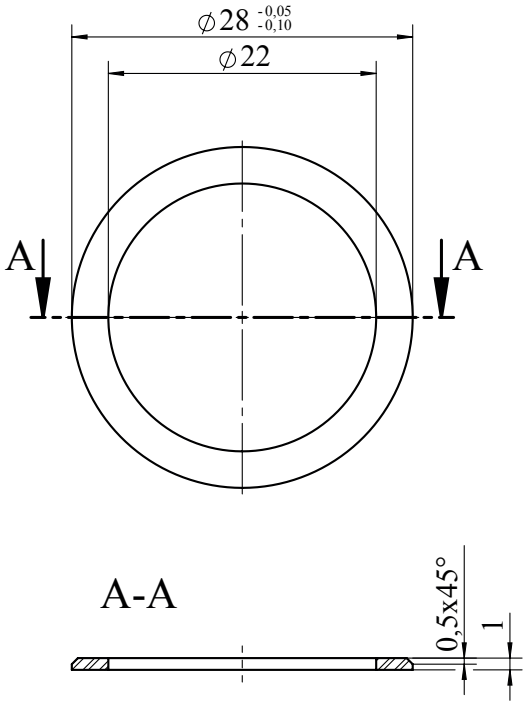

schwarz eloxiert

EN AW-5083 [AlMg4.5Mn0.7]

Passscheibe 01

Komponenten-Nr.: 014760.001

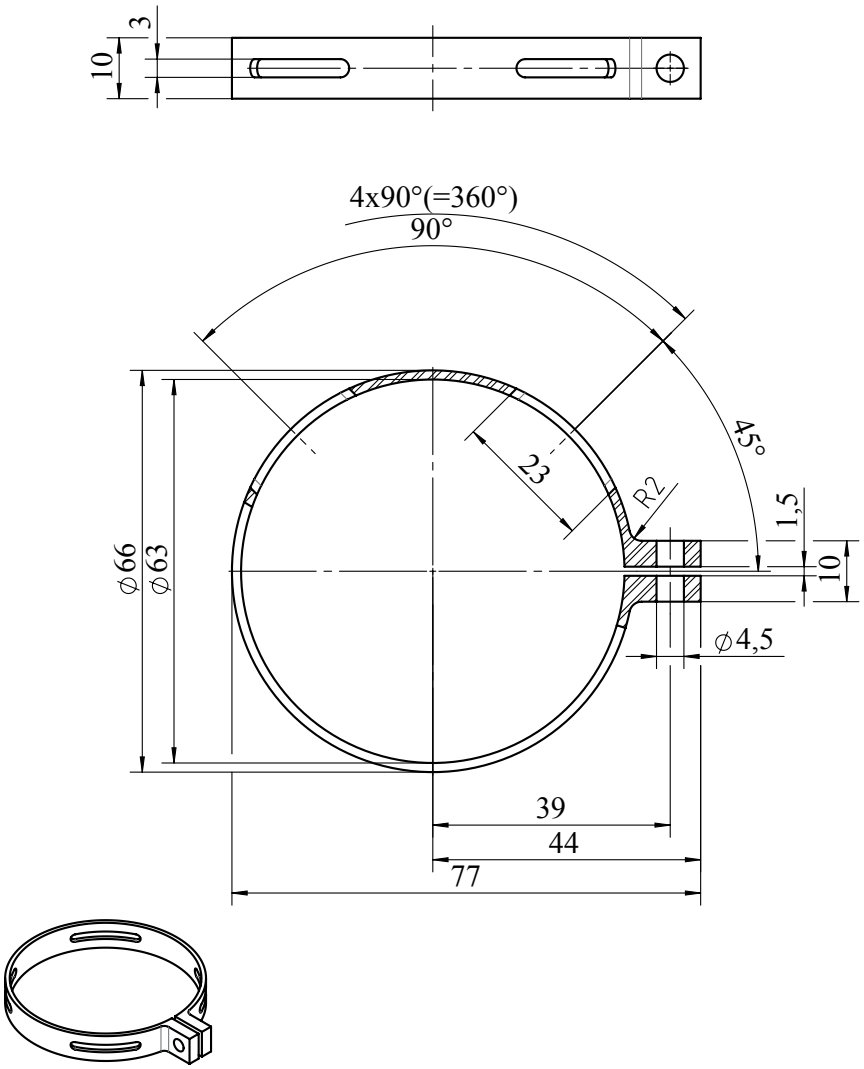

EN AW-5083 [AlMg4.5Mn0.7]

Schelle 01

Komponenten-Nr.: 014767.001

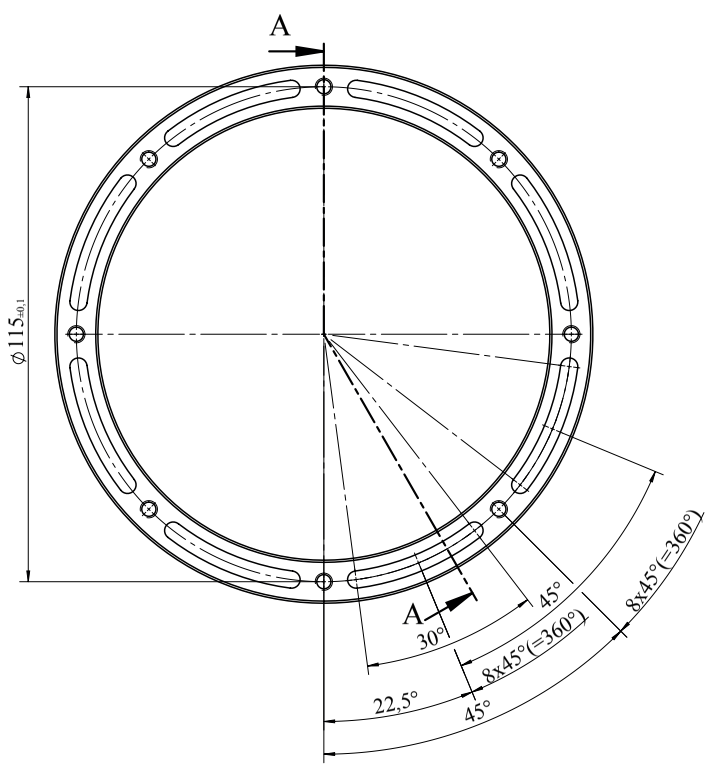

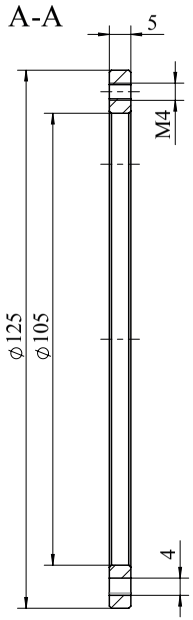

Nicht bemaßte Fasen 0,5x45°

1.4435 (X2CrNiMo18-14-3)

Monatagering 21

Komponenten-Nr.:	014773.001
2	1

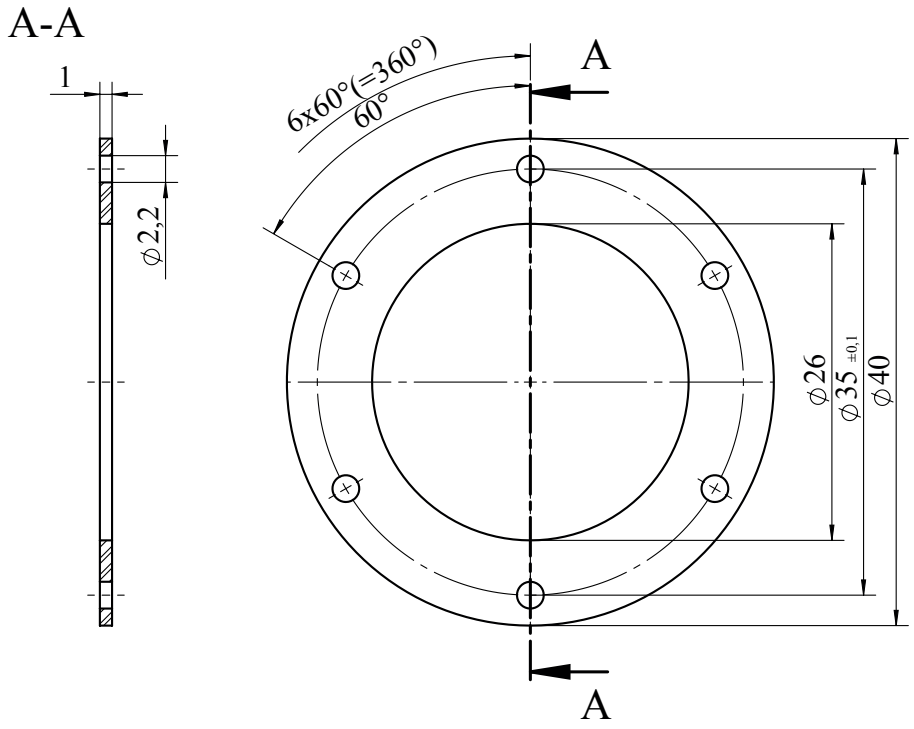

schwarz eloxiert

EN AW-5083 [AlMg4.5Mn0.7]

Sicherungsscheibe 21

Komponenten-Nr.: 014780.001

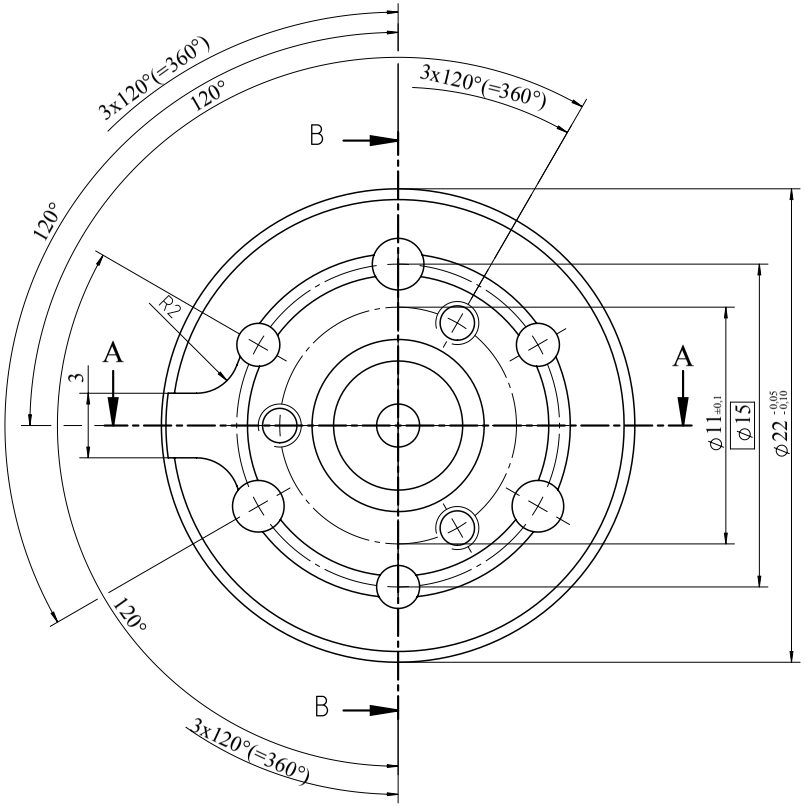

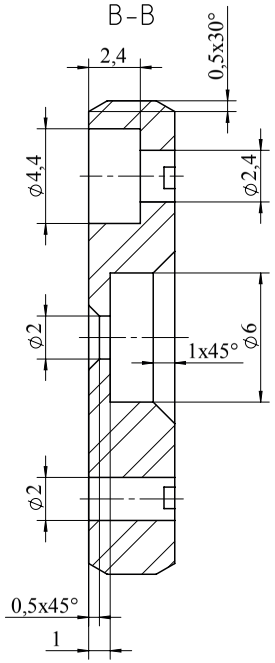

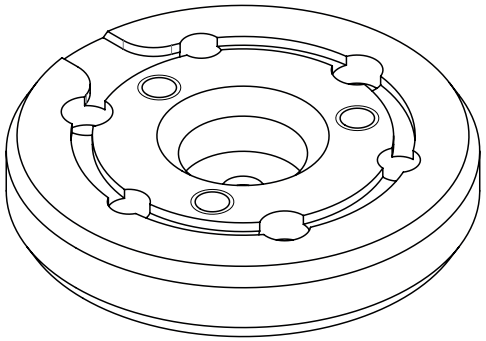

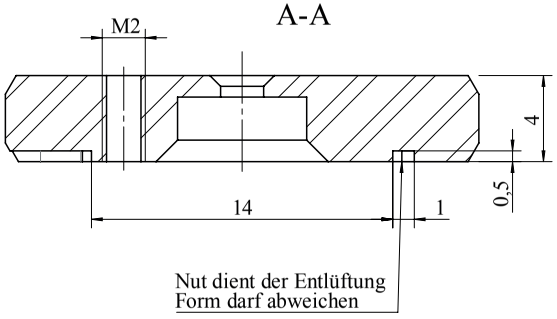

schwarz eloxiert

EN AW-5083 [AlMg4.5Mn0.7]

Diaphragm 02

Komponenten-Nr.: 014790.001

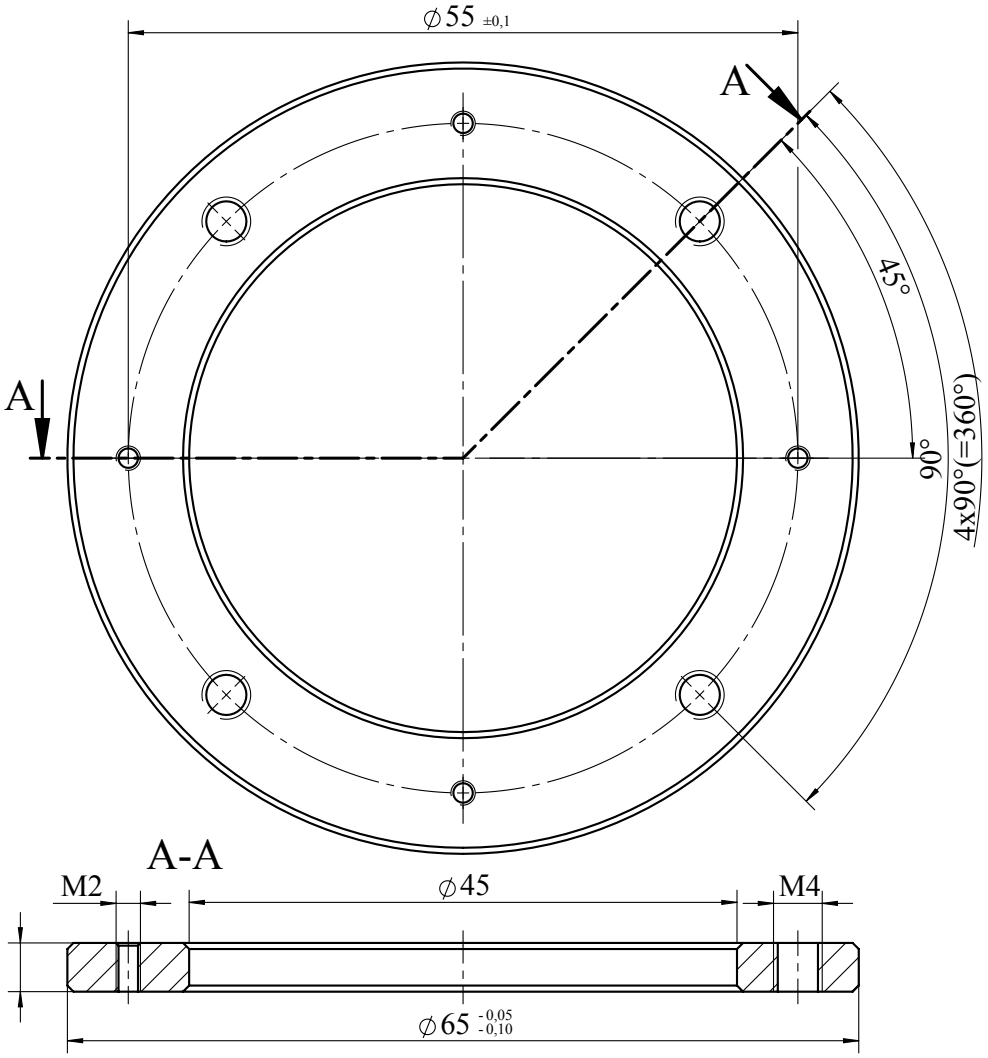

Nicht bemaßte Fasen 0,5x45°

Material: AISI Type 316L Edelstahl

Benennung: Montagering 02

Komponenten-Nr.: 014791.001

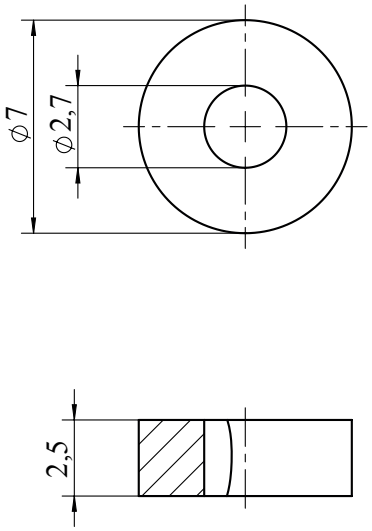

AISI Type 316L Edelstahl

Sonderscheibe 02

Komponenten-Nr.: 014802.001

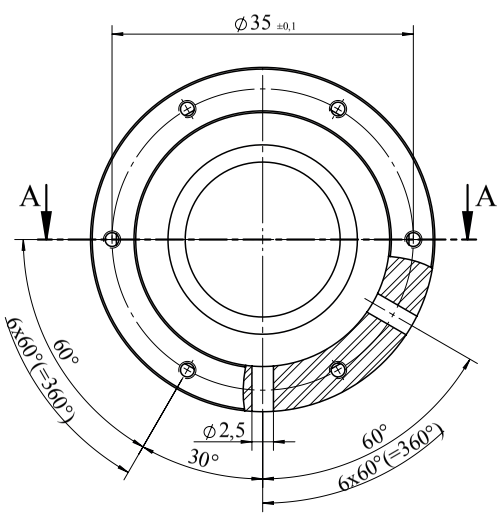

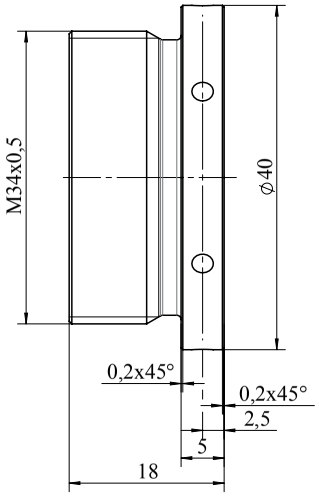

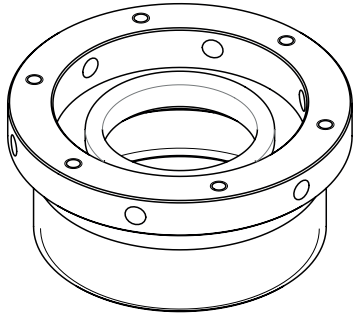

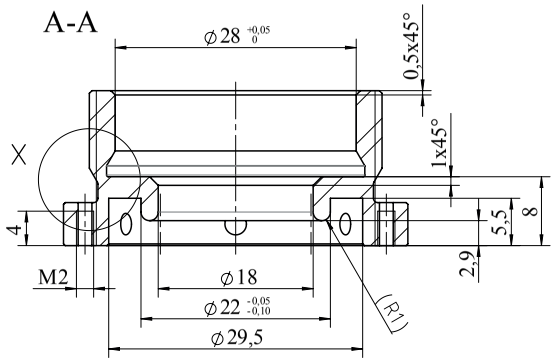

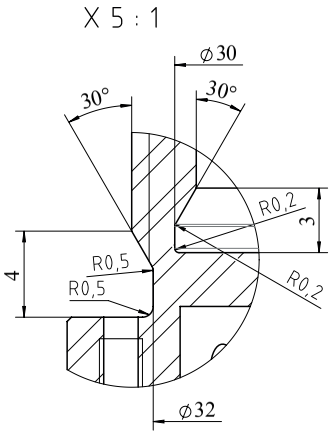

schwarz eloxiert

EN AW-5083 [AlMg4.5Mn0.7]

Aufnahme 22

Komponenten-Nr.: 014888.001

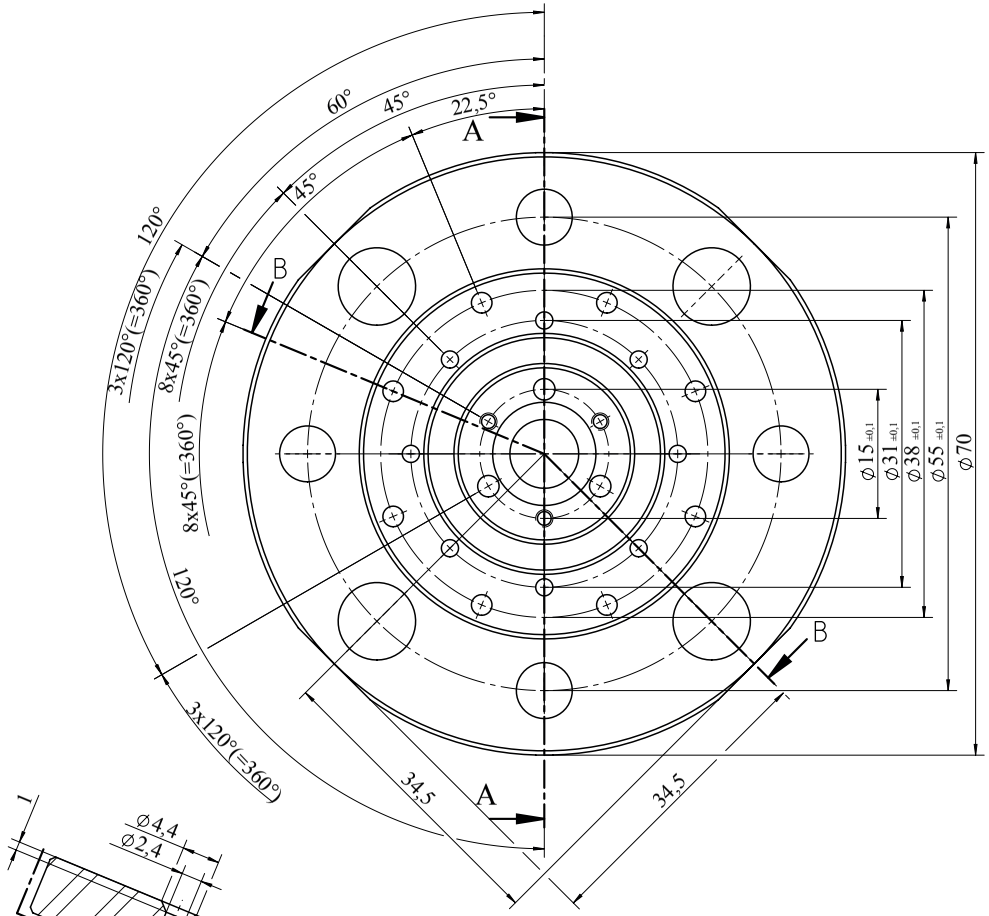

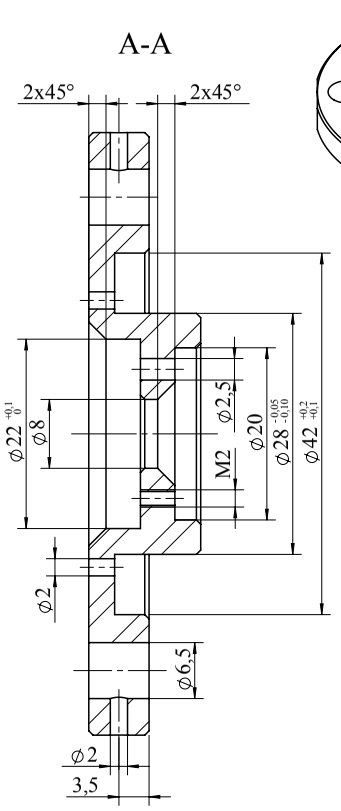

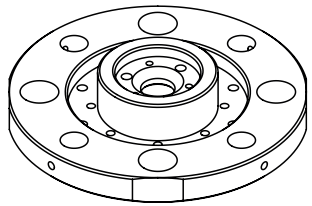

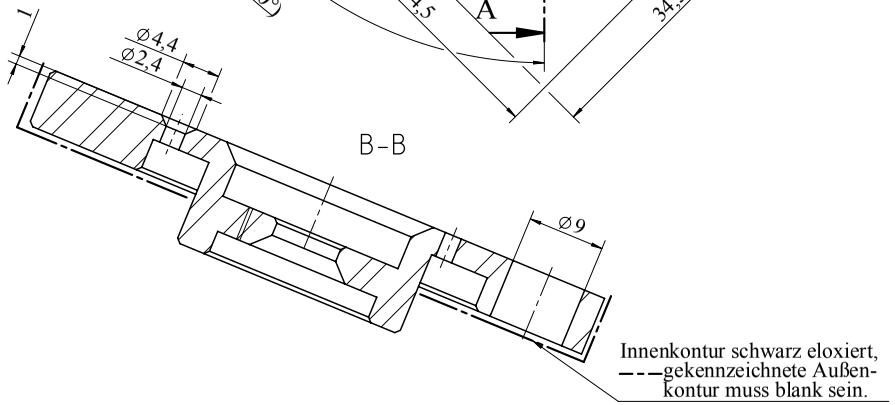

Innenkontur schwarz eloxiert,
– – – gekennzeichnete Außenkontur muss blank sein.

Teilweise schwarz eloxiert

Nicht bemaßte Fasen 0,5x45°

EN AW-5083 [AlMg4.5Mn0.7]

Aufnahme 23

Komponenten-Nr.: 014889.001

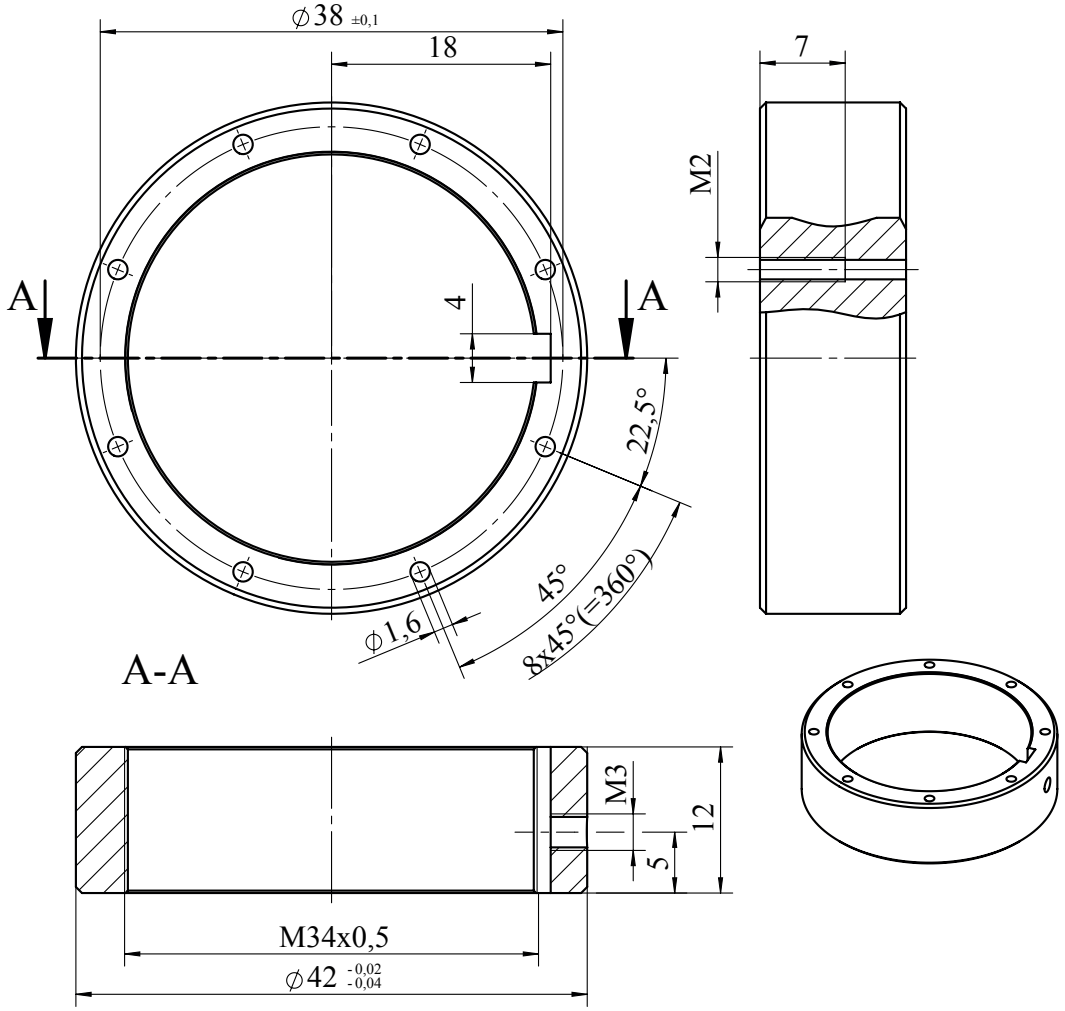

Nicht bemaßte Fasen 0,5x45°

AISI Type 316L Edelstahl

Gewindebuchse M34x0,5

Komponenten-Nr.: 014890.001

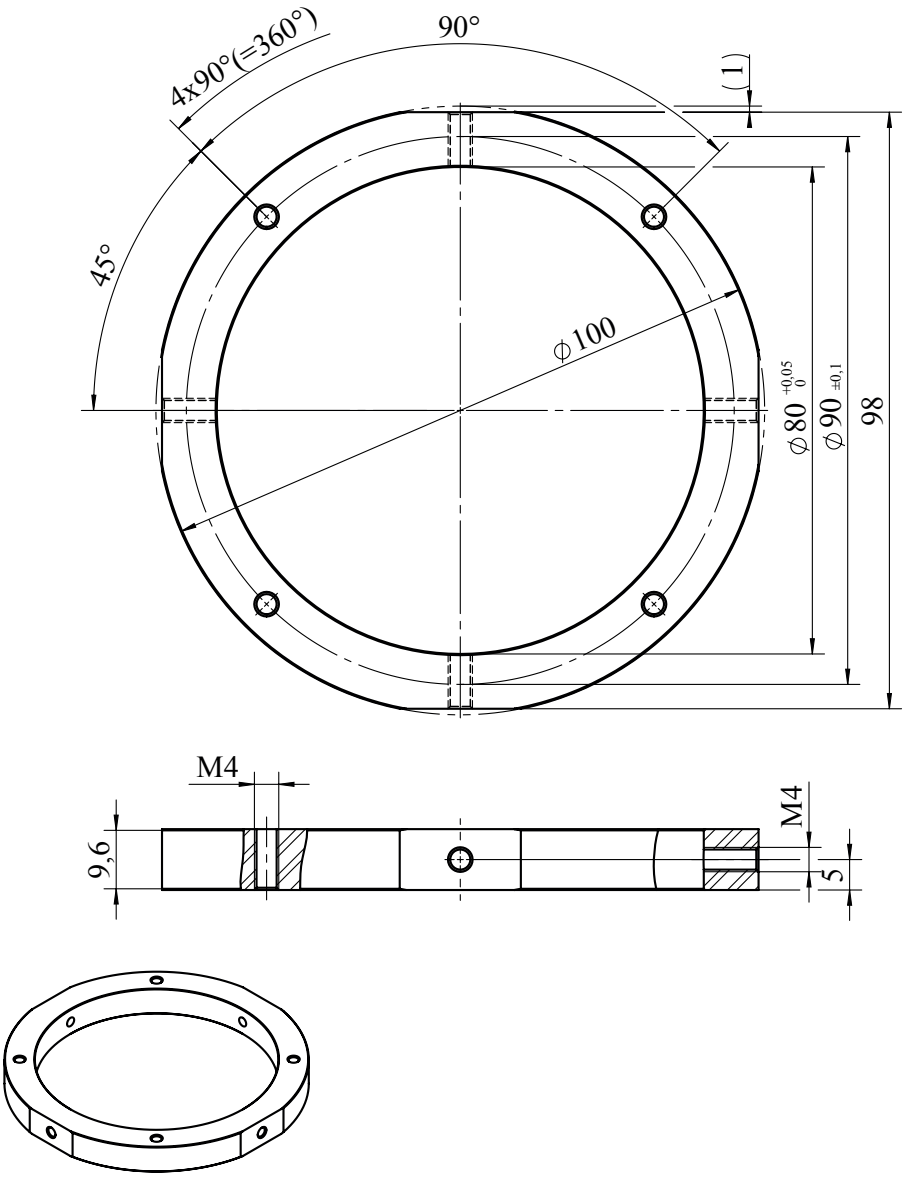

EN AW-5083 [AlMg4.5Mn0.7]

Justierring 01

Komponenten-Nr.: 014891.001

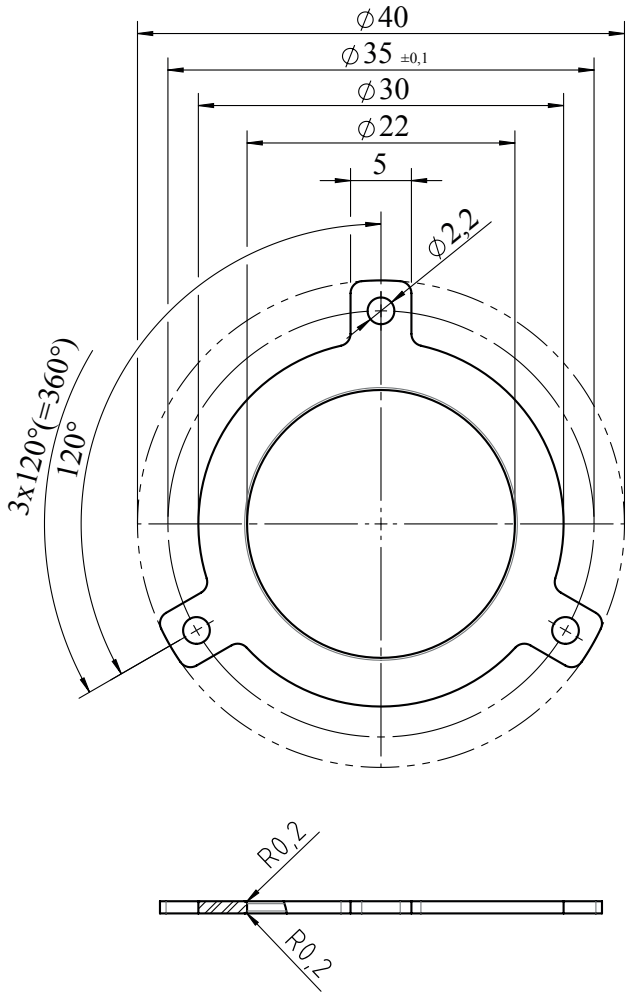

schwarz eloxiert

Nicht bemaßte Radien R1

EN AW-5083 [AlMg4.5Mn0.7]

Druckscheibe 22

Komponenten-Nr.: 015014.001

BIBLIOGRAPHY

[1] A. Einstein, "Die Grundlage der allgemeinen Relativitätstheorie," *Annalen der Physik*, vol. 354, no. 7, pp. 769–822, 1916.

[2] B. P. Abbott, "Observation of gravitational waves from a binary black hole merger," in *Centennial of General Relativity*, pp. 291–311, WORLD SCIENTIFIC, feb 2017.

[3] J.-P. Uzan, "Varying Constants, Gravitation and Cosmology," *Living Reviews in Relativity*, vol. 14, mar 2011.

[4] M. Safronova, D. Budker, D. DeMille, D. F. J. Kimball, A. Derevianko, and C. W. Clark, "Search for new physics with atoms and molecules," *Reviews of Modern Physics*, vol. 90, jun 2018.

[5] M. Pospelov and A. Ritz, "Electric dipole moments as probes of new physics," *Annals of Physics*, vol. 318, pp. 119–169, jul 2005.

[6] I. B. Khriplovich and S. K. Lamoreaux, *CP Violation Without Strangeness*. Springer Berlin Heidelberg, 1997.

[7] J. K. Webb, J. A. King, M. T. Murphy, V. V. Flambaum, R. F. Carswell, and M. B. Bainbridge, "Indications of a Spatial Variation of the Fine Structure Constant," *Physical Review Letters*, vol. 107, oct 2011.

[8] J. C. Berengut and V. V. Flambaum, "Manifestations of a spatial variation of fundamental constants in atomic and nuclear clocks, Oklo, meteorites, and cosmological phenomena," *EPL (Europhysics Letters)*, vol. 97, p. 20006, jan 2012.

[9] G. Gabrielse, A. Khabbaz, D. S. Hall, C. Heimann, H. Kalinowsky, and W. Jhe, "Precision Mass Spectroscopy of the Antiproton and Proton Using Simultaneously Trapped Particles," *Physical Review Letters*, vol. 82, pp. 3198–3201, apr 1999.

[10] I. Draganić, J. R. C. López-Urrutia, R. DuBois, S. Fritzsche, V. M. Shabaev, R. S. Orts, I. I. Tupitsyn, Y. Zou, and J. Ullrich, "High Precision Wavelength Measurements of QED-Sensitive Forbidden Transitions in Highly Charged Argon Ions," *Physical Review Letters*, vol. 91, oct 2003.

[11] R. Shaniv, R. Ozeri, M. Safronova, S. Porsev, V. Dzuba, V. Flambaum, and H. Häffner, "New Methods for Testing Lorentz Invariance with Atomic Systems," *Physical Review Letters*, vol. 120, mar 2018.

[12] M. Kozlov, M. Safronova, J. C. López-Urrutia, and P. Schmidt, "Highly-charged ions: Optical clocks and applications in fundamental physics," *Reviews of Modern Physics*, vol. 90, dec 2018.

[13] J. Fraunhofer, "Bestimmung des Brechungs- und des Farbenzerstreungs-Vermögens verschiedener Glasarten, in Bezug auf die Vervollkommnung achromatischer Fernröhre," *Annalen der Physik*, vol. 56, no. 7, pp. 264–313, 1817.

[14] G. Kirchhoff and R. Bunsen, "Chemische Analyse durch Spectralbeobachtungen," *Journal fuer Praktische Chemie*, vol. 80, no. 1, pp. 449–477, 1860.

[15] G. Kirchhoff, "Ueber die Fraunhofer'schen Linien," *Journal fuer Praktische Chemie*, vol. 80, no. 1, pp. 480–486, 1860.

[16] A. A. Michelson and E. W. Morley, "On a method of making the wavelength of sodium light the actual and practical standard of length," *American Journal of Science*, vol. s3-34, pp. 427–430, dec 1887.

[17] A. Sommerfeld, "Zur Feinstruktur der Wasserstofflinien. Geschichte und gegenwaertiger Stand der Theorie," *Die Naturwissenschaften*, vol. 28, pp. 417–423, jul 1940.

[18] T. H. Maiman, "Stimulated Optical Radiation in Ruby," *Nature*, vol. 187, pp. 493–494, aug 1960.

[19] J. Reichert, R. Holzwarth, T. Udem, and T. W. Hänsch, "Measuring the frequency of light with mode-locked lasers," *Optics Communications*, vol. 172, pp. 59–68, dec 1999.

[20] N. Huntemann, C. Sanner, B. Lipphardt, C. Tamm, and E. Peik, "Single-Ion Atomic Clock with 3×10^{-18} Systematic Uncertainty," *Physical Review Letters*, vol. 116, feb 2016.

[21] W. Paul and H. Steinwedel, "Notizen: Ein neues Massenspektrometer ohne Magnetfeld," *Zeitschrift fuer Naturforschung A*, vol. 8, jan 1953.

[22] W. Paul and M. Raether, "Das elektrische Massenfilter," *Zeitschrift fuer Physik*, vol. 140, pp. 262–273, may 1955.

[23] W. Paul, H. P. Reinhard, and U. von Zahn, "Das elektrische Massenfilter als Massenspektrometer und Isotopentrenner," *Zeitschrift fuer Physik*, vol. 152, pp. 143–182, apr 1958.

[24] E. Fischer, "Die dreidimensionale Stabilisierung von Ladungstraegern in einem Vierpolfeld," *Zeitschrift fuer Physik*, vol. 156, pp. 1–26, mar 1959.

[25] H. G. Dehmelt and F. G. Major, "Orientation of(He4)+Ions by Exchange Collisions with Cesium Atoms," *Physical Review Letters*, vol. 8, pp. 213–214, mar 1962.

[26] W. Johnson and G. Soff, "The lamb shift in hydrogen-like atoms, $1 \leqslant Z \leqslant 110$," *Atomic Data and Nuclear Data Tables*, vol. 33, pp. 405–446, nov 1985.

[27] L. Schmöger, "Kalte hochgeladene Ionen für Frequenzmetrologie," 2017.

[28] M. Schwarz, "Lasermanipulation von rotationsgekühlten Molekülionen in einer neuen kryogenen Paul-Falle," 2012.

[29] T. Leopold, *A cryogenic ion trap system for quantum logic spectroscopy of highly charged ions.* PhD thesis, QUEST Institute for Experimental Quantum Metrology, PTB-Braunschweig, 2018.

[30] V. Mäckel, R. Klawitter, G. Brenner, J. R. C. López-Urrutia, and J. Ullrich, "Laser Spectroscopy on Forbidden Transitions in Trapped Highly Charged Ar^{13+} Ions," *Physical Review Letters*, vol. 107, sep 2011.

[31] "https://upload.wikimedia.org/wikipedia/en/9/99/Jaansen_Microscope.jpg, (05.09.19)."

[32] K. Pyka, J. Keller, H. L. Partner, R. Nigmatullin, T. Burgermeister, D. M. Meier, K. Kuhlmann, A. Retzker, M. B. Plenio, W. H. Zurek, A. del Campo, and T. E. Mehlstäubler, "Topological defect formation and spontaneous symmetry breaking in ion Coulomb crystals," *Nature Communications*, vol. 4, aug 2013.

[33] M. Knoop, ed., *Physics with trapped charged particles*. Imperial College Press, 2014.

[34] J. E. Curtis and K. A. Museum, *Art and Empire: Treasures from Assyria in the British Museum*. Harry N Abrams Inc, 1995.

[35] L. A. Seneca, "Naturales quaestiones, liber i," 65 AD.

[36] T. C. Kriss and V. M. Kriss, "History of the Operating Microscope: From Magnifying Glass to Microneurosurgery," *Neurosurgery*, vol. 42, pp. 899–907, apr 1998.

[37] J. Stark, "Design ultrastabiler Hochfrequenzfelder für die Langzeitspeicherung hochgeladener Ionen," Master's thesis, Ruprecht-Karls-Universität, Heidelberg, 2015.

[38] P. Micke, S. Kühn, L. Buchauer, J. R. Harries, T. M. Bücking, K. Blaum, A. Cieluch, A. Egl, D. Hollain, S. Kraemer, T. Pfeifer, P. O. Schmidt, R. X. Schüssler, C. Schweiger, T. Stöhlker, S. Sturm, R. N. Wolf, S. Bernitt, and J. R. C. López-Urrutia, "The Heidelberg compact electron beam ion traps," *Review of Scientific Instruments*, vol. 89, p. 063109, jun 2018.

[39] L. Schmöger, M. Schwarz, T. M. Baumann, O. O. Versolato, B. Piest, T. Pfeifer, J. Ullrich, P. O. Schmidt, and J. R. C. López-Urrutia, "Deceleration, precooling, and multi-pass stopping of highly charged ions in Be+ Coulomb crystals," *Review of Scientific Instruments*, vol. 86, p. 103111, oct 2015.

[40] J. Nauta, A. Borodin, H. B. Ledwa, J. Stark, M. Schwarz, L. Schmöger, P. Micke, J. R. C. López-Urrutia, and T. Pfeifer, "Towards precision measurements on highly charged ions using a high harmonic generation frequency comb," *Nuclear Instruments and Methods in Physics Research Section B: Beam Interactions with Materials and Atoms*, vol. 408, pp. 285–288, oct 2017.

[41] M. Schwarz, J. R. C. López-Urrutia, F. R. Brunner, T. Ballance, M. Drewsen, P. O. Schmidt, and J. Ullrich, "A cryogenic Paul Trap for Highly Charged Ions and Molecular Ions," *Journal of Physics: Conference Series*, vol. 388, p. 122005, nov 2012.

[42] M. Schwarz, O. O. Versolato, A. Windberger, F. R. Brunner, T. Ballance, S. N. Eberle, J. Ullrich, P. O. Schmidt, A. K. Hansen, A. D. Gingell, M. Drewsen, and J. R. C. López-Urrutia, "Cryogenic linear Paul trap for cold highly charged ion experiments," *Review of Scientific Instruments*, vol. 83, p. 083115, aug 2012.

[43] P. Micke, J. Stark, S. A. King, T. Leopold, T. Pfeifer, L. Schmöger, M. Schwarz, L. J. Spieß, P. O. Schmidt, and J. R. C. López-Urrutia, "Closed-cycle, low-vibration 4 K cryostat for ion traps and other applications," *Review of Scientific Instruments*, vol. 90, p. 065104, jun 2019.

[44] Lambda Research Corporation, *OSLO Optics Reference*.

[45] E. Born, Max; Wolf, *Principles of Optics*. Cambridge University Press, 1999.

[46] B. Jähne, *Digitale Bildverarbeitung*. Springer Berlin Heidelberg, 2012.

[47] J. Hollenhorst, "A theory of multiplication noise," *IEEE Transactions on Electron Devices*, vol. 37, pp. 781–788, mar 1990.

[48] ANDOR, "iXon Ultra X-9661 Performance Sheet."

[49] R. C. Thompson, "Ion Coulomb crystals," *Contemporary Physics*, pp. 1–17, jan 2015.

[50] D. James, "Quantum dynamics of cold trapped ions with application to quantum computation," *Applied Physics B: Lasers and Optics*, vol. 66, pp. 181–190, feb 1998.

[51] K. Schwarzschild, "Untersuchungen zur geometrischen Optik. II," in *Gesammelte Werke/Collected Works*, pp. 130–156, Springer Berlin Heidelberg, 1992.

[52] I. H. Malitson, "Interspecimen Comparison of the Refractive Index of Fused Silica∗,†," *Journal of the Optical Society of America*, vol. 55, p. 1205, oct 1965.

[53] I. H. Malitson, "A Redetermination of Some Optical Properties of Calcium Fluoride," *Applied Optics*, vol. 2, p. 1103, nov 1963.

[54] S. Bollanti, P. D. Lazzaro, F. Flora, L. Mezi, D. Murra, and A. Torre, "Conventional and modified Schwarzschild objective for EUV lithography: design relations," *Applied Physics B*, vol. 85, pp. 603–610, aug 2006.

[55] K. A. Goldberg, E. Tejnil, S. H. Lee, H. Medecki, J. David T. Attwood, K. H. Jackson, and J. Bokor, "Characterization of an EUV Schwarzschild objective using phase-shifting point diffraction interferometry," in *Emerging Lithographic Technologies* (D. E. Seeger, ed.), SPIE, jul 1997.

[56] J. Tan, C. Wang, Y. Wang, W. Wang, J. Liu, R. Leach, and L. Hao, "Long working distance microscope with a low obscuration aspherical Schwarzschild objective," *Optics Letters*, vol. 39, p. 6699, nov 2014.

[57] H. Ball, C. D. Marciniak, R. N. Wolf, A. T.-H. Hung, K. Pyka, and M. J. Biercuk, "Site-resolved imaging of beryllium ion crystals in a high-optical-access Penning trap with inbore optomechanics," *Review of Scientific Instruments*, vol. 90, p. 053103, may 2019.

[58] L. K. Spieß, "Setup of a vibration-suppressed cryogenic system for a RF ion trap with minimum micromotion," Master's thesis, Heidelberg : Ruprecht-Karls-Universität, 2018.

[59] K. Vonnegut, *If This Isn't Nice, What Is?: Advice for the Young*. ROSETTA-BOOKS LLC, 2013.

LIST OF FIGURES

Figure 1 The first compound microscope made by Zacharias Janssen around 1606-1607. Taken from [31]. 14

Figure 2 a) Hyperbolic electrode configuration. Φ_0 is the applied electric potential, r_0 describes the distance between trap center and electrodes. Taken from [37] b)-d) Qualitative plot of the radial, RF-driven potential described in Equation 6. b) saddle potential at a given time $t = 0$; c) saddle potential at $t = \pi/\Omega_{RF}$; d) time averaged effective pseudo-potential. In addition the equipotential lines x^2–$y^2 = const$ are projected onto the x-y plane. 17

Figure 3 Stability diagram for a two-dimensional quadrupole mass spectrometer. The red and blue areas are showing the stable solutions of the Mathieu Equation 11 in x- and y-direction. In the gray area both solutions overlap and stable trapping in both directions is possible 19

Figure 4 Trajectory of an ion in a Paul trap in $u = x, y$ direction, calculated for a radial Mathieu parameter $q = 0.2$ and $a = 0.0$ in dependence of $\zeta = \Omega_{RF}\, t/2$. The blue trajectory shows only the slow secular motion while the orange curve represents secular and micromotion. The micro motion amplitude rises with increasing distance u to the centre of the quadrupole axis. 20

Figure 5 Level scheme of a Be^+ ion. 21

Figure 6 CAD rendering of CryPTEx II (bottom left), the beamline (bottom right), the XUV-Ebit (top right) and the XUV frequency comb (top left). Courtesy of Julian Stark. 22

Figure 7 Illustration of Snell's law: Two rays (blue, orange) move through medium 1 with refractive index $n_1 = 1.5$. At the boundary of medium 2 ($n_2 = 1.0$) the blue ray with incident angle $\theta_1 = 25°$ is being refracted at an angle $\theta_2 = \sin^{-1}(n_1/n_2)\theta_1 = 36.3°$ while the orange is reflected since $\theta'_1 > \theta_{crit}$. 28

Figure 8 The first five radial orders of the Zernike polynomials $Z_n^m(r, \phi)$. By expanding $W(r, \phi)$ one can see, that the different terms contribute in a uniquely to the final wavefront, e.g. $(Z_0^0, Z_1^{\pm 1}, Z_2^0)$ are representing the image position, while $(Z_2^{\pm 2}, Z_3^{\pm 3}, Z_4^0)$ describe 3rd order distortions, such as spherical aberrations. 29

Figure 9 Qualitative illustration of two points, which are separated by the Rayleigh limit. On the left side the simulated image is shown with logarithmic intensity to increase the contrast to the diffraction rings. On the right side the linear intensity profile along $y = 0$ is shown. 32

Figure 10 Illustration of the lens stack. At the bottom in dark gray a mounting ring is fixed by four M3 screws on top of the niobium resonator. Twelve M2 screws hold the cage (gray) which centers the rings inside the tower. The green rings, also shown in Figure 14, are designed to clamp and center the lenses while not destroying them in the cool down phase. Orange rings separate the lenses axially and the red ring prevents destruction due to axial pressure by the thrust pieces shown together with the top ring colored in black in Figure 15. 37

Figure 11 Drawing of the whole optical system, which was designed in this work. With a working distance of 57 mm, the stack on the left is directly mounted on top of the resonator. In between the first seven lenses at 4 K and the bi-asphere at 40 K an intermediate focus enables effective shielding of blackbody-radiation from room temperature. The magnification in the commissioning phase was set to $M = 12.7$. With a design wavelength of 313 nm, Be^+ ions can be spatially resolved on a detector. 38

Figure 12 Analysis of the PSF on- and off-axis for the lens stack with lenses $1 - 7$. On axis the Strehl-ratio is simulated to be 0.13 which is far from the diffraction limit > 0.85. Off-axis the peak is not observable anymore due to occuring aberrations. 41

Figure 13 Full field analysis of the wavefront. While photons irradiated from the center of the object experience only comparably small spherical aberrations, the off-center wavefronts are distorted by coma and a tilt in y-direction. This may be caused by the Edmund asphere, since it is designed for collimation. In Section 4.1, which outlines proposals for future updates, the first asphere was modified to counteract on these aberrations. 42

Figure 14 Illustration of a ring holder for a 2″ lens. The ring is partially segmented into 40 flexible arms with 1 mm separation. The inner diameter measures 50.5 mm and is therefore undersized to clamp and center the lenses. The wall thickness of the arms is 0.35 mm. Each ring is anodized to reduce stray light reflections. 43

Figure 15 Illustration of the final ring (dark grey) on top of the lens stack. The anodized ring is fixed by eight M3 screws to the aluminum cage and cut by a 3 mm slit. Three arms are setting and centering the 1″ meniscus lens. The mounting rings of the other lenses are pushed down by three M4 thrust pieces which are screwed into the arms. 44

Figure 16 Illustration of the intermediate focus. In the bottom picture, both meniscus lenses are shown. An aluminum shield which is mounted on the 4 K-shield. Additionally, an anodized aluminum hat with a 4 mm hole is mounted with three screws on top of the shield to reduce reflections of stray light. In blue, a 2 mm pinhole is mounted on a movable ring holder shown in red. Both pieces are made of anodized aluminum. The ring holder is fixed by three screws in axial direction on the 40 K heat shield. In addition to the diaphragm a stainless steel threaded bush (gray) is fixated on the ring. Thus, the holder for the bi-asphere colored in dark green can be screwed in and out by 2.5 mm in each direction. 45

Figure 17 Simulation of the modular transfer function in OSLO. While the performance of the lens stack is far from the diffraction limit, on axis points are still resolved far above 100 cycles/mm. At the edge of a crystal with 250 µm radius the tangential MTF falls below 0.2 at 40 cycles/mm, which corresponds to a resolution of $d = 25$ µm. 46

Figure 18 Images of a 5, 10, 20µm pinhole, taken by a CMOS with 3 µm pixel size in the intermediate focus behind the lens stack. While images (a) and (b) show the expected results and yield the pinhole sizes, (c) is distorted and asymmetrically projected on the CMOS. This is a result of the unstable ground which deforms already by moving through the laboratory. 47

Figure 19 (a)Characterization the magnification in dependence of the lens distance to the intermediate focus by moving the bi-aspheric lens along the optical axis. An inverse function $f(x) = a/(b - x)$ had been fitted on the data points. (b) Magnification in dependence of the distance from the bi-asphere to the EMCCD. 48

Figure 20 Comparison between a simulated and a real image with comparable scalings. (a) Ray tracing simulation of a grid with 100 µm side-length. (b) Cutout of a resolution target image at magnification $M = 10.47$. On the right plot the mean marginal intensity along the y-axis for the x-axis region 93.4 – 118.3 µm is shown. This corresponds to 20 px. On the bottom, the same was done for the x-axis from 89.7.4 – 151.9 µm which correspond to 20 px on the EMCCD. 49

Figure 21 Cutout of a resolution target image at magnification $M = 10.47$. On the right plot the mean marginal intensity along the y-axis for the x-axis region 186.8 – 199.2µm is shown. This corresponds to 10px. On the bottom, the same was done for the x-axis from 62.3 – 80.9µm, which correspond to 50px on the EMCCD. (b) Linear fits $f(x) = ax + b$ (red) on the averaged signal (blue) of the projected signal the horizontal lines. The resolution value determined from the slope and the 10-to-90% intensity is given by $d = (I_{90-10}/a) \cdot (px/M)$. Within this area a mean value of $< d >= 7.09(1.16)$µm was determined. 50

Figure 22 Drawing of the optical elements with a bi-asphere mounted at 4 K, replacing the lens stack. In Section 4.2 the design developed in OSLO is discussed. At a distance of 65 mm from the object plane to the first surface the lens is located. The intermediate focus and PTB bi-asphere are both still located at 157 mm and 176 mm distance from the object. The magnification has been increased to $M = 23.1$ at the image plane located 646 mm away from the object. 53

Figure 23 PSF simulation of a $NA = 0.325$ optical system with two bi-aspheres and magnification $M = 23.1$. The minimal Strehl ratio in the focus is $I/I_0 \approx 0.75$ at the center and the border of an object with 250 µm radius. On the right side the ensquared fractional energy is plotted. It is shown, that ≈ 90% of the photons are focused onto a $3x3$ pixel array. 53

Figure 24 Analysis of the wavefront aberrations for the lens system shown in Section 4.2. The peak-to-valley values as well as the RMS are reduced by an order of magnitude compared to the values in Figure 13. In the Zernike picture presented in Figure 8, a small 3rd order 0° astigmatism contributes mostly to the residual aberrations. 54

Figure 25 MTF simulation of a $NA = 0.325$ optical system with two bi-aspheres and magnification $M = 23.1$. The Abbe limit for this system is $d = 0.481$ µm which corresponds to $M \cdot 90$ cylces/mm. With the design described in Section 4.2 the diffraction limit can be reached over the whole crystal size of 500 µm × 500 µm and current limitations are only given by the EMCCD detector. 55

Figure 26 Raytracing simulations of the lens system described in Section 4.2 with a grid as object. In the left figure the grid has a side length of 50 µm and in the right 20 µm. It is shown, that a 5 µm line separation is clearly resolvable. 56

Figure 27 Drawing of the Schwarzschild mirror system, which was designed in this work and is presented in Section 4.3. At a distance of 120 mm from the object plane, the primary, collecting mirror is mounted. Separated by 55 mm to the primary mirror, one finds the secondary mirror with 11 mm diameter. The magnification has been increased by a factor of more than two, to $M = 27.46$, compared to the lens system in Chapter 3. Furthermore a reflective optical system has no chromatic aberrations which allows for a simultaneous fluorescence detection of multiple ion species. 56

Figure 28 PSF simulation of a $NA = 0.26$ optical system with Schwarzschild mirrors and magnification $M = 27.46$ as described in Section 4.3. The minimal Strehl ratio in the focus is $I/I_0 \approx 0.83$ at the center and the border of an object with 250 µm radius. On the right side the ensquared fractional energy is plotted. It is shown, that ≈ 90% of the energy is focused onto a $3x3$ pixel array for all three wavelengths. In this simulation the absorption of the secondary mirror is not included. However, only the central part of the wavefront is cut out, such that the Strehl ratio should not change dramatically. 57

Figure 29 Analysis of the wavefront aberrations for the Schwarzschild mirror system shown in Section 4.3. Compared to the currently installed setup the peak-to-valley values as well as the RMS had been reduced down to 0.2 and 0.06, respectively. 57

Figure 30 MTF simulation of a $NA = 0.26$ Schwarzschild-like optics and magnification $M = 27.46$. At a wavelength of 313 nm the Abbe limit for this system is $d = 0.6$ µm which corresponds to $M \cdot 60.5$ cylces/mm. With the design described in Section 4.3 the diffraction limit can be reached over the whole crystal size of 500 µm × 500 µm for all wavelengths and current limitations are only given by the EMCCD detector which can resolve $d_{EMCCD} = 0.947$ µm. 58

Figure 31 Raytracing simulations of the mirror system described in Section 4.3 with a grid as object. In the left figure, the grid has a side length of 20 µm and on the right 5 µm. Green dots are for 313 nm, blue for 441 nm and red for 235 nm wavelength. 58

Figure 32 Illustration of the 2″ meniscus mount. On top a ventilated ring pushes the lens uniformly into the radial clamps shown in green. On the bottom it is placed on a distance ring, separating the meniscus from the backside of a concave lens. 63

Figure 33 PSF simulation of a optical system with an optimized asphere as collecting lens which is presented in Section 4.1 . The maximum Strehl ratio in the focus is $I/I_{max} \approx 0.375$ at the center. For the outer regions of the target the performance of the system decreases significantly. On the right side the ensquared fractional energy is plotted. It is shown, that ≈ 65% of the energy is focused onto a $3x3$ pixel array. 64

Figure 34 Analysis of the wavefront aberrations for the lens system shown in Section 4.1. Peak-to-valley and root-mean-squared values and were decreased by a factor of at least two compared to the currently mounted system. 64

Figure 35 MTF simulation of a $NA = 0.365$ optical system with a modified asphere as collecting lens and magnification $M = 13.7$ as described in Section 4.1. 65

Figure 36 Raytracing simulations of the lens system described in Section 4.1 with a grid as object. On the left figure the grid has a side length of 50 µm and on the right 20 µm. It is shown, that a 5 µm line separation is clearly resolvable. 65

LIST OF TABLES

Table 1 Scaling laws for atomic properties of hydrogen-like ions [12]. 13

Table 2 Surface shapes of an asphere depending on the conic constant κ. 33

Table 3 Description of the used lenses starting with an asphere fabricated by the company Edmund Optics as first element next to the trap center. The first seven lenses are stacked in a tower on top of the niobium resonator at 4 K. Lens 8 is located behind the intermediate focus at the 40 K stage and refocuses the fluorescence to the EMCCD and the PMT outside the vacuum. 39

Table 4 Alignment of the lens stack optimized by OSLO with number of Surface, radius of the curvature, thickness, aperture radius in millimeter and the materials. 40

Table 5 Thermal shrinking of the materials used in this work from 300 K to a given temperature. 41

Table 6 Coefficients for the modified asphere which has a radius $r = 25$ mm and an numerical aperture of $NA = 0.4$. The distance to the trap center is 65 mm. 51

Table 7 First refocussing bi-asphere which has a radius $r = 27.5$ mm and an numerical aperture of $NA = 0.325$. The distance to the trap center is 65 mm. 52

Table 8 Alignment of Schwarzschild objective optimized by OSLO. Surface 1 and 3 are the mirror surfaces while surface 5 is the viewport. 56

ERKLÄRUNG

Ich versichere, dass ich diese Arbeit selbstständig verfasst und keine anderen als die angegebenen Quellen und Hilfsmittel benutzt habe.

Heidelberg, den 15.10.2019,